MEMS-Based Temperature-Dependent Characterization of Biomolecular Interactions

Bin Wang

Submitted in partial fulfillment of the
requirements for the degree of
Doctor of Philosophy
in the Graduate School of Arts and Sciences

Columbia University

2012

ABSTRACT

MEMS-Based Temperature-Dependent Characterization of Biomolecular Interactions

Bin Wang

Biomolecular interactions are of fundamental importance for a wide variety of biological processes. Temperature dependence is a ubiquitous effect for biomolecular interactions as most biological processes are thermally active. Understanding the temperature dependence of biomolecular interactions is hence critical for a wide variety of applications in fundamental sciences and drug discovery and biotherapeutics. Micro-Electro-Mechanical Systems (MEMS) technology holds great potential in facilitating temperature-dependent characterization of biomolecular interactions by providing on-chip microfluidic handling with drastically reduced sample consumption, and well-controlled micro- or nanoscale environments in which biomolecules are effectively manipulated and analyzed. This thesis is focused on various MEMS-based devices for temperature-dependent characterization of biomolecular interactions.

Biomolecular interactions can occur with biomolecules in solution or with either the target or receptor molecules immobilized to a solid surface. For surface-based biomolecular interactions, we first present microcantilever-based characterization of biomolecular affinity binding with *in-situ* temperature sensing, using a demonstrative system of platelet-derived growth factor (PDGF) and an inhibitory ligand. The temperature-dependent kinetic and equilibrium binding properties are determined. In addition, a microfluidic approach for temperature-dependent biomolecular behavior with single-molecule resolution is also presented. Using a platform that combines microfludic sample handling, on-chip temperature control, and total internal reflection fluorescence

(TIRF) microscopy, we have studied the temperature dependence of the structural dynamics of transfer RNA (tRNA) translocation through ribosome in protein synthesis.

For solution-based biomolecular interactions, we mainly focus on calorimetry, a technology that directly measures heat evolved in biological processes. We first present a MEMS differential scanning calorimetric (DSC) sensor integrating highly sensitive thermoelectric sensing and microfluidic handling for thermodynamic characterization of biomolecules. We have characterized the unfolding of protein (e.g. lysozyme) at minimized sample consumption with thermodynamic properties determined, including the specific heat capacity, molar enthalpy change, and melting temperature. In addition, we also present the development of a variant of standard DSC, temperature-modulated DSC (AC-DSC), on a MEMS device for thermodynamic characterization of biomolecules. Preliminary results again with lysozyme unfolding at optimum modulation frequencies have been presented with thermodynamic properties determined. Furthermore, we have developed a MEMS isothermal titration calorimeter (ITC) integrating thermally isolated calorimetric chambers, on-chip passive mixing, and environmental temperature control, for temperature-dependent characterization of biomolecular interactions. We have characterized the interactions of 18-Crown-6 and barium chloride, as well as ribonuclease A and cytidine 2'-monophosphate, in a 1-μL volume with low concentrations (ca. 2 mM). Thermodynamic properties, including the stoichiometry, equilibrium binding constant, and enthalpy change, are also determined.

Finally, some perspectives of future work are proposed, suggesting the strategies and noticeable issues for further development of MEMS/microfluidics-based devices for more efficient temperature-dependent characterization of biomolecular interactions.

Table of Contents

List of Charts

List of Tables

List of Symbols

k_{on}……Association rate constant

k_{off}……Dissociation rate constant

K_{d}……Equilibrium dissociation constant

$[R]$……Concentration of receptor

$[A]$……Concentration of target analyte

$[RA]$……Concentration of the receptor-analyte complex

$[RA]_{\mathrm{max}}$……Saturated concentration of the receptor-analyte complex

y……Observed response signal corresponding to the complex concentration $[RA]$

y_{max}……Observed response signal corresponding to the saturated complex concentration $[RA]_{\mathrm{max}}$

c…… Concentration of analyte $[A]$ in flow-through mode, assumed to be constant

k_{m}……Onsager coefficient of mass transport

D……Diffusivity of sample biomolecules

u……Flow rate for sample introduction

h……Chamber height

l……Cantilever length

b……Cantilever width

R……Resistance of a temperature sensor

T……Temperature

T_0……Reference temperature

R_0……Sensor resistance at a reference temperature

α……Temperature coefficient of resistivity

h……Natural convection heat transfer coefficient

T_{s}……Average surface temperature

T_{∞}……Temperature at an infinite distance

L……Characteristic dimension

k……Thermal conductivity

β……Thermal expansion coefficient

ν……Kinetic viscosity

α……Thermal diffusivity

C……Empirical parameter

m……Empirical parameter

g……Gravitational constant

ΔP……Differential thermal power

P_s……Thermal power generated in the sample material

P_r……Thermal power generated in the reference material

ΔC_P……Differential heat capacity

C_Ps……Heat capacity of the sample material

C_Pr……Heat capacity of the reference material

$\dot{T}$ ……Time rate of the controlled temperatures of sample and reference materials

ΔU……Output from the thermoelectric sensor

S……Thermoelectric sensitivity

c……Partial specific heat capacity of biomolecules

ΔH……Total change of molar enthalpy

T_m……Melting temperature

I……Modulated electric current

I_0……Amplitude of modulated electric current

ω……Modulation frequency

ΔT_ac……AC component of the sample temperature

τ……Thermal time constant

C……Total heat capacity of the sample and its containing chamber

c_solv……Partial specific heat capacity of reference solvent

Δc……Difference in the specific heat capacity of biomolecules

m……Mass of biomolecules in sample chamber

v……Partial specific volume of biomolecules

v_{solv}……Partial specific volume of reference solvent

$[M]$……Equilibrium concentration of a sample molecule

$[X]$……Equilibrium concentration of a binding reagent

$[\mathrm{M}X]$……Equilibrium concentration of the binding product

N……Stoichiometry

Q……Biomolecular reaction heat

r……Molar ratio of reactants

V_0……Active volume for reaction

M_{t}……Total concentration of sample molecule

X_{t}……Total concentration of binding reagent

K_{B}……Equilibrium binding constant

List of Abbreviations

MEMS……Micro-Electro-Mechanical Systems

DNA……deoxyribonucleic acid

RNA……ribonucleic acid

tRNA……transfer RNA

PCR……polymerase chain reaction

SPR……surface plasmon resonance

QCM……quartz crystal microbalance

MALDI-MS……matrix-assisted laser desorption/ionization mass spectrometry

DSC……differential scanning calorimetry

ITC……isothermal titration calorimetry

TIRF……total internal reflection fluorescence

CMOS……complementary metal–oxide–semiconductor

ITO……indium tin oxide

PDGF……platelet-derived growth factor

DC-DSC……standard differential scanning calorimetry

AC-DSC……temperature-modulated differential scanning calorimetry

Sb-Bi……antimony-bismuth

PDMS……poly(dimethylsiloxane)

Cr/Au……chromium/gold

CVD……chemical vapor deposition

RIE……reactive ionic etching

XeF_2……Xenon difluoride

PID…… proportional-integral-derivative

PSD……photosensitive detector

FRET……fluorescence resonance energy transfer

smFRET……single-molecule fluorescence resonance energy transfer

PRE……pre-translocation

POST……post-translocation

GS……global state

PECVD……plasma-enhanced chemical vapor deposition

NHS…… *N*-hydroxysuccinimidyl

PEG…… polyethylene glycol

E. coli…… *Escherichia coli*

EMCCD……electron multiplying charge-coupled device

TCR……temperature coefficient of resistivity

aa-tRNA……aminoacyl-tRNA

mRNA……messenger RNA

EF-G……elongation factor G

cryo-EM……cryogenic electron microscopy

TMAH……tetramethylammonium hydroxide

RMA……root-mean-square

18-C-6……18-Crown-6

$BaCl_2$……barium chloride

RNase A……ribonuclease A

2’CMP……cytidine 2’-monophosphate

Acknowledgements

This thesis would not have been possible without support and encouragement of my colleagues, friends and family. I would like to extend my sincerest thanks to all of these people for their friendship, support and love throughout all these years.

Foremost, I would like to express my sincere gratitude to my advisor, Professor Qiao Lin, for his support, enthusiasm and enlightening guidance. During my graduate study, I have benefited from him greatly in many aspects of academic research, communication skills, and personality. His profound knowledge has been a constant source of information for my research. His patient and dedicated mentoring has been extraordinary, and indispensable to the completion of this thesis.

I also want to extend my thanks to Professors Ruben L. Gonzalez Jr., Donald W. Pfaff, Tom Laue, Shimon Weiss, Jonathan B. Chaires, and Yong Xu for their enthusiastic advice and support during my Ph.D. studies. The collaboration with them has always been inspiring and delightful. I would also like to thank Stephen Smith and Scott McEuen from GE Healthcare, who noticed my work and extended my research scope to industry. I am also grateful to other members of my thesis committee, Professors Arvind Narayanaswamy, Chee Wei Wong, and Elon J. Terrell, for their insightful comments and suggestions on my thesis.

In addition, I am truly grateful to my colleagues, ThaiHuu Nguyen, Yao Zhou, Zhiyong Lin, John P. Hilton, Xian Huang, Junhui Ni, Fengliang Huang, Zhiguo Zhou, Jing Zhu, Haogang Cai, Jinho Kim, Jaeyoung Yang, Bing Song, Yuan Jia, Tim Olsen, and my collaborators, Jingyi Fei, Yoav Litvin, Joseph Ho, Bradley Frizzell, Rakesh Katragadda, Nichola C. Garbett et al., for their valuable help and discussions over the

time of my research. Many helpful discussions with other faculty and students are gratefully appreciated as well. I would also like to thank the CEPSR clean room and the machine shop at Columbia University and Cornell Nanoscale Facilities for granting me access to the fabrication and testing facilities for my research.

Moreover, I would like to thank my parents, Minggui Wang and Xue-e Tian, my brother, Ping Wang, my parents-in-law, Mingzheng Wang and Xiuhe Chen, whose love, support, and consistent encouragement kept me motivated and concentrated on my research throughout these years.

Last but not the least, I would like to express my deepest gratitude to my wife, Yuji Wang, to whom this thesis is dedicated, for her love and unwavering support during the best and worst of my times. Without her encouragement and full support, this Ph.D. would not have been possible.

Dedication

This thesis is dedicated to my wife, Yuji Wang.

Chapter 1 Introduction

1.1 Background

1.1.1 Biomolecular Interactions and Their Temperature Dependence

Biomolecular interactions are the most fundamental phenomena in biological processes [1] including structural change of biomolecules, e.g., proteins, deoxyribonucleic (DNA) and ribonucleic (RNA) acids, and binding between various biomolecules such as ligand-DNA, ligand-protein, and protein-protein. Understanding biomolecular interactions is hence of critical importance for fundamental sciences, especially concerning the energetics of biomolecular interactions as the conformational and chemical complementarity between the biomolecules strongly influences cellular signal transduction and expression [2]. Moreover, modern drug development and therapeutics have thus increasingly relied on biomolecular interaction studies [3], noticing the fact that current experimental and computational screening of compounds for therapeutic drugs is mostly based on the characterization of the ligand-target affinity binding [4]. Therefore, there has been a strong need for techniques that can reliably characterize biomolecular interactions.

Temperature dependence is a ubiquitously important effect for biomolecular interactions as biological processes are generally thermally active and the associated thermodynamic properties are naturally temperature-dependent. For example, protein folding, in which protein molecules fold into their characteristic three-dimensional structure, is typically exothermic; that is, heat is released in such processes. The reversed process, protein unfolding, in which the three-dimensional structure of protein molecules is lost under heating, absorbs heat and is hence endothermic. Another more complicated example is with the ribosome, the biomolecular machine that is responsible for protein synthesis, or translation, in all living cells [5]. Previous studies on the translocation of transfer RNA (tRNA) through the ribosome during protein synthesis have demonstrated that pre-translocation ribosome-tRNA complexes undergo spontaneous and thermally activated fluctuations between two discrete and structurally well-characterized global conformational states [6]. Hence, an ability to study ribosome and tRNA structural dynamics as a function of well-defined temperature changes can reveal mechanistically important details regarding the energetics of biomolecular behavior.

1.1.2 Importance of Temperature-Dependent Characterization of Biomolecular Interactions

Temperature-dependent characterization of biomolecular interactions is crucial for **drug discovery and bio-therapeutics**. Affinity binding (generally the most fundamental of biomolecular interactions) is a chemisorptions process which results in high strength bonds between receptor and target molecules [7]. It involves large intermolecular forces and activation energies, resulting from the specific nature of the two participating molecules [8]. Since the binding affinity commonly involves thermodynamic activity and is determined by the Gibbs energy during biomolecular interactions [4], consideration of temperature effects is necessary in therapeutic ligand design. In addition, as *in-vivo* relevant therapeutic assays have become increasingly important, insight into the temperature-dependent nature of biomolecular affinity binding [9, 10] can be critical for understanding the mechanisms governing these interactions, such as the efficacy of drug molecules under thermally active stimulation [11]. Moreover, knowledge about the temperature dependence of ligand-receptor systems can assist in identifying therapeutic targets by exploring receptor dysfunction associated with metastasic cell proliferation, or receptor recovery leading to tissue repair [12].

On the other hand, once fully characterized, the temperature dependence of biomolecular interactions can be also used for various **biochemical detection and biomolecular manipulation**. A well-known example of such applications is the polymerase chain reaction (PCR), the most powerful tool for fast, specific pathogenic detection [13]. PCR is based on the amplification of a very specific DNA sequence, referred to as the target sequence. In the presence of a particular enzyme, *Taq* polymerase, and specific primers (short strands of single-stranded DNA, complementary to part of the target sequence), the target sequence is duplicated by processing once through a cycle of different temperatures, generating multiple copies of the initial target DNA on an exponential basis [13]. Applications for biomolecular manipulation are based on the fact that binding equilibrium significantly migrates with temperature. At optimal temperatures, a receptor-analyte system can form strong binding while dissociates at another temperature depending on the conformation of receptor molecules [2] (Figure 1-1), which can be utilized for thermally controlled enrichment and detection of target analyte molecules in a fluidic environment [11].

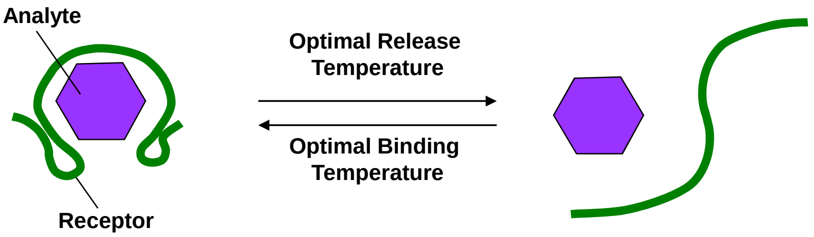

Figure 1-1: Schematic of thermally controlled binding and release of receptor-analyte [2, 11].

1.2 Methods for Characterization of Biomolecular Interactions

There have been many technical methods for biomolecular characterization. Biomolecular interactions can occur with biomolecules in solution or with either target or receptor molecules immobilized to solid surfaces. **Surface-based** biomolecular interactions, which are widely used in affinity biosensors [14], can be investigated with methods such as protein arrays [15], immunoassays [16], thermal-shift assays [17], surface plasmon resonance (SPR) [18] and quartz crystal microbalance (QCM) [19]. Meanwhile, **solution-based** biomolecular interactions are commonly characterized using methods such as UV-absorption [20], differential and titration calorimetry [21], matrix-assisted laser desorption/ionization mass spectrometry (MALDI-MS) [22] and electrophoretic separation [23].

1.2.1 Surface-Based Biomolecular Interactions

Most surface-based biomolecular interactions are based on bio-affinity assays [24] in which the receptor molecules are typically immobilized on a solid substrate while the target molecules are introduced and induce a detectable signal upon binding with receptor molecules. Affinity-based biomolecular interactions traditionally include antigen and antibody, lectin and carbohydrate, enzyme and inhibitory systems, as well as novel oligonucleotide aptamers [2]. Aptamers are a special class of molecules derived from RNA or DNA that bind to a target analyte with high specificity [2] by ways of precise stacking of moieties, specific hydrogen bonding, and folding upon binding to the target molecules (i.e., an aptamer molecule can incorporate small molecules into its nucleic acid structure or integrate into the structure of a large molecule [25]). These allow aptamers to distinguish between their target analytes and non-specific molecules by subtle variations such as chirality, functional end group, or isoform [11].Aptamers have several advantages over conventional high-affinity reagents (e.g. antibodies or enzymes) including the wide applicability to virtually any target molecules as they can be synthesized [26], stability at room temperature, and convenience of modifying the terminal sites for easy immobilization to solid surfaces [27, 28].

The detection of surface-based biomolecular interactions is typically based on the following technologies:

1. **Fluorescence microscopy and spectrometry**: Fluorescent groups are attached to the biomolecules through direct labeling to certain molecular sites [29], or sandwiched labeling using an intermediate analyte-specific reagent [30], and the quick scan of the fluorescence intensity gives information of the biomolecules printed on a solid surface or interactions between target and immobilized receptor molecules [15, 29, 30].
2. **Surface plasmon resonance (SPR)**: SPR detection allows direct observation of biomolecular interactions between a target analyte and its binding receptor immobilized on a solid surface by measuring the changes in refractive index close to the sensor surface upon binding [18].
3. **Thermal-shift assays**: This is also called ThermoFluor [31] based on the observation that ligands perturb protein thermal stability upon binding to the protein in its native state, represented by an increase in the protein melting temperature [17] measured by fluorescence intensity change during the transition.

4. **Quartz crystal microbalance (QCM)**: QCM measures the shift of resonant frequency of a thin quartz oscillator whose surface is functioned and immobilized with receptor molecules upon. Upon binding with target analyte molecules, the change in mass causes a change in resonant frequency which can then be related to biomolecular interactions [32].
5. **Cantilevers**: Using microcantilevers whose surface is immobilized with receptor molecules, the binding with target analyte molecules is transduced to a mechanical signal and can be detected through the cantilever deflection (static mode) or the resonant frequency change (dynamic mode) [33].

1.2.2 Single-Molecule Investigation of Biomolecular Interactions

Single-molecule studies, in contrast to ensemble measurements, involve direct observation and analysis of individual biomolecules, allowing access to mechanistic information that is often obscured in ensemble measurements [34]. A major strength of studying biological processes with single-molecule resolution is the direct measurement of distributions of molecular properties, rather than their ensemble averages [34]. By constructing histograms of particular physical chemical properties for many individual molecules, deviant subpopulations can be identified and characterized [34]. Moreover, the recording of single molecule trajectories allows real-time observation of biological processes and rare and short-lived intermediates [34]. The absence of a need for synchronization of the entire ensemble of molecules allows us to extract detailed dynamical information from single-molecule trajectories, otherwise obscured in kinetic ensemble studies by dephasing processes [5, 35-37].

Single-molecule investigation is ideally suited for characterization of biomolecular association and dissociation kinetics under equilibrium conditions [34]. Single-molecule methods do not only enable direct observation of binding and unbinding events for a very precise determination of rate constants [38], but also allow the visualization of various types of heterogeneity in binding properties [34]. There has been single-molecule characterization of biomolecular interactions and correlation to information on structural conformation [39-41].

Contemporary single-molecule studies have benefitted greatly from the development of advanced surface-based biomolecular characterization techniques, such as single-molecule fluorescent microscopies [42] based on sensitive optical probes [43], effectively providing molecular structural and functional information at the single-molecule level. Building on these advances, single-molecule studies of a wide range of biochemical systems have led to significant advances in the mechanistic understanding of such systems [44-50].

1.2.3 Biocalorimetry

Among the technologies for solution-based biomolecular characterization, calorimetry has been an increasingly attractive method with distinct advantages over other techniques. Calorimetry directly measures heat evolved in biological processes and allows for determination of thermodynamic properties [51-53], and is universally applicable to a wide variety of biomolecules in that almost all reactions are thermally active. As calorimetric measurements occur in solution phase without restrictions from biomolecular immobilization to solid surfaces, the biomolecules can retain their full conformational changes and avidity effects during interactions [54, 55]. Additionally, calorimetric measurements are label-free in that biomolecules are not required to be labeled with a radioactive, enzymatic or fluorescent labeling groups to report molecular binding or conformational changes. To date, calorimetry has been widely used in drug discovery and biotherapeutic development [56].

There are two major types of calorimetry depending on the operation mode: **differential scanning calorimetry (DSC)** and **isothermal titration calorimetry (ITC)**. DSC (Figure 1-2a) involves measuring heat by monitoring the differential thermal activity between a sample and a reference material in two matched calorimetric chambers whose temperatures are scanned at a specified rate over a chosen range [57, 58]. The thermally induced activity of the sample molecules, which is either exothermic or endothermic, causes a thermal power difference between the sample and reference materials (i.e., differential thermal power). Measurement of the biologically induced differential thermal power leads to the determination of the thermodynamic properties of the sample biomolecules. Because of ubiquitous heat production or absorption in biomolecular conformational transitions such as protein folding and unfolding, DSC is widely used for characterizing such processes [51-53, 59-61].

ITC (Figure 1-2b) measures heat evolved in a biochemical reaction as a function of the molar ratio of reactants. In particular, a binding reagent is titrated, or added in known aliquots, into a sample, while the reaction heat is measured and used to calculate a full set of thermodynamic properties [62]. It can simultaneously determine all binding parameters with a single set of experiments, and thus provides an efficient, high-precision, label-free method for characterization of biomolecular interactions [63]. To date, ITC has been widely used for applications in fundamental sciences [64-66], as well as drug discovery and biotherapeutics development [67-69].

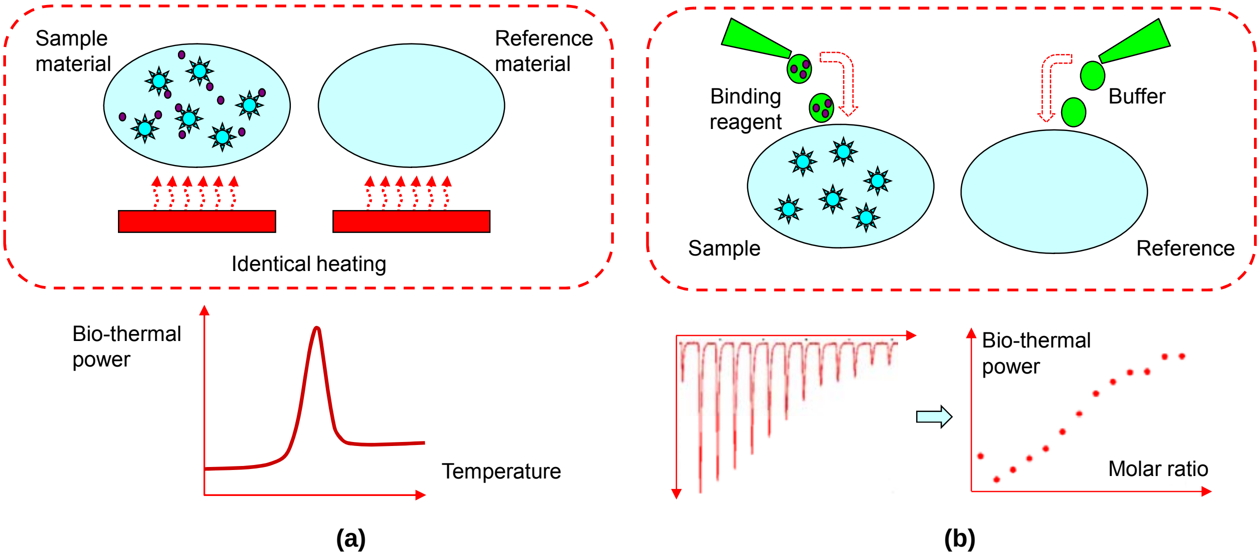

Figure 1-2: Schematic of the principle of (a) DSC and (b) ITC.

1.2.4 Temperature-Controlled Biomolecular Interactions

With temperature-control functionalities equipped with the biomolecular characterization technologies listed above, temperature-dependent characterization of biomolecular interactions is possible. However, such studies are generally limited by the conventional technologies in which temperature control to bioassays is achieved by maintaining the entire physical space in which the experiment is performed at a suitable temperature [70] or placing devices on external temperature-controlled modules [71]. These schemes are unsuitable for real-time biomolecular characterization as they typically involve heating of large thermal masses, inaccurate temperature sensing, and slow thermal response. For example, current cantilever-based characterization of biomolecular interaction at accurately controlled temperatures is scarce, while the few existing examples offer limited interpretation of affinity binding kinetics at relatively low temperature resolutions [72]. In addition, the measurement of the temperature-dependence of single-biomolecular behavior remains a major challenge [73], and generally suffers from heating of large thermal masses and temperature sensing in regions far removed from the single molecules under investigation, and is hence cumbersome, slow, and relatively inaccurate [74, 75].

1.3 Micro-Electro-Mechanical Systems (MEMS) for Characterization of Biomolecular Interactions

1.3.1 MEMS Technology and Opportunities in Biomolecular Characterization

Micro-Electro-Mechanical Systems (MEMS) technology features miniature devices that integrate electrical and mechanical components with sub-micrometer to millimeter sizes. MEMS devices are fabricated using techniques involving thin-film deposition, lithography, and selective etching, which are originally derived from integrated circuit fabrication techniques. MEMS technology enables batch fabrication of devices with reduced manufacturing cost and time. In addition, MEMS devices offer miniature sizes and maximal portability, and can allow for improved time responses, high sensitivity, and low power consumption. Furthermore, MEMS devices are easily integrated with microfluidic handling of well-defined liquid-phase samples and more importantly, well-controlled micro- or nanoscale environments in which biomolecules are effectively manipulated and analyzed [76]. Therefore, MEMS technology tailored to biomedical applications holds great potential in facilitating characterization of both surface- and solution-based biomolecular interactions.

1.3.2 Current Surface-Based Biomolecular Characterization in MEMS Devices

Recently, there has been increasing attention of microcantilevers to study surface-based affinity binding [77], offering a highly sensitive, low-cost platform capable of label-free, real-time detection of biomolecular interactions and conformational changes [78, 79]. Microcantilevers have been applied to studies of membrane protein-ligand [80], antibody-antigen [81], receptor-ligand [82], protein-protein [83], and protein-DNA [84] systems. Due to the miniaturization nature of microcantilevers, they are also easy to integrate with other MEMS and microfluidic functional elements to allow for effective environmental control for biomolecular characterization. Moreover, unlike other surface-based biomolecular characterization techniques such as SPR [18] and QCM [19], cantilevers can distinguish between binding molecules in active and inactive forms as the measurement is based on the change of surface stress across the cantilever surface [72], which is highly specific to conformational change of immobilized receptor upon binding.

A variety of microfluidic devices have also been created for surface-based single-molecule investigations[76]. For example, rapid single-molecule bioassays have been performed in microchannels in combination with microscopic techniques such as total internal reflection fluorescence (TIRF) microscopy[85]. These microscopy-based microfluidic systems have facilitated studies including the hybridization DNA probes to surface-immobilized DNA targets[86] and the kinetics of chromatin assembly on individual DNA molecules[87]. In addition, microfabricated submicron-sized channels[88], molecular-confinement microfluidic reactors[89], microcavities[90], and microelectrodes[91] have all been incorporated into microfluidic devices in order to provide controlled experimental conditions for various biological studies at the single-molecule level.

1.3.3 Current MEMS-Based Calorimetric Devices

Several MEMS calorimetric devices have been reported in the literature. Lai et al. [92] developed a chip-based microcalorimeter for characterization of properties of polymers and other thin film materials. Jaeggi et al. [93] reported a thermoelectric AC power sensor using a polysilicon/aluminum thermopile realized by complementary metal–oxide–semiconductor (CMOS) IC technology. Hagleitner et al. [94] described smart thermal sensors highly integrated with solid-state thermopiles by CMOS and micromachining technology for gas sensing. Cavicchi et al. [95] presented a MEMS calorimetric sensor with a silicon nitride diaphragm and solid state thermopile for combustible gas detection. Barnes et al. [96] reported a bimetallic microcalorimeter with femtojoule sensitivity for use as a photothermal spectrometer. Johannessen et al. [97] and Verhaegen et al. [98] described chip-based calorimeters for measurement of catalase activity within a single mouse hepatocyte and detection of cell metabolism. Chancellor et al. [99] and Olson et al. [100] presented micromachined calorimeters that demonstrated measurement of enthalpy changes due to evaporation of water droplets.

However, the existing MEMS calorimetric devices are generally limited by several critical issues. One issue is in the inability to properly handle liquid samples in a well-defined environment. Current MEMS calorimeters are mostly limited to solid- [92, 101] or gas-phase [95] or droplet-based [102] detections. There have been reports on devices integrating sensitive thermal sensors situated on freestanding membranes for liquid-phase calorimetric measurements [99, 103]. However, such devices either involve measurements in open environments without proper fluid confinement [99], which are prone to environmental disturbances and also do not yield volume-specific information, or use off-chip external flow cells, which are not amenable to miniaturization and require rather large sample consumption [103].

Alternatively, by integrating microfluidic chambers or channels as biological reactors, flow-through and continuous-flow MEMS calorimeters [104] have been reported. The calorimetric sensing in these devices can be achieved through IR thermography [105], mechanical resonation [106], or integrated thin-film thermal sensors such as a resistor [107] or a thermopile [108]. These devices provide controlled fluidic environments and can allow easy integration with other microfluidic functionalities or thermal sensing configurations [109] for biochemical thermodynamic investigations. However, they still require a large amount of samples while being limited by significant convective heat leakage due to the continuous flow. More importantly, the measurements are mostly conducted without well-defined volumes [104], which makes it difficult to obtain quantitative information associated with the reaction. In addition, the existing MEMS calorimetric devices generally lack mixing functionalities [110], which is critical for reaction between microfluidic samples. Moreover, the temperature control for measurements of biochemical reactions is typically missing, and prevents from determining temperature-dependent binding properties [111].

1.3.4 MEMS-Based Temperature-Dependent Characterization of Biomolecular Interactions

The critical need of temperature-dependent characterization of biomolecular interactions can be potentially addressed by leveraging MEMS/microfluidic devices fully

Table 1-1 Working principle, range, and comments on mostly used micro-temperature sensors [113].

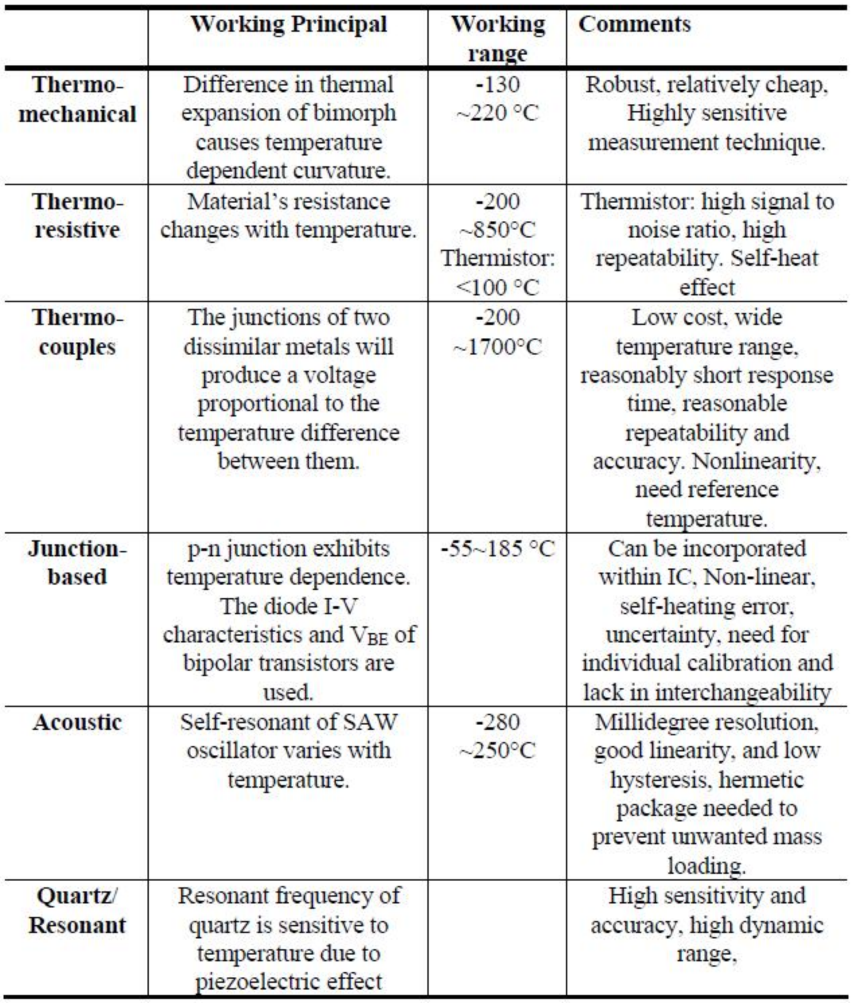

	Working Principal	Working range	Comments
Thermo-mechanical	Difference in thermal expansion of bimorph causes temperature dependent curvature.	-130 ~220 °C	Robust, relatively cheap, Highly sensitive measurement technique.
Thermo-resistive	Material's resistance changes with temperature.	-200 ~850°C Thermistor: <100 °C	Thermistor: high signal to noise ratio, high repeatability. Self-heat effect
Thermo-couples	The junctions of two dissimilar metals will produce a voltage proportional to the temperature difference between them.	-200 ~1700°C	Low cost, wide temperature range, reasonably short response time, reasonable repeatability and accuracy. Nonlinearity, need reference temperature.
Junction-based	p-n junction exhibits temperature dependence. The diode I-V characteristics and V_{BE} of bipolar transistors are used.	-55~185 °C	Can be incorporated within IC, Non-linear, self-heating error, uncertainty, need for individual calibration and lack in interchangeability
Acoustic	Self-resonant of SAW oscillator varies with temperature.	-280 ~250°C	Millidegree resolution, good linearity, and low hysteresis, hermetic package needed to prevent unwanted mass loading.
Quartz/ Resonant	Resonant frequency of quartz is sensitive to temperature due to piezoelectric effect		High sensitivity and accuracy, high dynamic range,

integrated with on-chip temperature-control functionalities. Conventionally, temperature control to bioassays is achieved by maintaining the entire physical space in which the experiment is performed at a suitable temperature [70] or placing devices on external temperature-controlled modules [71]. These schemes are unsuitable for real-time biomolecular characterization as they typically involve heating of large thermal masses, inaccurate temperature sensing, and slow thermal response. Recent microfluidic devices using on-chip circulating water bath with no temperature sensing in the detection channels [112] feature open-loop temperature control strategy that does not allow adequate accuracy and is rather cumbersome in operation, especially during the transition between temperature setpoints. In contrast, micro-heaters and temperature sensors (Table 1-1 [113]) hold great potential in addressing this critical issue. Among these sensors, microfabricated thin-film temperature control elements integrated within microfluidic channels or chambers allow for simple fabrication and integration for efficient temperature-dependent investigations [114]; however, their application for characterizing biomolecular interactions has yet to be fully explored.

1.4 Significance and Contributions of This Thesis

The main thrust of this Ph.D. thesis is to address the opportunities for MEMS technology in biomolecular characterization. MEMS devices that integrate microfluidic handling, miniature environment control, and thermal transduction functionalities have been developed for characterization of various biomolecular interactions both surface- and solution-based. Based on systematic measurements conducted in these devices, thermodynamic properties and their temperature dependence associated with the biomolecular interactions have also been elucidated. Work performed in this thesis will contribute to establishing a solid foundation for realizing integrated miniature instruments or systems that meet challenges not attainable with currently available technologies for temperature-dependent characterization of biomolecular interactions. The significance of this thesis is summarized below.

Integrated real-time, *in-situ* temperature control to biomolecules in microfluidic devices with well-defined environments: To address the issues with current temperature-dependent investigations of surface-based biomolecular interactions, thin-film resistive micro-heaters and temperature sensors have been directly fabricated on-chip in the biomolecular detection region to provide *in-situ* temperature sensing and closed-loop controlled temperatures to biomolecules in the detection. More importantly, the integrated MEMS thermal transducers have been carefully designed for different needs within well-defined environments in various applications. For example, an indium tin oxide (ITO) resistive temperature sensor on a glass cover of a microfluidic chamber is used to measure the chamber temperature, as well as unobstructed optical access for reflection-based optical detection. While for heating uniformity in microchannels, microheaters are placed on either side of a microchannel, and temperature sensors with sufficiently small footprints are located in the center of the microchannel. This configuration ensures that the region of the chip heated by the microheaters is much larger than the detection volume, thus eliminating non-uniform temperature distributions within the detection volume.

DSC and ITC characterization with well-defined miniature volumes of liquid-phase biomolecules: While existing MEMS calorimetric devices are limited by inadequacy of properly handling liquid samples in a well-defined environment, or lacking volume-specific information for quantitative determination of thermodynamic information, we have developed MEMS devices integrating microfluidic calorimetric chambers with maximized thermal isolation, integrated thin-film thermoelectric sensors and resistive micro-heaters and temperature sensors, and on-chip microfluidic mixing for DSC and ITC measurements of liquid-phase biomolecular samples with well-defined, miniature volumes that are three orders of magnitude smaller than those used in conventional calorimeters. Other noticeable advantages of MEMS DSC and ITC devices include reduced thermal mass and thus rapid thermal response, enhanced throughput by integration of parallel functional units, and low cost by MEMS batch fabrication.

Thermodynamic properties of biomolecules determined from the measurements, with important temperature-dependent information previously unavailable: Notably, the interpretation of the measurement results using the MEMS devices for biomolecular interactions has been conducted attributable to the well-defined sample volumes and reaction environment. This allows, for the first time, full elucidation of temperature-dependent thermodynamic information of several biomolecular interactions of critical scientific and therapeutic interest. For example, the temperature-dependent affinity properties of the binding between platelet-derived growth factor (PDGF), a protein regarded as a ubiquitous mitogen and chemotactic factor in angiogenesis, and an affinity aptamer have been determined and can potentially used for the screening and optimization of inhibiting ligands of PDGF and other target molecules. In addition, our investigate the temperature-dependence of ribosome and tRNA structural dynamics reveal that the previously characterized, thermally activated transitions between two global conformational states of the pre-translocation ribosomal complex have well-defined, measurable, and disproportionate effects and persist at physiological temperature. The important information listed above is unavailable in previous literature.

Following the significant approaches above, the major contributions of this thesis are summarized as follows:

Design and development of microfluidic devices integrating on-chip temperature control for surface-based biomolecular interactions: Microfluidic devices integrating on-chip micro-heaters and temperature sensors have been developed, either exploiting microcantilevers for temperature-dependent characterization of biomolecular affinity binding, or combining prism-based total internal reflection fluorescence (TIRF) microscopy for investigation of the temperature dependence of biomolecular activity with single-molecule resolution. For each case, the integrated MEMS thermal features are designed to ensure accurate and uniform temperature control as well as compatible with the biological detection systems.

Characterization of surface-based biomolecular interactions, obtaining temperature-dependent thermodynamic information: With the microcantilever device, we demonstrate label-free characterization of temperature-dependent binding kinetics of the PDGF protein with an aptamer receptor. Affinity binding properties including the association and dissociation rate constants as well as equilibrium dissociation constant are obtained, and shown to exhibit significant dependencies on temperature. With the single-molecule detection device, we investigate the temperature-dependence of ribosome and tRNA structural dynamics through the ribosome during protein synthesis. Thermally activated transitions between two global conformational states of the pre-translocation ribosomal complex show temperature-dependent rates with well-defined, measurable, and disproportionate effects.

Design and development of MEMS calorimetric sensors: MEMS devices integrating sensitive thermoelectric sensing and microfluidic handling have been developed for calorimetric detection of biomolecules. In particular, two matched microfluidic chambers are situated on freestanding diaphragms and surrounded by air cavities for maximized thermal isolation. Thin-film resistive micro-heaters and temperature sensors are integrated for on-chip device calibration and *in-situ* temperature monitoring, while a thermopile is also integrated with its hot and cold junctions aligned to the calorimetric chambers for sensing the differential temperature caused by biomolecular interactions. For effective measurement of biochemical reaction, the chambers are connected to inlets through passive chaotic mixers.

Demonstration of biomolecular characterization in various functional modes: standard (DC) and temperature-modulated (AC) DSC, and ITC: For DSC measurements, the devices are situated in a thermal enclosure which shields environmental disturbances as well as provides temperature scanning to the devices. DC-DSC requires the temperature to be varied at a constant rate within a range of interest while AC-DSC uses the on-chip heaters to generate an AC modulated heating power to samples. For ITC measurements, the temperature is controlled at setpoints by the thermal enclosure while the reactants at varying molar ratios are introduced, mixed, and their reaction detected. We have characterized protein unfolding (e.g., lysozyme) using DC- and AC-DSC, and biomolecular interactions (e.g., 18-Crown-6 and barium chloride, and ribonuclease A and cytidine 2'-monophosphate) using ITC measurements.

Interpretation of DSC and ITC measurements, obtaining thermodynamic properties of biomolecular stability and temperature-dependent biomolecular interactions: Based on the calorimetric measurements on the MEMS devices, analytical modeling and data fitting have been performed to determine the critical thermodynamic properties of the biomolecular interactions. DSC characterization of protein unfolding has led to the specific heat capacity, molar enthalpy change, and melting temperature of the protein; while ITC characterization of biomolecular interactions has led to the stoichiometry, equilibrium binding constant, and enthalpy change of the interactions. The obtained values have also been compared with established data using conventional calorimeters.

1.5 Thesis Outline

In this thesis, several MEMS devices integrating microfluidic handing and thermal transduction for temperature-dependent characterization of biomolecular interactions will be presented. The work incorporated in this thesis can be divided into two major categories: characterization of surface-based biomolecular interactions based on microcantilevers (Chapter 2) and single-molecule detection (Chapter 3), and characterization of solution-based biomolecular interactions using MEMS-based calorimetric devices (Chapters 4 – 6).

In Chapter 2, label-free characterization of temperature-dependent biomolecular affinity binding on solid surfaces using a microcantilever device will be introduced. The device consists of a polymer cantilever, whose surface is functionalized with molecules as an affinity receptor to a target analyte, located in a microfluidic chamber integrating a transparent ITO resistive temperature sensor on the underlying substrate. The ITO sensor allows for real-time measurements of the chamber temperature, as well as unobstructed optical access for reflection-based optical detection of the cantilever deflection. The measured cantilever deflection is used to determine the target-receptor binding characteristics. We demonstrate label-free characterization of temperature-dependent binding kinetics of the PDGF protein with an aptamer receptor. Affinity binding properties including the association and dissociation rate constants as well as equilibrium dissociation constant are obtained, and shown to exhibit significant dependencies on temperatures.

In Chapter 3, a microfluidic approach for single-molecule studies of the temperature-dependent behavior of biomolecules will be presented. The approach couples a temperature-controlled microfluidic flowcell to a prism-based TIRF microscope. The microfluidic flowcell comprises a set of parallel microchannels sandwiched between a quartz microscope slide and a glass coverslip, onto which thermal control elements are integrated. The temperature inside a microchannel selected for single-molecule measurements is maintained at a desired setpoint using a closed-loop control of the on-chip heaters and temperature sensors. The platform is used to study the temperature dependence of ribosome and tRNA structural dynamics that are required for the rapid and precise translocation of tRNAs through the ribosome during protein synthesis. The results provide a robust experimental framework for investigating the thermodynamic activation parameters that underlie transitions across these barriers.

Chapter 4 introduces a MEMS DSC sensor for characterization of liquid-phase biomolecular samples. The device consists of two microchambers, each of which is based on a freestanding polyimide diaphragm and surrounded by air cavities for thermal isolation. The chambers are each equipped with a thin-film gold resistive heater and temperature sensor, and are also integrated with a thin-film antimony-bismuth (Sb-Bi) thermopile. For DSC measurements, the chambers are respectively filled with a biomolecular sample and a reference solution, with their temperature varied at a constant rate. The thermopile voltage is measured to determine the differential power between the chambers for thermodynamic characterization of the biomolecules. The device is used to measure the unfolding of proteins in a small volume (1 μL) and at practically relevant concentrations (approximately 1 mg/mL), demonstrating the potential of MEMS calorimetry to enable sensitive biomolecular characterization with minimized sample consumption. .

In Chapter 5, a MEMS-based approach to AC-DSC for biomolecular characterization will be presented. Based on a MEMS device integrating microfluidic handling with highly sensitive thermoelectric detection as well as on-chip AC heating and temperature sensing, we perform, for the first time, MEMS-based AC-DSC detection of liquid biological samples, demonstrated by the measurements of protein unfolding. The specific heat capacity and the melting temperature of the protein during the unfolding process are obtained and found to be consistent with published data. This MEMS AC-DSC approach has potential applications to label-free characterization of biomolecules.

In Chapter 6, we present a MEMS-based ITC device for characterization of biomolecular interactions. The MEMS device consists of two identical microchambers, each situated on a freestanding diaphragm and surrounded by air cavities for effective thermal isolation. The chambers are integrated with a sensitive thin-film thermopile and connected to the inlets through a passive chaotic micromixer. The mixer uses herringbone-shaped ridges in the ceiling of a serpentine channel to generate a chaotic flow pattern that induces mixing of the incoming liquid streams. We demonstrate experimental results of the biomolecular interactions in a 1-μL volume. Consistent temperature-dependent thermodynamic properties of the biomolecular binding, including the stoichiometry, equilibrium binding constant, and enthalpy change, are also obtained, demonstrating the potential of efficient thermodynamic characterization of biomolecular interactions with minimized sample consumption.

This thesis will conclude with a summary and a discussion of future work in Chapter 7.

Chapter 2 Microcantilever-Based Label-Free Characterization of Temperature-Dependent Biomolecular Affinity Binding

This chapter presents label-free characterization of temperature-dependent biomolecular affinity binding on solid surfaces using a microcantilever-based device. The device consists of a Parylene cantilever one side of which is coated with a gold film and functionalized with molecules as an affinity receptor to a target analyte. The cantilever is located in a poly(dimethylsiloxane) (PDMS) microfluidic chamber that is integrated with a transparent indium tin oxide (ITO) resistive temperature sensor on the underlying substrate. The ITO sensor allows for real-time measurements of the chamber temperature, as well as unobstructed optical access for reflection-based optical detection of the cantilever deflection. To test the temperature-dependent binding between the target and receptor, the temperature of the chamber is maintained at a constant setpoint, while a solution of unlabeled analyte molecules is continuously infused through the chamber. The measured cantilever deflection is used to determine the target-receptor binding characteristics. We demonstrate label-free characterization of temperature-dependent binding kinetics of the platelet-derived growth factor (PDGF) protein with an aptamer receptor. Affinity binding properties including the association and dissociation rate constants as well as equilibrium dissociation constant are obtained, and shown to exhibit significant dependencies on temperature.

2.1 Background

Biomolecular affinity binding is of fundamental importance for fundamental sciences [2] and drug development and therapeutics [3]. Temperature-dependent characterization of biomolecular affinity binding is crucial [4, 9-11]. One clinically significant example is the development of inhibitory ligands for PDGF, a protein regarded as an ubiquitous mitogen and chemotactic factor [20] in angiogenesis. If the inhibitory ligands to PDGF are used *in vivo*, it is crucial to understand the temperature-dependence underlying PDGF-ligand interaction. Therefore, there is a strong need for a technique that can reliably characterize the effects of temperature on biomolecular affinity binding.

Affinity binding can occur with target and receptor molecules in solution, or with either molecule immobilized to solid surfaces. Characterization of surface-based affinity binding, which is typically based on affinity biosensors [14], can be investigated with methods such as protein arrays [15], immunoassays [16], and thermal-shift assays [17], which use fluorescent or radioactive labeling groups to signal binding events. Such labeling of target or receptor molecules is in general time-consuming and labor intensive, and is not capable of distinguishing signals from analytes in inactive and active forms [115]. More importantly, when used for temperature-dependent studies, fluorescent or radioactive labeling compounds can be temperature-dependent in their own right, or interfere with the binding under investigation.

Label-free methods, such as surface plasmon resonance (SPR) [18] and quartz crystal microbalance (QCM) [19], have also been used for characterization of affinity binding on solid surfaces. More recently, there has been increasing use of microcantilevers to study surface-based affinity binding [77]. Compared with SPR and QCM, the significant advantages of using microcantilevers include distinguishing the bound molecules in active and inactive forms, and the wide applicability to various experimental configurations involving other microfluidic and MEMS functional elements.

However, there has been a lack of studies that adequately characterize temperature-dependent thermodynamic properties of the binding interaction [116]. Currently, microcantilever-based characterization of biomolecular interaction at controlled temperatures is scarce, while the few existing examples [72] offer limited interpretation of affinity binding kinetics at relatively low temperature resolutions. This need can be potentially addressed by leveraging temperature-control microdevices. Conventional schemes, such as heating the entire physical space in which the devices are located [70] or placing devices on external temperature-controlled modules [71], are unsuitable for real-time biomolecular characterization as they typically involve heating of large thermal masses, inaccurate temperature sensing, and slow thermal response. Microfabricated thin-film temperature control elements integrated within microfluidic devices allow for efficient temperature-dependent investigations [117]; however, their application for characterizing biomolecular affinity binding has yet to be fully explored.

This chapter presents label-free characterization of temperature-dependent biomolecular affinity binding on solid surfaces, using a microfluidic device integrating sensitive polymer cantilevers and on-chip temperature sensing. With *in-situ* temperature sensing enabled by an integrated temperature sensor with unobstructed optical access, the device enables the elucidation of kinetic and equilibrium binding properties at well-controlled temperatures, and can be potentially extended to study transient thermal effects on biomolecular binding. Using the device, we demonstrate a label-free study of temperature-dependent affinity binding between PDGF and a complementary aptamer. Quantitative binding properties are obtained as a function of temperature, including the association and dissociation rate-constants (k_{on} and k_{off}) as well as equilibrium dissociation constant (K_{d}). These results offer previously unavailable insight into the temperature-dependence of the aptamer-PDGF affinity system.

2.2 Materials and Methods

2.2.1 Principle

Microcantilevers can transduce surface-based biochemical interactions into mechanical signals. In particular, when biomolecules immobilized on the cantilever surface undergo intermolecular reactions, their conformational change causes a change in the surface stress on the cantilever due to reduction decrease in free energy [72]. The deflection of the cantilever induced by the surface stress change provides a direct measure of the biomolecular interaction. For instance, the steady-state cantilever deflection can indicate the fraction of immobilized biomolecules that have bound to free analytes in solution, while the time to reach steady state reflects the rate constant of the specific binding. When the microcantilever is integrated with microheaters and temperature sensors, temperature-dependent properties of biomolecular interactions can be investigated at well-defined temperatures.

We exploit this concept and employ a cantilever-based microfluidic device (below) to investigate temperature-dependent ligand-receptor binding, using PDGF and a PDGF-specific aptamer as an example affinity system for demonstration. Aptamers are a class of synthetically developed RNA or DNA that bind to specific target analytes with high specificity [2, 11]. This PDGF-specific aptamer is a 36t ligand containing a three-way helix junction secondary structure motif [20] and synthesized with a 3′-3′-linked thymidine nucleotide (designated by [3′T]) at the 3′-end and a thiolated 5′-end for attachment to gold surface via thiol chemistry (Figure 2-1). The aptamer-PDGF interaction is enabled by continuously introducing PDGF solution to the immobilized aptamer. Upon binding, conformational changes in the nucleic acid structure of the aptamer molecules subsequently impart a uniform surface stress on the cantilever, which causes microcantilever deflection (Figure 2-2). Thus, measurement of this deflection, e.g., using an optical method in which a light beam reflects off the cantilever, can be interpreted to reveal kinetic properties within the binding between aptamer and PDGF.

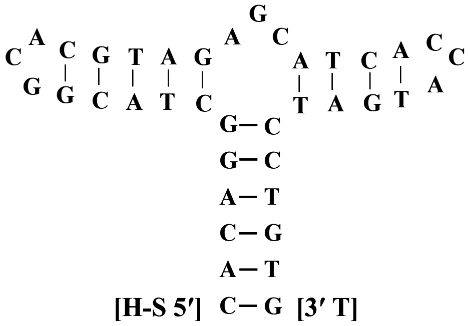

Figure 2-1: The nucleic acid structure of the PDGF-specific aptamer.

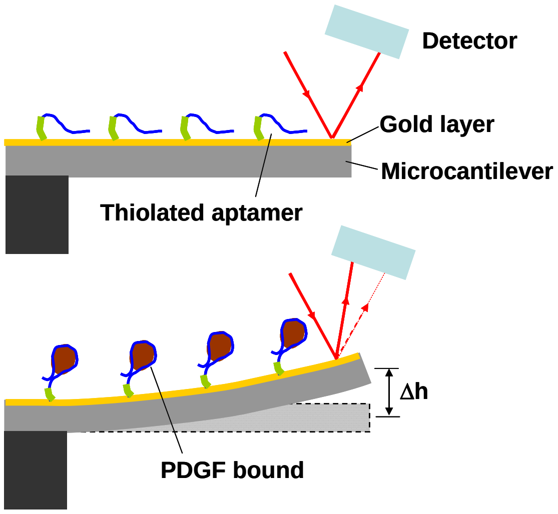

Figure 2-2: Principle of the microcantilever-based detection of aptamer-PDGF binding.

2.2.2 Device Design, Fabrication and Testing Setup

Our approach is based on a cantilever-based microfluidic chip coupled to a Peltier thermoelectric module (Figure 2-3). The chip mainly consists of three functional layers: a silicon chip featuring the Parylene microcantilever, a PDMS spacer layer defining the microfluidic chamber, and a glass plate with an ITO temperature sensor. The inlet and outlet tubings are embedded in the PDMS spacer layer to allow continuous flow during experiments. Temperature is controlled in closed loop by adjusting the voltage applied to the Peltier module (which allows both heating and cooling by thermoelectric effects [118]) according to the feedback from the *in-situ* ITO temperature sensor. Transparent ITO patterned glass is chosen for unobstructed optical detection of microcantilever deflection. Parylene is employed as a device material to exploit benefits such as higher potential detection sensitivity due to its low Young's modulus and excellent chemical inertness.

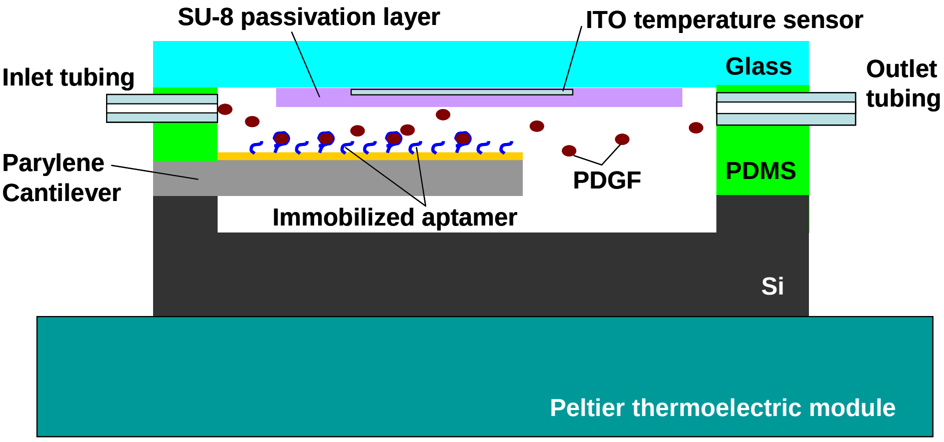

Figure 2-3: Design schematic of the cantilever-based microfluidic device for characterization of temperature-dependent aptamer-PDGF binding.

The fabrication of the microcantilever chip began on an oxide-precoated silicon wafer. Multiple cantilevers were included in the chamber for redundancy. First, anchor cavities surrounding the cantilevers were defined and etched by KOH to a depth of approximately 20 μm (Figure 2-4a). Then the pits underneath the cantilevers were defined, followed by uniformly coating a 6-μm thick Parylene film via chemical vapor deposition (CVD) (Figure 2-4b). Cantilevers were then patterned by oxygen-plasma reactive ionic etching (RIE), and coated with a Cr/Au (chromium/gold, 5/45 nm) thin film via thermally evaporation and wet etching (Figure 2-4c). Subsequently, the pits defined above were completed by Xenon difluoride (XeF_2) gas-phase etching to fully release the cantilevers (Figure 2-4d). In parallel, the ITO temperature sensor was patterned on an ITO-coated glass slide (Delta Technologies, CB-50IN) by wet etching using 25% HCl (Figure 2-4e) and passivated by a 1.5-μm thick SU-8 photoresist layer (Figure 2-4f). Also, a 250-μm thick PDMS spacer layer defining the microfluidic chamber was fabricated using a replica molding technique [119] (Figure 2-4g). Finally, the microcantilever chip, the PDMS spacer layer, and the ITO glass slide were bonded together in sequence with the interfaces treated with oxygen plasma and reinforced by gluing (Figure 2-4h). The inlet and outlet solution lines were coupled to the device by capillary tubings inserted into the PDMS spacer layer. The resulting chip package was attached to a Peltier module (Melcor) using a thermally conductive glue (Omega Engineering). Figure 2-5a shows a packaged device with 17 microcantilevers in a circular chamber and Figure 2-5b the micrograph of a representative single cantilever.

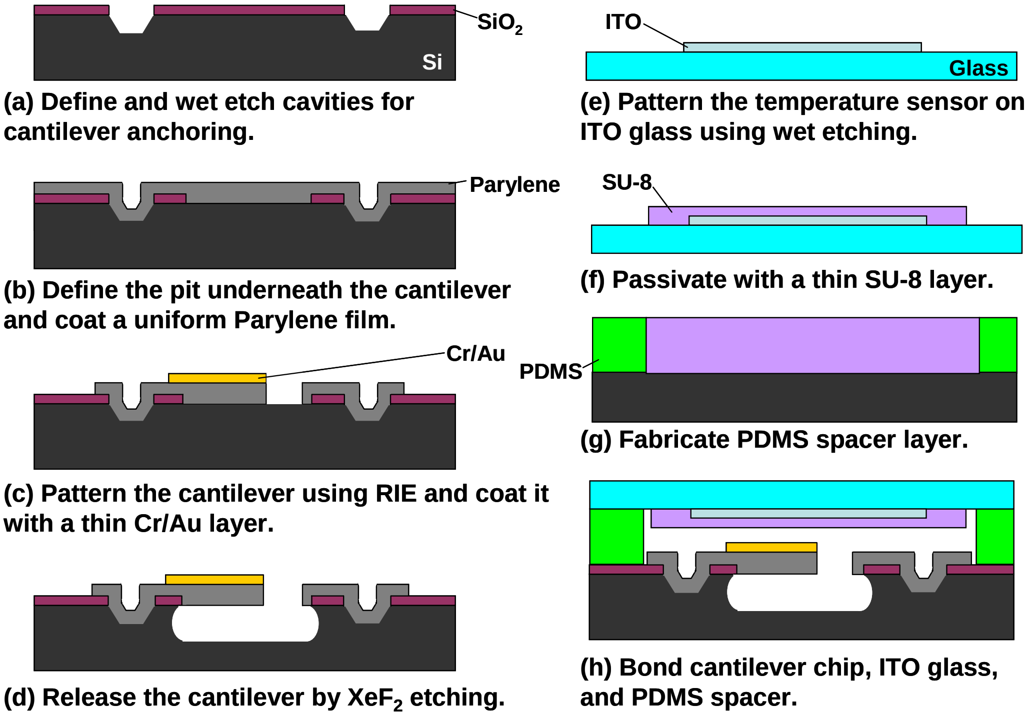

Figure 2-4: Fabrication process of the microcantilever device.

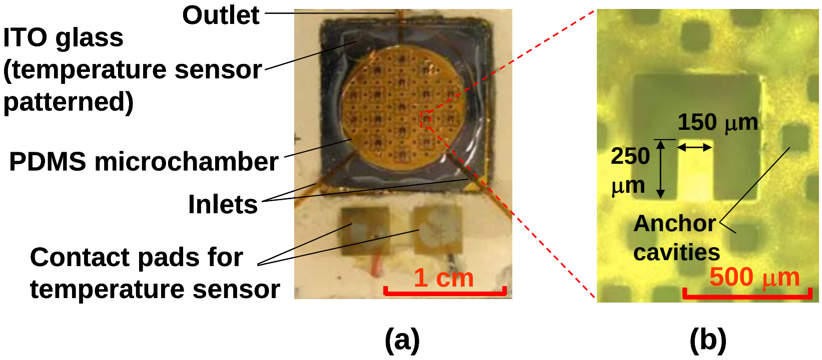

Figure 2-5: Fabricated microcantilever device. (a) Image of a packaged device. (b) Micrograph of a representative single cantilever.

As shown in Figure 2-6, the experimental setup mainly consisted of electrical instruments for temperature control, and an optical lever for optical detection. The temperature inside the reaction chamber of the chip was maintained at a desired setpoint using the Peltier thermoelectric module driven by a DC power supply (Agilent E3631) and the ITO temperature sensor measured by a digital multimeter (Agilent 34410A), regulated under closed-loop proportional-integral-derivative (PID) control algorithm. During experiments, the two inlets were connected to two parallel solution lines driven by syringe pumps (New Era Pump Systems NE-1000) which allowed convenient switch between two different injected solutions. For optical detection, a home-built optical lever system was used, in which a laser beam from a diode laser generator was directed to the gold surface of a cantilever and reflected to a photosensitive detector (PSD, Coherent). The signal was amplified by a PSD amplifier (Photonics OT-301) and then measured by a nanovoltmeter (Agilent 34420A). The on-chip temperature control and optical signal acquisition were computer-automated and monitored by a LabVIEW-based program.

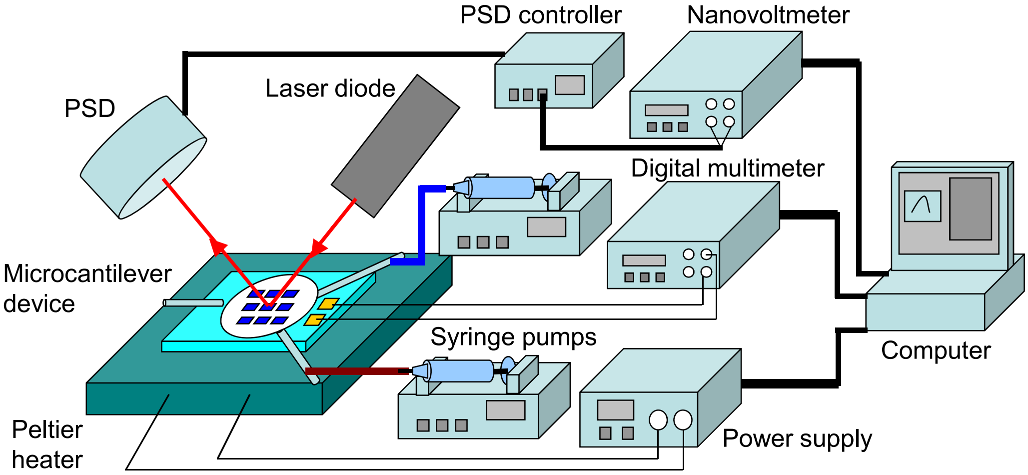

Figure 2-6: Experimental setup for the temperature control, optical detection and signal acquisition in the cantilever-based microfluidic device.

2.2.3 Materials and Experimental Procedure

An isoform of PDGF, PDGF-BB (Sigma Aldrich), was chosen as a model analyte in our experiments. PDGF-BB was prepared in PBSM buffer (10.1 mM Na_2HPO4, 1.8 mM KH_2PO4, 137 mM NaCl, 2.7 mM KCl, and 1 mM $MgCl_2$, pH 7.4).The PDGF-specific aptamer was obtained from IDT DNA and prepared in sterile water (Fisher

Scientific). All solutions were degassed prior to introduction into the microfluidic chambers to avoid inducing air bubbles. Meanwhile, the microcantilever device was pre-cleaned with acetone, ethanol, and sterile water sequentially. To immobilize aptamer molecules on the cantilever surface, 3 μM aptamer solution was allowed to perfuse through the reaction chamber overnight at a constant flow rate of 0.5 μL/min at 4 °C. During the aptamer-PDGF association and dissociation experiments, PBSM buffer and 5 nM PDGF solutions respectively perfused through the reaction chamber via the device's two microfluidic inlets as follows. The chamber was initially flushed with PBSM buffer and then infused with PDGF solution, initiating the association between PDGF and the aptamer as detected via the cantilever deflection. After the association reached equilibrium, the infusion was switched back to PBSM buffer to enable the dissociation process. Throughout the experiments, the flow rate of both PBSM buffer and PDGF solution was maintained at 10 μL/min, which was chosen to allow an acceptable mass transport rate at which PDGF molecules were accessed by the aptamer-functionalized surface [120], while limiting the flow-induced shear force on the molecules that could affect the binding activity [121]. After the measurement, the system was regenerated by removing any PDGF molecules that remained on the surface by 4 M urea and 15 mM EDTA and then rinsing with PBSM buffer. The baseline in response signal, i.e., the PSD output of the optical detection system with no occurrence of the aptamer-PDGF affinity binding, was measured with PBSM buffer alone flowing through the microchamber.

2.2.4 Monovalent Binding Kinetic Model

We consider a monovalent model for the equilibrium affinity binding between the immobilized receptor (of concentration [R]) and the target analyte (of concentration [A]) to form a complex (of concentration [RA]) [122]:

$$[R]+[A] \underset{k_{\mathrm{off}}}{\overset{k_{\mathrm{on}}}{\rightleftharpoons}} [RA] \tag{2-1}$$

where k_{on} and k_{off} are the association and dissociation rate constants, respectively. The net rate of complex formation varies with time according to the following differential equation:

$$\frac{dy}{dt} = k_{\mathrm{on}}[A](y_{\max} - y) - k_{\mathrm{off}}\, y \tag{2-2}$$

where y and $y_{\max}$ respectively represent the observed response signals respectively corresponding to the complex concentration [RA] and saturation complex concentration $[RA]_{\max}$ (i.e., the asymptotic value of [RA] at infinite time) for a given concentration of injected analyte [A].

In flow-through mode as used in the experiments, either the target analyte solution (for association) or pure buffer (for dissociation) is introduced continuously to the cantilever. At a sufficiently large flow rate, the analyte concentration [A] can be assumed to be a constant c in the association process, or 0 in the dissociation process [122]. Eq. (2-2) thus reduces to the following equations, respectively, for the association and dissociation processes:

$$\frac{dy}{dt} = k_{\mathrm{on}} c(y_{\max} - y) - k_{\mathrm{off}}\, y \tag{2-3}$$

$$\frac{dy}{dt} = -k_{\mathrm{off}}\, y \tag{2-4}$$

Solving Eq. (2-3) (using initial condition $y = 0$ at $t = 0$) yields the time-dependent association response signal:

$$y = y_{\max}\frac{c}{K_{\mathrm{d}}+c}(1-e^{-(k_{on}c+k_{off})t}) \tag{2-5}$$

where $K_{\mathrm{d}} = \frac{k_{\mathrm{off}}}{k_{\mathrm{on}}}$ is the equilibrium dissociation constant.

For the dissociation process, solving a Eq. (2-4) yields

$$y = y_0 e^{-k_{\mathrm{off}}t} \tag{2-6}$$

where y_0 is the initial signal at the beginning of the dissociation process ($t = 0$). Using Eqs. (2-5) and (2-6), the kinetic and equilibrium binding constants (k_{on}, k_{off}, and K_{d}) can be obtained from the time-resolved measurement signal y.

2.3 Results and Discussion

2.3.1 Aptamer-PDGF Binding and Selectivity to PDGF

We first validated the specificity of PDGF binding in our device with three sets of control experiments. These include (1) introduction of PDGF solution into the reaction chamber with an aptamer-free cantilever surface, followed by PBSM buffer; (2) introduction of only PBSM buffer into the reaction chamber of an aptamer-functionalized cantilever; and (3) introduction of a lysozyme (egg white, Sigma Aldrich) solution to an aptamer-functionalized cantilever, followed by PBSM buffer. Here lysozyme, which has comparable molecular weight (14.3 kDa) to PDGF (25 kDa), was used as a non-binding protein for testing the aptamer specificity.

Figure 2-7 shows the signal traces of the control experiments, combining the phases of sample injection and PBSM buffer injection, compared with a representative trace of aptamer-PDGF binding undergoing the same phases. Throughout the experiments, this device showed a noise level of less than ±2 mV and repeatability within 10%. In the absence of either aptamer or PDGF, no signal above noise level was detected upon the presence of biomolecules or buffer solution. More importantly, for aptamer-PDGF binding, there existed an exponential increase to a binding equilibrium corresponding to the introduction of PDGF molecules, and a relatively slow shift back to the original equilibrium upon PBSM buffer injection. Thus, the non-specific binding of PDGF to either surface of the cantilever was generally negligible compared with the affinity binding between aptamer and PDGF.

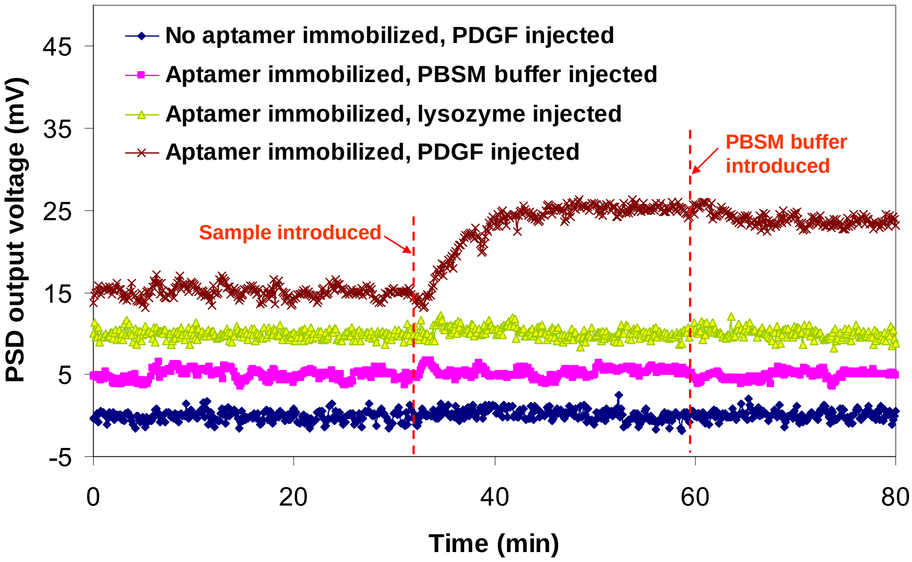

Figure 2-7: Binding specificity demonstrated by association and dissociation signal traces of control experiments in the absence of either aptamer or PDGF, compared with a representative aptamer-PDGF binding trace (all traces intentionally plotted with an offset of 5 mV for clarity).

2.3.2 Characterization of Temperature-Dependent Aptamer-PDGF Binding

Temperature-dependent characterization of the aptamer-PDGF binding was performed by monitoring the association and dissociation processes at temperature varying from 19-37 °C. This temperature range is considered suitable for characterization of aptamer-PDGF interactions since aptamer-based therapeutics typically demand a physiologically relevant temperature up to 37 °C. With our experimental setup, the temperature inside the chamber, indicated by the ITO temperature sensor, was consistently controlled within ± 0.3 °C at setpoints in the range of 19-37 °C. The experimental data were then fitted to the monovalent binding kinetic model given in Eqs. (2-5) and (2-6) to obtain the temperature-dependent kinetic properties of the rate constants for association (k_{on}) and dissociation (k_{off}), and the equilibrium dissociation constant (K_{d}). For each temperature setpoint, we used the GraphPad Prism software [123] to fit the experimental data on the combined dissociation and association processes in a manner that ensures the baseline consistency.

Figure 2-8 shows the experimental signal (baseline subtracted) of aptamer-PDGF association and dissociation processes at controlled temperature setpoints of 19, 25, 31, and 37 °C, as well as the fitted curves to the monovalent binding kinetic model. These data showed a clear shift with temperature, and thus considerable temperature dependence within the aptamer-PDGF interaction. In particular, as the temperature increased from 19 to 37 °C, the characteristic time for the association process to reach equilibrium decreased from approximately 30 to 15 minutes, indicating that the rate of the aptamer-PDGF association process increased with temperature. In addition, the steady-state deflection of the cantilever in equilibrium aptamer-PDGF binding also increased with temperature (Figure 2-8). This indicated a more significant surface stress change on the cantilever, which was primarily caused by a larger fraction of immobilized aptamer molecules that are bound to PDGF molecules. These results suggest that temperatures in the physiological range present an optimal condition for the binding of PDGF to aptamer, which is determined by a combination of aptamer tertiary conformation, molecular orientation, and binding energy, as well as the effect of generally increased Brownian motion at higher temperature.

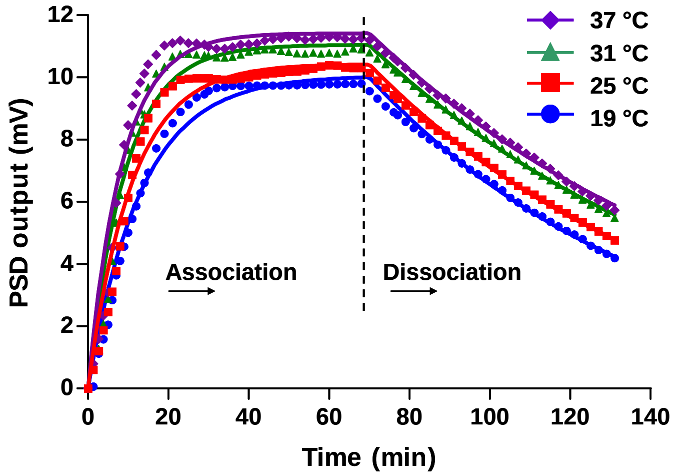

Figure 2-8: The experimental data of association (left) and dissociation (right) processes at 19, 25, 31, and 37 °C and the fitted curves to the monovalent binding kinetic model.

There was a small apparent overshoot in the detected signal before the association process reached equilibrium (Figure 2-8). This could be attributed to the variation in the flow rates during the introduction of PBSM buffer and PDGF solution to the microchamber, which most likely were caused by the difference in the syringe pumps and access channels between PBSM buffer and PDGF solution injections. As the association process was triggered by switching the introduction of PBSM buffer to that of PDGF solution, the variation in flow rate induced a difference in the hydrodynamic force on the cantilever and in turn a slight overshoot in cantilever deflection. However, this did not significantly influence the values of binding parameters obtained from the model (Eqs. (2-5) and (2-6)) to the experimental data.

In the flow-through experiments, the mass transport of biomolecules occurred by convection and diffusion. To assess this effect on the aptamer-PDGF binding in our device, we first estimated the characteristic time for PDGF molecules accessed by the cantilever surface. The rate of molecular transport to the surface is given by the Onsager coefficient of mass transport [120]:

$$k_{\mathrm{m}} \approx \sqrt[3]{\frac{D^2 u}{h^2 b l}} \tag{2-7}$$

where D is the diffusivity of sample biomolecules, u is the flow rate for sample introduction, h is the height of the reaction chamber, and b and l are the width and length of the cantilever. For the experimental data above, $h = 250$ μm, $b = 150$ μm, $l = 250$ μm, and $D \approx 10^{-10}$ m^2/s [124]. Using $u = 10$ μL/min, $k_{\mathrm{m}} = 5.4\times10^{-4}$ m/min, and the time scale for the analyte diffusion was estimated to be $h/k_{\mathrm{m}} = 0.46$ min. Compared with the apparent time scale of aptamer-PDGF association process (approximately 15-30 minutes), it is reasonable to assume that the aptamer-PDGF binding process was not limited by mass transport at this flow rate [120].

2.3.3 Temperature-Dependent Kinetics of Aptamer-PDGF Binding

We further determined the kinetic and equilibrium binding properties by fitting the monovalent binding model (Eqs. (2-5) and (2-6)) to the experimental data. The temperature dependent kinetic binding rate constants are shown in Figure 2-9. As the temperature increased from 19 to 37 °C, k_{on} increased from 1.3×10^7 to 2.3×10^7 $(\mathrm{M}\cdot\mathrm{min})^{-1}$, while k_{off} decreased from 0.015 to 0.01 min^{-1}. Meanwhile, K_{d}, as shown in Figure 2-10, decreased from approximately 12×10^{-10} M to 5×10^{-10} M as the temperature changed from 19 to 37 °C. This indicates stronger aptamer-PDGF binding, i.e., a more favorable conformational change of the aptamer molecules for the affinity interaction as the temperature approached the physiological values, at which the aptamer was synthetically isolated [20]. Moreover, the decrease of K_{d} with temperature implies that the aptamer-PDGF system becomes more thermodynamically stable as the temperature increases, which typically involves negative Gibbs free energy [4]. These results are consistent with published data using conventional methods (e.g., UV-absorption [20]). The K_{d} values we obtained are higher than those obtained with the aptamer in solution (typically $\sim10^{-10}$ M), which is likely attributable to two reasons. First, the surface-immobilized receptor has restricted conformational flexibility for the analyte to access the entire binding sites [54], and thus may not retain its full solution-based activity [125]. In addition, avidity, in which the binding of analyte molecules with receptor molecules is synergistically stabilized by entropic effects [122], is known to have a noticeable contribution to high-affinity binding systems [55]. In our experiments, the presence of the solid surface may have led to reduced avidity effects because of less efficient diffusion [126] and limited clustering of analyte and receptor molecules [122].

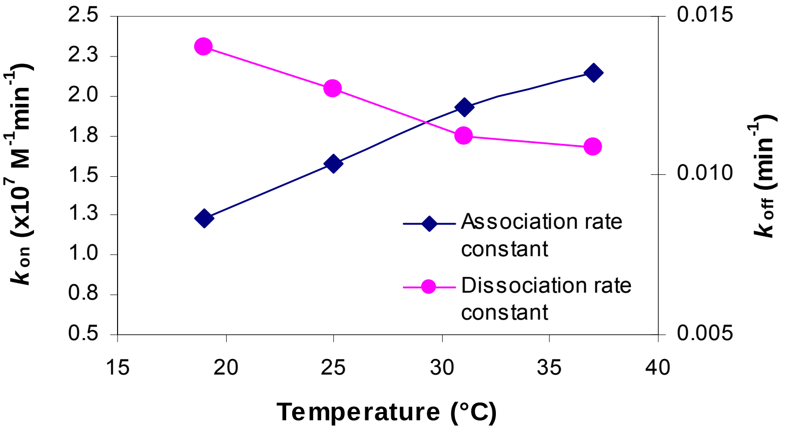

Figure 2-9: Association rate constant (k_{on}) and dissociation rate constant (k_{off}) at controlled temperatures of 19, 25, 31, and 37 °C.

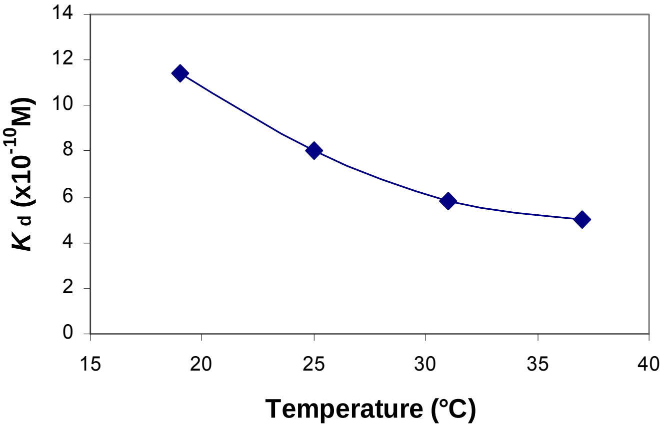

Figure 2-10: Equilibrium dissociation constant (K_d) at controlled temperatures of 19, 25, 31, and 37 °C.

2.4 Conclusions

This chapter presents label-free characterization of temperature-dependent biomolecular affinity binding on solid surfaces using a microcantilever-based device integrating on-chip temperature sensing. The device consists of a Parylene cantilever one side of which is coated with a thin gold film and functionalized with molecules of an affinity receptor to a target analyte. The cantilever is located in a PDMS microfluidic chamber which is integrated with a transparent ITO thin-film resistive temperature sensor on a glass slide. The ITO sensor allows for real-time measurements of the temperature inside the chamber with unobstructed optical access for reflection-based optical detection of the cantilever deflection. The device is situated on a Peltier thermoelectric module, which, in conjunction with the integrated ITO sensor, is used to control the chamber temperature based on a closed-loop PID algorithm. To test the temperature-dependent binding between the target and receptor, the temperature of the chamber is maintained at a constant setpoint, while the analyte solution is continuously infused through the chamber. The measured cantilever deflection is used to determine the thermodynamic properties associated with the target-receptor binding according to a monovalent binding kinetic model.

We studied the temperature-dependent affinity binding between PDGF, a protein regarded as a ubiquitous mitogen and chemotactic factor in angiogenesis, and an affinity aptamer. We first verified the detection specificity using this device and then systematically characterized the aptamer-PDGF association and dissociation processes with the chamber temperature controlled in the range of 19-37 °C. Quantitative binding properties were obtained, indicating strong temperature dependence of the binding of PDGF to the aptamer. As the temperature increased from 19 to 37 °C, the association rate constant increased from 1.3×10^{7} to 2.3×10^{7} $(\mathrm{M\cdot min})^{-1}$, while dissociation rate constant decreased from 0.015 to 0.01 min^{-1}. This corresponds to a decrease of the equilibrium dissociation constant from approximately 12×10^{-10} M to 5×10^{-10} M. These results provide a starting point for label-free characterization of temperature-dependent biomolecular interactions, and can potentially used for the screening and optimization of inhibiting ligands of PDGF and other target molecules.

Chapter 3 Microfluidic Approach to Characterization of Temperature-Dependent Biomolecular Activity with Single-Molecule Resolution

This chapter presents a microfluidic approach for single-molecule studies of the temperature-dependent behavior of biomolecules, using a platform that combines microfluidic sample handling, on-chip temperature control, and total internal reflection fluorescence (TIRF) microscopy of surface-immobilized biomolecules. With efficient, rapid, and uniform heating by microheaters and *in situ* temperature measurements within a microfluidic flowcell by micro temperature sensors, closed-loop, accurate temperature control is achieved. To demonstrate its utility, the temperature-controlled microfluidic flowcell is coupled to a prism-based TIRF microscope and is used to investigate the temperature-dependence of ribosome and transfer RNA (tRNA) structural dynamics that are required for the rapid and precise translocation of tRNAs through the ribosome during protein synthesis. Our studies reveal that the previously characterized, thermally activated transitions between two global conformational states of the pre-translocation (PRE) ribosomal complex persist at physiological temperature. In addition, the temperature-dependence of the rates of transition between these two global conformational states of the PRE complex reveal well-defined, measurable, and disproportionate effects, providing a robust experimental framework for investigating the thermodynamic activation parameters that underlie transitions across these barriers.

3.1 Background

Single-molecule studies of biochemical systems, in contrast to ensemble measurements, involve direct observation and analysis of individual biomolecules, allowing access to mechanistic information that is often obscured in ensemble measurements. Although an ability to perform single-molecule measurements as a function of well-defined temperature is critical for studying the energetics of biomolecular behavior, measurement of the temperature-dependence of single-biomolecular behavior remains a major challenge [73]. Conventional temperature control methods [70, 127, 128] in single-molecule investigations are generally cumbersome, slow, and relatively inaccurate [74, 75]. These limitations in temperature control are a major hindrance to fully harnessing the power of single-molecule investigations.

Microfluidic technology can greatly facilitate single-molecule experiments by providing on-chip fluid handling with drastically reduced sample consumption, and more importantly, well-controlled micro- or nanoscale environments in which biomolecules are effectively manipulated and analyzed. Despite the insights that have been gleaned through the use of the microfluidic tools, the influence of temperature on individual biomolecular behavior remains poorly characterized due to the lack of accurate temperature control within single-molecule detection systems. For example, a microfluidic device uses a circulating water bath and no temperature sensing in the detection channels [112]; this open-loop temperature control strategy however does not allow adequate accuracy and is rather cumbersome in operation, in particular during the transition between temperature setpoints.

Microfabricated thin-film heaters and temperature sensors for efficient on-chip temperature control [114] have been widely used in microfluidic devices such as polymerase chain reaction (PCR) platforms [129]. However, such thermal elements have not yet been successfully incorporated into single-molecule fluorescence microscopy systems for studies of temperature dependent properties of single biomolecules. Indeed, existing microfluidic on-chip temperature control configurations encompass several shortcomings that make them poorly suited for integration into existing single-molecule fluorescence microscopy systems. For example, non-uniform temperature distributions arising from localized heating (typical characteristic of on-chip temperature control configurations) are a critical issue that could make the controlled temperatures within the detection area inaccurate. Moreover, non-uniform temperature distributions could introduce heterogeneity across the individual molecules being observed, resulting in a shifted and/or broader distribution of transition parameters obtained at a particular temperature setpoint, possibly complicating data analysis. In addition, the majority of existing microfluidic on-chip temperature control configurations is incompatible with single-molecule fluorescence microscopy systems by obstructing the required optical path. Finally, thermally induced defocusing arising from heat transfer to the microscope objective during the heating-enabled observation period is a significant issue that remains unaddressed in the design of currently available microfluidic on-chip temperature control configurations.

In this chapter, we report a microfluidic approach that overcomes the limitations of existing on-chip temperature control configurations and successfully integrates facile and accurate on-chip temperature control within a standard TIRF microscopy system. As TIRF has emerged as a prominent method for single-molecule studies (because of its high sensitivity and signal-to-noise ratio as well as wide-field detection capabilities [130]), this approach provides a platform which readily enables studies of the temperature-dependence of a wide range of biomolecular activity with single-molecule resolution. The approach employs closed-loop temperature control via on-chip heating and *in situ* temperature sensing of a minimized biological sample volume. To meet the requirements of single-molecule measurement resolution, microheaters are placed on either side of a microchannel, and temperature sensors with sufficiently small footprints are located in the center of the microchannel. This configuration ensures that the region of the chip heated by the microheaters is much larger than the TIRF microscopy detection volume, thus eliminating non-uniform temperature distributions within the detection volume. Moreover, the placement of microheaters on either side of a microchannel on a glass substrate allows for an adequately large and optically transparent observation area that is fully compatible with TIRF microscopy and ensures that temperature gradients primarily occur within the depth of the microchannel, such that the conduction of heat through the glass substrate to the in-contact microscope objective is negligible. Our approach therefore provides a low-cost and compact experimental platform that can be directly used for TIRF microscopy-based, temperature-dependent, single-molecule investigations, eliminating the need to control the temperature of the entire setup or the physical space in which the experiment is performed.

We demonstrate the utility of our approach by performing a temperature-dependent, single-molecule fluorescence resonance energy transfer (FRET) study of the ribosome, the biomolecular machine that is responsible for protein synthesis, or translation, in all living cells [5, 36, 131]. Because the efficiency of FRET depends on the distance between donor and acceptor fluorophores (typically engineered into the biomolecule of interest), single-molecule FRET (smFRET) experiments provide a powerful tool for investigating the conformational dynamics of biomolecules [46, 132]. Previously, we have developed and used a smFRET signal between the ribosome and a ribosome-bound tRNA substrate to investigate the mechanism through which the ribosome achieves the rapid and precise translocation of tRNAs through multiple ribosomal binding sites that is required during protein synthesis [131]. These previous smFRET studies, all performed at room temperature, have demonstrated that pre-translocation (PRE) ribosome-tRNA complexes undergo spontaneous and thermally activated fluctuations between two discrete and structurally well-characterized global conformational states, termed global state 1 (GS1) and global state 2 (GS2). Because GS2 is an authentic on-pathway intermediate in the translocation reaction [6, 133, 134], thermally activated fluctuations between GS1 and GS2 may play a critical role in the translocation mechanism. Lacking smFRET data recorded at physiological temperature (37 °C for the *Escherichia coli* system under investigation here), however, it is presently unknown whether the kinetic barriers associated with GS1→GS2 and GS2→GS1 transitions persist *in vivo*. Here we unambiguously demonstrate that at the physiologically relevant temperature of 37 °C, PRE complexes continue to spontaneously fluctuate between GS1 and GS2. This observation demonstrates that under physiologically relevant conditions, the free-energy landscape of the PRE complex is not entirely flat and that functionally critical GS1→GS2 and GS2→GS1 transitions require overcoming measureable kinetic barriers. More importantly, extension of the proof-of-principle experiments reported here will readily allow detailed investigations of the thermodynamic activation parameters that govern this essential structural rearrangement of the translating ribosome. More generally, the results we present here demonstrate the potential of our approach for studying the energetics of biomolecular structural dynamics and biochemical reactions at the single-molecule level, thus expanding the toolkit that is available for mechanistic studies of Nature's molecular machines.

3.2 Materials and Methods

3.2.1 Design

Our microfluidic approach couples a temperature-controlled microfluidic flowcell to a prism-based TIRF microscope. The microfluidic flowcell comprises a set of parallel microchannels sandwiched between a quartz microscope slide and a glass coverslip, onto which thermal control elements are integrated (Figure 3-1a). The microchannels have cross-sectional dimensions of approximately 1 mm × 80 μm and are 20 mm in length. The centerlines of adjacent channels are separated by a distance of 4.3 mm. The thermal control elements on the coverslip surface include thin-film resistive microheaters and temperature sensors (Figure 3-1b). In accordance with the confinement of parallel microchannels, the microheaters are distributed evenly across the entire coverslip in order to provide uniform heating, while the sensors are located directly underneath the microchannels to accurately probe the surface temperature in real time. Each heater is a serpentine line 200 μm wide, covering a 20 mm × 2 mm square area next to the channel area, and typically has an electric resistance of approximately 200 Ω at room temperature. Each temperature sensor is also a serpentine line located at the center of the corresponding channel area, with an approximate coverage area of 5 mm × 120 μm and a typical electric resistance of approximately 120 Ω at room temperature. This design affords a relatively uniform temperature distribution within each microchannel, whose small depth (80 μm) allows the temperature of the fluorescent detection area on the quartz slide to be measured by the temperature sensor on the glass coverslip with acceptable accuracy.

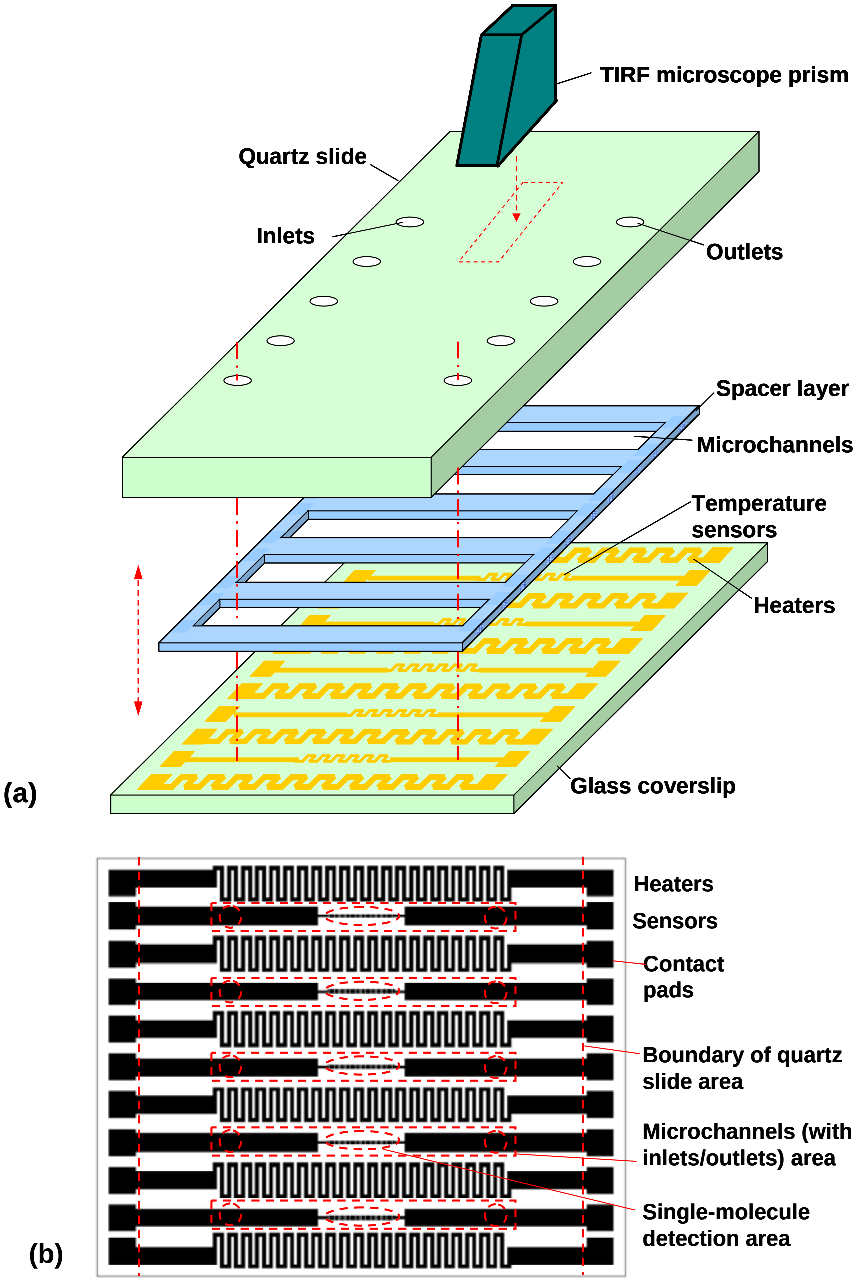

Figure 3-1: Design schematic of the microfluidic approach to temperature-controlled single-molecule studies. (a) A temperature-controlled microfluidic flow cell coupled to a prism-based TIRF microscope. (b) Design layout of microheaters and temperature sensors on the coverslip.

3.2.2 Fabrication and Functionalization

The fabrication of the microfluidic chip (Figure 3-2a) began on a glass coverslip with patterning a double layer of LOR 3A and Shipley S1805 photoresists (both from MicroChem, Inc.) to define the heaters and temperature sensors. A 10-nm chromium film and a 100-nm gold film were then deposited via electron-beam evaporation, and patterned with a lift-off process to form the heaters and temperature sensors. A 200-nm silicon nitride passivation layer was next deposited using plasma enhanced chemical vapor deposition (PECVD). Contact pads for the heaters and temperature sensors were defined by photolithography and exposed by reactive ion etching (RIE).

A quartz microscope slide containing drilled inlet and outlet ports was cleaned, aminosilanized, and subsequently derivatized with a mixture of *N*-hydroxysuccinimidyl (NHS) ester-derivatized polyethylene glycol (PEG) and a bifunctionalized NHS ester-PEG-biotin (Laysan Bio, Inc.)[5, 131, 135]. This multi-step treatment creates an optically clean, low background fluorescence, PEG- and PEG-biotin-derivatized quartz surface that is randomly and sparsely populated with biotin groups. Biotinylated biomolecules can then be immobilized and spatially localized using a biotin-streptavidin-biotin bridge (Figure 3-2b). The microfabricated coverslip is bonded to the passivated and functionalized quartz slide using a spacer layer of double-sided tape (approximately 80 μm thick) that defines the microchannels. Multiple parallel channels are incorporated to allow several biochemical experiments to be performed on one microfluidic chip. A packaged device with five microchannels is shown in Figure 3-3a with the details of the chip near the detection area shown in Figure 3-3b.

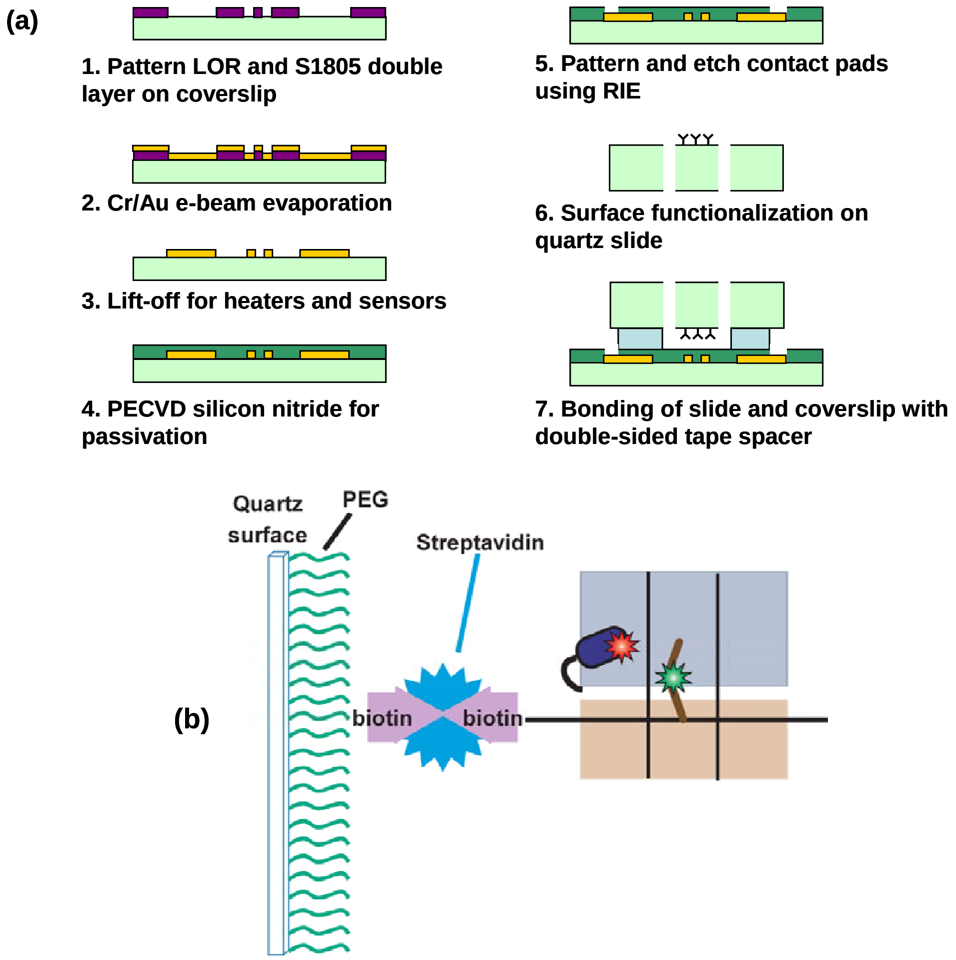

Figure 3-2: (a) Fabrication and surface functionalization processes. (b) Surface immobilization strategy: quartz flow cell is first passivated with a mixture of PEG and PEG-biotin and then incubated with streptavidin prior to use. PRE-A ribosomal complexes carrying biotinylated-mRNA are then immobilized onto the surface of the streptavidin-derivatized flow cell via a biotin-streptavidin-biotin bridge.

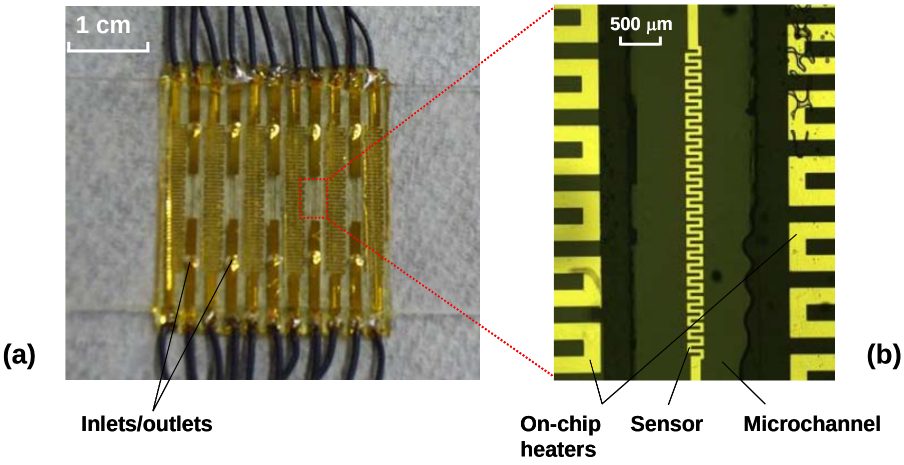

Figure 3-3: (a) Photograph of a packaged device; and (b) micrograph of micro-heaters and a temperature sensor.

3.2.3 *Materials*

A single-cysteine variant of *Escherichia coli* ribosomal protein L1 was fluorescently labeled with a Cy5 acceptor fluorophore ((Cy5)L1) and reconstituted into mutant *E. coli* ribosomes lacking ribosomal protein L1 as previously described [36, 37, 131]. *E. coli* tRNA^{Phe} was labeled with a Cy3 donor fluorophore ((Cy3)tRNA^{Phe}) at the naturally occurring 3-(3-amino-3-carboxy-propyl) uridine residue at position 47 within the central fold, or elbow, domain of the tRNA body and aminoacylated with phenylalanine as previously described [36, 37, 131]. Ribosomes with (Cy5)L1 were enzymatically initiated onto a 5'-biotinlated mRNA and enzymatically elongated by one amino acid such that they carried fMet-Phe-(Cy3)tRNA^{Phe} at the P site [131]. Ribosomal elongation complexes prepared in this manner were purified by sucrose density gradient ultracentrifugation [36, 37, 131] and were subsequently immobilized onto the surface of the streptavidin-derivatized microchannel.

Surface-immobilized ribosomal elongation complexes were incubated in 1 mM puromycin in Tris-Polymix buffer (50mM Tris-OAc, 100mM KCl, 15mM $Mg(OAc)_2$, 5mM NH_4OAc, 0.5mM $Ca(OAc)_2$, 10mM 2-mercaptoethanol, 5mM putrescine, and 1mM spermidine) [131] supplemented with an oxygen scavenging system (9300 μg/mL glucose oxidase, 40 μg/mL catalase and 1% β-D-glucose) [131] and a triplet state quencher cocktail (1mM 1,3,5,7-cyclooctatetraene (Aldrich) and 1mM *p*-nitrobenzyl alcohol (Fluka)) [36, 131] for 5 min at room temperature. Puromycin is a ribosome-targeting antibiotic that mimics the 3'-terminal residue of an aminoacyl-tRNA, binds to the ribosomal A site, participates as the acceptor in the peptidyl transfer reaction, and subsequently dissociates from the ribosome, carrying the nascent polypeptide with it [131]. The resulting puromycin-reacted ribosomal complex contains a deacylated P-site $tRNA^{Phe}$ and serves as an analog of an authentic PRE complex which we designate as PRE^{-A} [131].

3.2.4 Experimental Method

smFRET measurements were performed on a laboratory-built, prism-based TIRF microscope based on an inverted fluorescence microscope (Nikon TE2000-U) and using a diode-pumped solid-state 532-nm laser (CrystaLaser, Inc.) as an excitation source and a Cascade II:512B electron multiplying charge-coupled device (EMCCD) camera (Photometerics, Inc.) as a detector. Simultaneous detection of the fluorescence emission of both Cy3 and Cy5 fluorophores for 100-200 individual, spatially-resolved PRE^{-A} complexes over an observation area of 60×120 μm^2 was achieved using a PlanApo 1.2 numerical aperture 60× water immersion objective (Nikon, Inc.), optically separating the Cy3 and Cy5 emission signals using a Dual-View image splitting device (Photometrics, Inc.), and simultaneously imaging the Cy3 and Cy5 emission signals on the two halves of the 512×512 pixel CCD chip within the Cascade II:512B EMCCD camera. Cy3 and Cy5 emission signals arising from single PRE^{-A} complexes were collected at a time resolution of 50 ms/frame. Single PRE^{-A} complexes were identified and Cy3 and Cy5 emission intensity *versus* time trajectories were extracted using the MetaMorph software suite (Molecular Devices) as previously described [131]. Using MATLAB, raw Cy3 and Cy5 emission intensity *versus* time trajectories were baseline corrected, corrected for bleed-through of the donor signal into the acceptor channel (typically ~7%), and used to calculate smFRET *versus* time trajectories using $I_{Cy5}/(I_{Cy3}+I_{Cy5})$, where I_{Cy3} and I_{Cy5} are the fluorescence intensities of Cy3 and Cy5, respectively, as previously described [131].

In TIRF microscopy, a thin (100-200 nm) electromagnetic evanescent field is generated by total internal reflection at the interface between the quartz slide and the aqueous buffer within the flowcell, yielding highly specific excitation of donor fluorophores that are covalently linked, or otherwise bound, to surface-immobilized biomolecules [5, 131]. Fluorescence emission from both donor and acceptor fluorophores within individual spatially separated and localized molecules are collected through a 1.2 numerical aperture/×60 water-immersion objective (Nikon, Inc.), separated by a Dual-View image splitting device and imaged onto the two halves of the CCD chip (Figure 3-4). The temperature inside a microchannel selected for single-molecule measurements (below) was maintained at a desired setpoint using a closed-loop control of the on-chip heaters and temperature sensors. As shown in Figure 3-4, the two heaters immediately adjacent to the microchannel, driven by a DC power supply (Agilent E3631), were used to heat the microchannel. The microchannel temperature was measured using the temperature sensor within the microchannel by a digital multimeter (Agilent 34420A). The load current in the heaters was adjusted according to the measured temperature using a PID control algorithm implemented by a LabVIEW (NI Instruments) program on a personal computer.

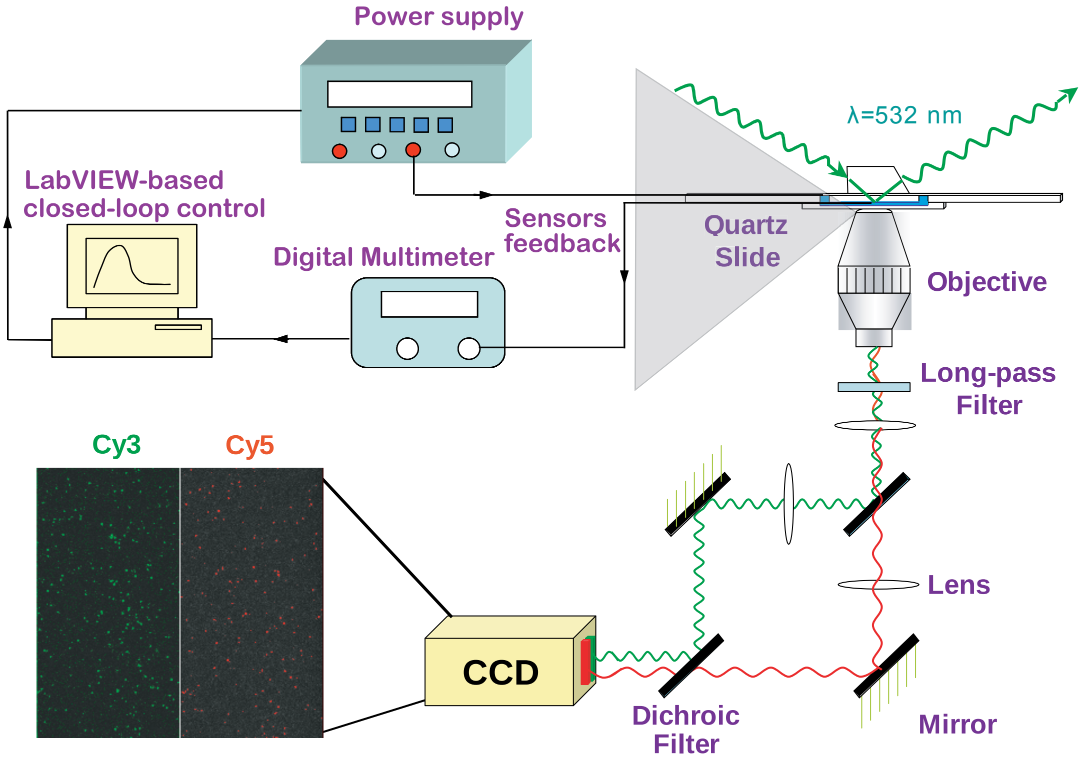

Figure 3-4: Single-molecule detection scheme within a prism-based inverted TIRF microscope and closed-loop temperature control utilizing on-chip heaters and temperature sensors.

3.3 Results and Discussion

3.3.1 On-Chip Temperature Control

To assess the temperature control capability of our design, including the accuracy of the temperature setpoint and the thermal response of the microfluidic flowcell, we first calibrated the on-chip temperature sensors based on the linear relationship between the sensor resistance and temperature. In particular, Resistive temperature sensors can be represented in terms of a linear relationship between the sensor resistance and temperature:

$$R = R_0[1+\alpha(T-T_0)] \tag{3-1}$$

where R is the sensor resistance at temperature T and R_0 the sensor resistance at a reference temperature T_0, with α the temperature coefficient of resistivity (TCR) of the sensor. To determine the parameters in this relationship, we measured the sensor resistance at a series of temperatures. This is accomplished by placing the microchip in a thermal environmental chamber (Delta 9023, Delta Design) maintained at a known temperature. Typical measurement results are shown in Figure 3-5, from which we can observe a highly linear relationship between resistance and temperature as expected from Eq. (3-1). A least-squares linear fit of Eq. (3-1) to the measurement data allowed for the determination of R_0, T_0, and α. For example, with data shown in Figure 3-5, the parameters were determined to be R_0 = 117.795 Ω at T_0 = 24.7 °C, with $\alpha = 2.01\times10^{-3}$ 1/°C.

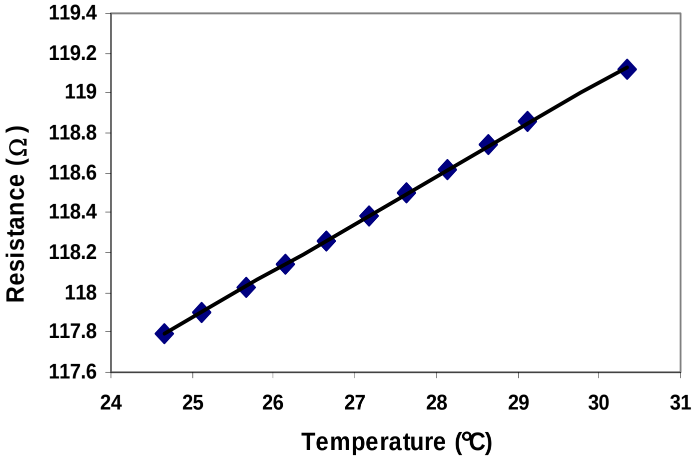

Figure 3-5: Measured electric resistance of a temperature sensor, showing highly linear dependence on temperature.

We subsequently characterized the closed-loop temperature control scheme described above. Figure 3-6 reports the temperature tracking history of a testing process in which the temperature inside a microchannel filled with Tris-Polymix buffer [5, 131] was controlled at the desired setpoints of 22, 25, 28, 31, 34, and 37 ˚C. As can be seen from Figure 3-6, the microchannel temperature could be rapidly increased from one temperature setpoint to another by the PID-based temperature controller with no appreciable overshoot. Thermal equilibrium at each temperature setpoint could be achieved within less than 30 seconds (Figure 3-6), and the steady-state temperature remained within approximately 0.01 ˚C of the desired temperature setpoint for periods of up to an hour (Figure 3-6). These characteristics are considered sufficient for real-time single-molecule fluorescence imaging of biochemical reactions and real-time fluorescence tracking of biomolecules [74].

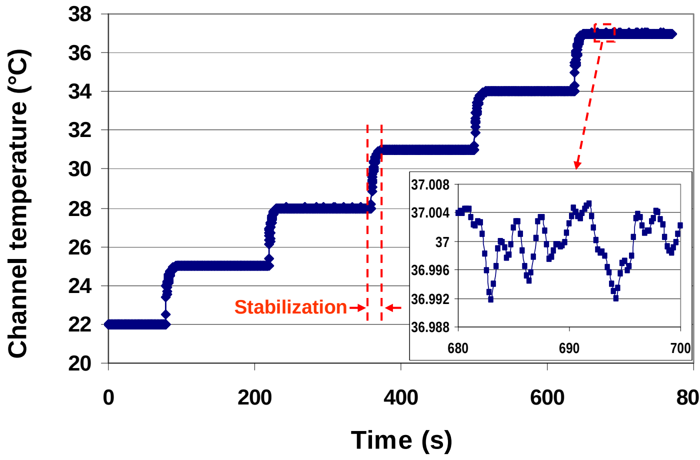

Figure 3-6: Time-resolved tracking of the temperature inside a microchannel at setpoints of 22, 25, 28, 31, 34, and 37 °C.

3.3.2 *Temperature Uniformity in a Microchannel*

The temperature sensor allows measurement of the average temperature in the microchannel, but does not provide information on the temperature distribution within the microchannel. Thus, we have evaluated the uniformity of the temperature within the microchannel, in particular in the finite TIRF measurement volume, using numerical simulation [136]. The simulation model considers three-dimensional heat conduction in the buffer (thermal conductivity: 0.6 W/m·K) contained in the microchannel, which are formed by the coverslip and quartz substrates (thermal conductivity: 1.4 W/m·K), as well as the double-sided tape spacer layer (Acrylic, thermal conductivity: 0.2 W/m·K). Given the small length scale of the microchannel, natural convection within the liquid buffer is estimated to be negligible. Electric power is applied uniformly to each microheater adjacent to the microchannel. The boundary conditions are given by natural convection on the top and bottom surfaces of the substrates, which are surrounded by air at room temperature (22 °C). The natural convection heat transfer coefficient h is determined by [137]

$$\frac{hL}{k} = C\left(\frac{g\beta(T_s - T_\infty)L^3}{\nu\alpha}\right)^m \tag{3-2}$$

where T_s is the average surface temperature (approximately given by the setpoint temperature), and L the characteristic dimension of the quartz slide and the glass coverslip (taken to be 1 cm). In addition, g is the gravitational constant, while k, ν, α, and β are the thermal conductivity, kinematic viscosity, thermal diffusivity, and thermal expansion coefficient of air, respectively, evaluated at the average air film temperature $(T_s+T_\infty)/2$. Using the empirical parameter values $C = 0.621$ and $m = 0.2$ for the top surface [137], and $C = 0.495$ and $m = 0.2$ for the bottom surface [137], the heat transfer coefficient h is estimated to be 8.83 and 5.65 $\mathrm{W/m^2 \cdot K}$ for the top and bottom surfaces, respectively.

The model is solved with finite element methods using COMSOL Multiphysics (COMSOL, Inc.) to obtain the temperature distributions in the microchannel. As an example, the simulated temperature distributions when the channel is heated to a setpoint temperature of 37 °C are shown in Figure 3-7. It can be seen that temperature variations within a 1-mm section of the microchannel, corresponding to the area covered by the temperature sensor, are smaller than 0.01 and 0.03 °C, respectively, in directions perpendicular to and along the channel's longitudinal axis. This suggests that the temperature is sufficiently uniform within the TIRF observation volume within the microchannel and can be accurately obtained from the average temperature measurements by the temperature sensor.

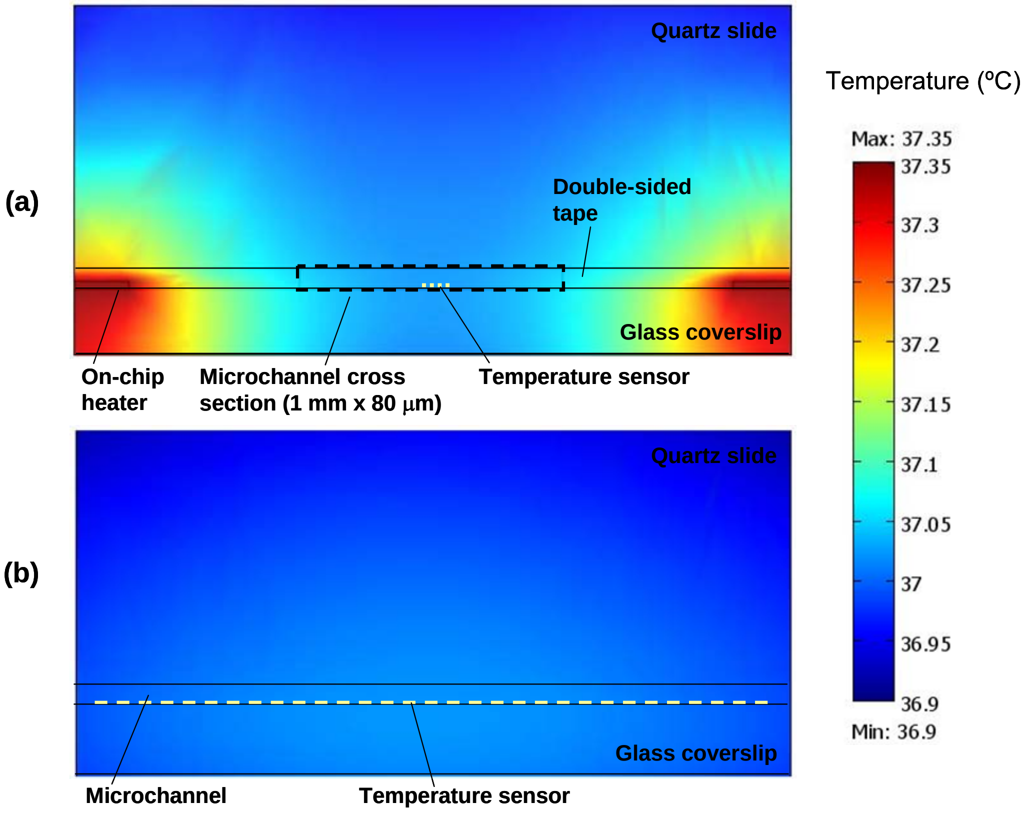

Figure 3-7: The simulated temperature distributions when the channel is heated to a setpoint temperature of 37 °C, showing temperature variations within a 1-mm section of the microchannel (corresponding to the area covered by the temperature sensor) are smaller than 0.01 and 0.03 °C, respectively, in directions (a) perpendicular to and (b) along the channel's longitudinal axis.

3.3.3 smFRET Experiments

In this section we demonstrate the utility of our microfluidic approach by investigating the temperature dependence of a smFRET signal that reports on the conformational dynamics of the ribosome and its tRNA substrates during protein synthesis, or translation. The ribosome (Figure 3-8a) is the universally conserved, two-subunit, ribonucleoprotein molecular machine that binds aminoacyl-tRNAs (aa-tRNAs) in the order dictated by the triplet-nucleotide codon sequence of a messenger RNA (mRNA) template and repetitively incorporates each amino acid into the nascent polypeptide chain until the entire mRNA template has been translated into the encoded protein product. As it incorporates each amino acid into the nascent polypeptide chain, the ribosome cycles through three fundamental steps that comprise the translation elongation cycle: (i) aa-tRNA selection and incorporation into the ribosomal aa-tRNA binding site (A site), which is catalyzed by the GTPase elongation factor Tu (EF-Tu), (ii) peptide bond formation and transfer of the nascent polypeptide from the peptidyl-tRNA bound at the ribosomal peptidyl-tRNA binding site (P site) to the newly incorporated A-site aa-tRNA, and (iii) translocation of the ribosome along the mRNA by precisely one codon, catalyzed by the GTPase elongation factor G (EF-G), during which the newly deacylated P site-bound tRNA and newly formed A site-bound peptidyl-tRNA move into the ribosomal deacylated-tRNA binding site (E site) and P site, respectively (Figure 3-8b).

The movement of tRNAs through the ribosome during translocation requires extensive remodeling of ribosome-tRNA interactions, a multistep process that involves a significant rearrangement of mobile ribosome structural elements as well as the ribosome-bound tRNAs from one structurally well-characterized global conformational state, global state 1 (GS1), to a second structurally well-characterized global conformational state, global state 2 (GS2) [6] (Figure 3-8c). Upon peptidyl transfer and in the absence of EF-G, smFRET experiments recorded at room temperature demonstrate that the pre-translocation (PRE) ribosome-tRNA complex undergoes spontaneous, thermally activated, and reversible transitions between GS1 and GS2 [6], that can be monitored using a previously characterized smFRET signal between an acceptor-labeled ribosome (labeled within the ribosomal L1 stalk) and a donor-labeled P site-bound tRNA [131] (Figure 3-8c). During each GS1→GS2 transition, the interaction between the L1 stalk and the P-site tRNA is established spontaneously as a consequence of tRNA and ribosome structural rearrangements involving a reconfiguration of the tRNA from a so-called “classical” binding configuration on the ribosome into a “hybrid” binding configuration, a “closing” of the L1 stalk into the intersubunit space, and a relative rotation of the ribosomal subunits with respect to each other (see Figure 3-8c for details on these conformational changes). During each GS2→GS1 transition, all of these structural rearrangements are reversed, resulting in a spontaneous disruption of the L1 stalk-tRNA interaction. Regulation of the GS1⇄GS2 conformational equilibrium by EF-G binding and activity promotes the directional movement of tRNAs through the ribosome during translocation and is thus a critical feature of the translocation mechanism [36, 131].

Despite its potentially important role in the mechanism of translocation, the GS1 ⇄ GS2 equilibrium has yet to be fully thermodynamically and kinetically characterized. For example, the temperature dependence of the free-energy landscape that governs the GS1⇄GS2 equilibrium remains completely unexplored. Recent temperature-dependent and time-resolved cryogenic electron microscopic (cryo-EM) reconstructions of post-translocation (POST) ribosomal complexes suggest that the free-energy landscape at the physiologically relevant temperature of 37 °C becomes completely flat, readily permitting POST complexes to sample any of a large number of conformations with roughly equal probability [138]. Since the ribosome and tRNA dynamics inferred from this cryo-EM study of POST complexes [138] involve many of the same ribosome and tRNA dynamics that comprise individual GS1→GS2 and GS2→GS1 transitions within PRE complexes (see below and Figure 3-8c) [139, 140], these cryo-EM results suggest the possibility that at the physiologically relevant temperature of 37 °C, GS1 and GS2 may not represent preferentially populated conformational states of the PRE complex (i.e. wells in the free-energy landscape) that are separated by appreciable kinetic barriers (i.e. peaks in the free-energy landscape). Thus, it remains unclear whether EF-G has to contend with the GS1 and GS2 states of PRE complex and the kinetic barriers separating them during translocation *in vivo*.

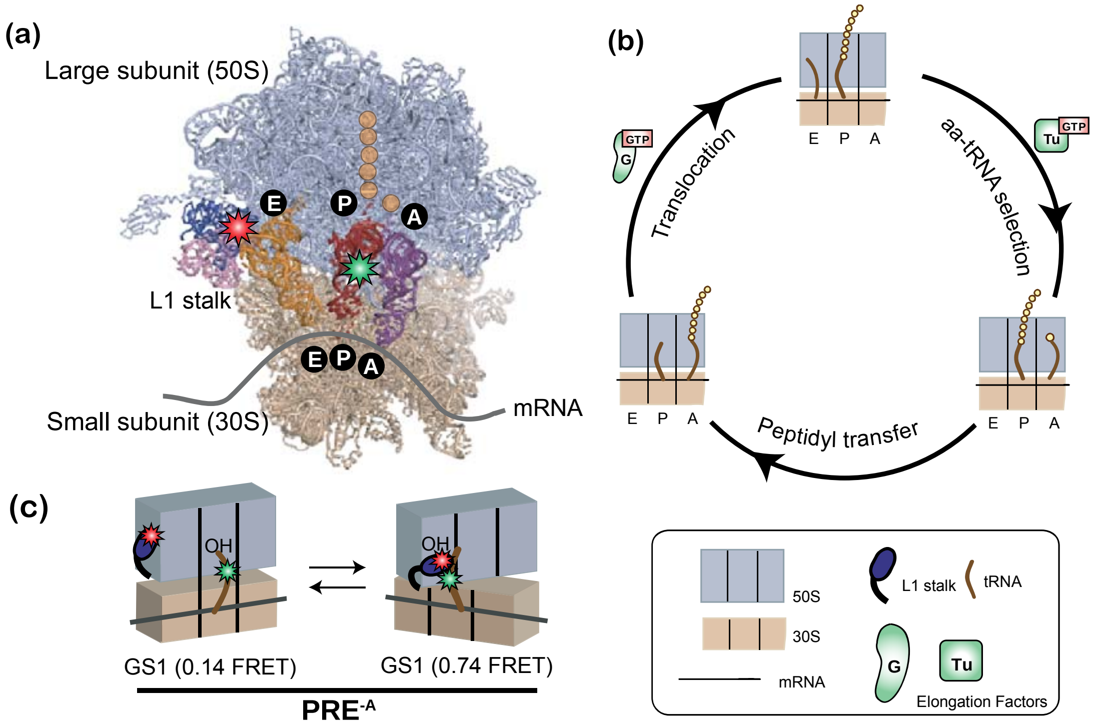

Figure 3-8: Ribosome-catalyzed protein synthesis. (a) X-ray crystallographic structure of the ribosome with its mRNA template and tRNA substrates (PDB ID: 2J00 and 2J01) and our smFRET labeling scheme. The 50S ribosomal subunit is shown in lavender and the 30S ribosomal subunit in tan. The L1 stalk consists of 23S rRNA helices 76-78 (pink) and ribosomal protein L1 (dark blue). There are three tRNA binding sites on the ribosome for aminoacyl-tRNA (A site, purple), peptidyl-tRNA (P site, red), and deacylated-tRNA (E site, orange). Individual amino acids are shown as yellow circles. Our smFRET labeling strategy places a Cy3 donor fluorophore (green star) within the central fold, or elbow, domain of the P-site tRNA and a Cy5 acceptor fluorophore (red star) within the L1 protein of the L1 stalk. (b) The three fundamental

steps of the translation elongation cycle: aa-tRNA selection, peptidyl transfer and translocation (see text for more detail). (c) The pre-translocation complex analog (PRE-A) used in our temperature-dependence studies. In the absence of EF-G the PRE-A complex fluctuates between two distinct global conformational states, GS1 and GS2.

Another example of mechanistically important information that is uniquely available from studies of the temperature dependence of the rates of GS1→GS2 and GS2→GS1 transitions are the thermodynamic activation parameters that characterize the kinetic barriers underlying GS1→GS2 and GS2→GS1 transitions. Using the GS1→GS2 and GS2→GS1 transition rates extracted from smFRET *versus* time trajectories recorded at a single temperature, the free energies of activation for GS1→GS2 and GS2→GS1 transitions have been calculated for several PRE complexes, as well as for several PRE complex analogs containing a P site-bound deacylated-tRNA but lacking an A site-bound peptidyl-tRNA ($\text{PRE}^{-\text{A}}$) [5, 141]. The lack of smFRET *versus* time trajectories recorded as a function of temperature, however, has thus far prevented determination of the relative enthalpic and entropic contributions to these free energies of activation. Measurement of the full set of thermodynamic activation parameters (i.e. activation free energy, activation enthalpy, and activation entropy) will reveal the nature of the driving forces underlying GS1→GS2 and GS2→GS1 transitions and will allow investigation of how binding of EF-G to the PRE complex modulates these forces in order to temporarily stabilize GS2 in the early steps of the translocation reaction. Access to this type of mechanistic information is afforded by studies of the temperature-dependence of GS1→GS2 and GS2→GS1 transition rates.

The $\text{PRE}^{-\text{A}}$ complex used in our temperature-dependence studies carries a deacylated tRNA^{Phe} in the P site and an empty (i.e. tRNA free) A site. Representative donor (Cy3) and acceptor (Cy5) emission intensities *versus* time trajectories recorded using this PRE^{-A} complex at temperatures of 22, 25, 28, 31, 34, and 37 °C are shown in Figure 3-9a. The corresponding smFRET *versus* time trajectories, calculated as $I_{Cy5}/(I_{Cy3}+I_{Cy5})$, where I_{Cy3} and I_{Cy5} are the Cy3 and Cy5 emission intensities, respectively, are also shown in Figure 3-9a. Consistent with previous findings [131, 142], the smFRET *versus* time trajectories fluctuate between two well-defined FRET states centred at FRET efficiencies of 0.14 ± 0.02 and 0.74 ± 0.02, corresponding to the GS1(L1 stalk-tRNA interaction is disrupted) and GS2 (L1 stalk-tRNA interaction is established) states of the PRE^{-A} complex, respectively (Figure 3-9b). The smFRET *versus* time trajectories recorded at 37 °C clearly reveal that at this temperature the PRE^{-A} complex continues to fluctuate between two well-defined FRET states centered at FRET values consistent with GS1 and GS2. This observation clearly demonstrates that at the physiologically relevant temperature of 37 °C, GS1 and GS2 continue to define minima in the free-energy landscape and that GS1→GS2 and GS2→GS1 transitions remain separated by appreciable kinetic barriers. Thus, EF-G must contend with these energetic features of the PRE complex during translocation *in vivo* and these energetic features of the PRE complex present a viable target for regulating translation *in vivo*, for example using ribosome-targeting small-molecule drugs.

Dwell-time histograms for GS1→GS2 and GS2→GS1 transitions at the various temperatures were plotted as previously described [131]. Specifically, each smFRET *versus* time trajectory was first idealized using a hidden Markov model using the HaMMy software suite [143]. We then used the idealized trajectories to plot a histogram of the idealized FRET values. The data points within the first second of each smFRET trajectories were included to avoid the accumulation of FRET value at 0 due to photobleaching of the fluorophores. The two peaks apparent in the resulting histograms were fitted with Gaussian distributions using user-specified initial values of 0.1 and 0.7 (Figure 3-9b), corresponding to the approximate FRET values of GS1 and GS2, respectively. The center and the full width at half height of the resulting Gaussian distributions were used to determine the thresholds for each FRET state. Using these thresholds to define the GS1 and GS2 states in the idealized trajectories, transition events were identified and dwell time spent in GS1 or GS2 before transitioning into GS2 or GS1 were extract, respectively. Population histograms of the dwell times spent in GS1 or GS2 were then plotted as a function of the dwell time [131] (Figure 3-9c and d).

Comparison of the smFRET *versus* time trajectories recorded across all measured temperatures clearly demonstrates that the frequencies of both GS1→GS2 and GS2→GS1 transitions increase as a function of increasing temperature (Figure 3-9a). Consistent with this observation, histograms of the dwell times spent at GS1 prior to undergoing a GS1→GS2 transition (Figure 3-9c) or at GS2 prior to undergoing a GS2→GS1 transition (Figure 3-9d) plotted at the various temperatures reveal that both GS1 and GS2 are destabilized by increasing temperature. Extension of these experiments to PRE^{-A} complexes in the absence *versus* the presence of EF-G, containing different P site-bound tRNAs, using multiple smFRET labeling schemes, and/or recorded under a variety of buffer conditions should now allow a comprehensive analysis of the thermodynamic activation parameters associated with GS1→GS2 and GS2→GS1 transitions.

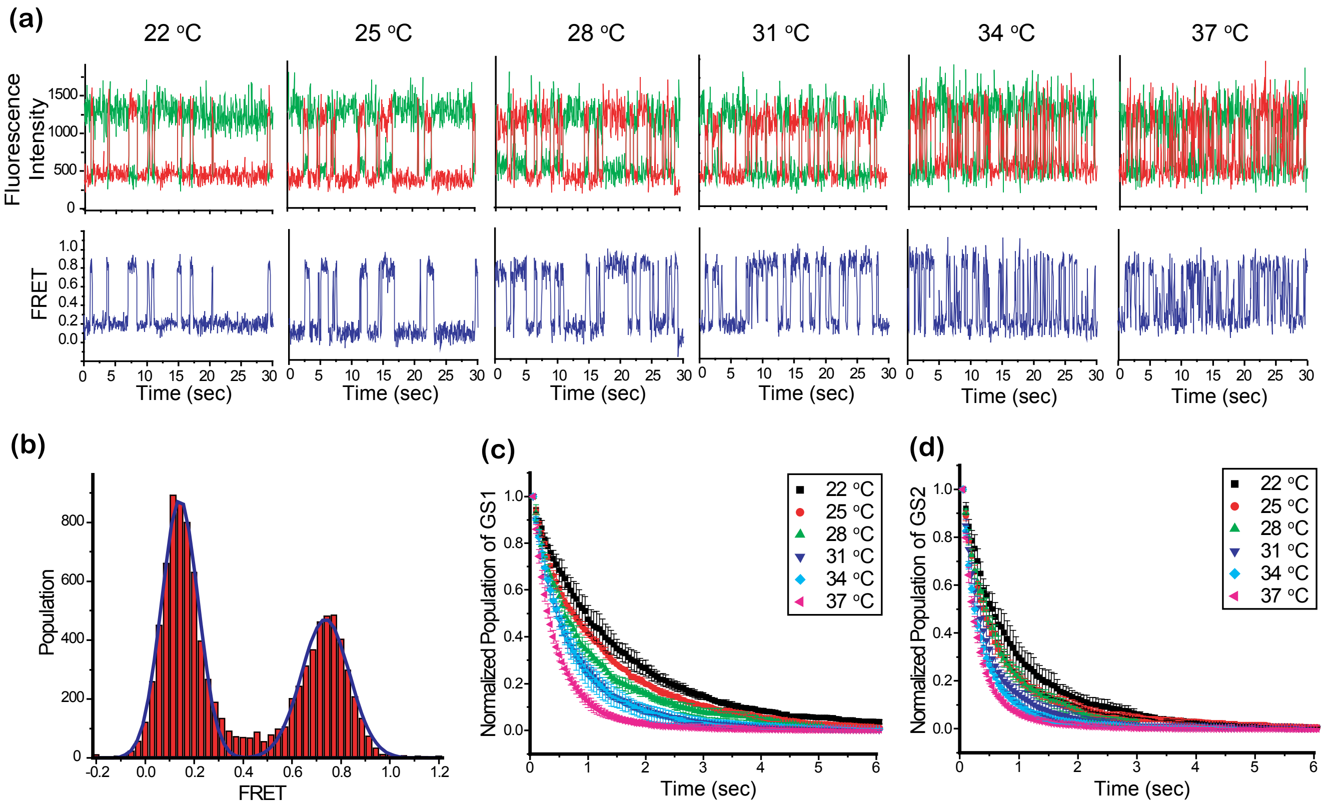

Figure 3-9: Temperature-dependent investigation of the GS1 $\rightleftarrows$ GS2 equilibrium obtained using our microfluidic platform in combination with TIRF microscope-based smFRET measurements at controlled temperatures of 22, 25, 28, 31, 34, and 37 °C. (a) Representative Cy3 and Cy5 emission intensities and FRET *versus* time trajectories. Cy3 and Cy5 emission intensities *versus* time trajectories are shown in green and red, respectively (top row). The corresponding smFRET *versus* time trajectories are shown in blue (bottom row). (b) Histogram of idealized FRET values built using the data collected at the 22˚C temperature point as an example. Dwell time histograms of (c) GS1 prior to undergoing a GS1→GS2 transition and (d) GS2 prior to undergoing a GS2→GS1 transition at the various temperature points that were investigated.

3.4 Conclusions

This chapter presents a microfluidic approach to investigating the temperature-dependence of single-molecule activity. Our approach utilizes a temperature-controlled microfluidic flowcell coupled to a prism-based TIRF microscope. The temperature-controlled microfluidic flowcell consists of a set of parallel microchannels formed between a quartz slide and a glass coverslip on which thin-film micro-heaters, for efficient and rapid on-chip heating, and temperature sensors, for *in situ* temperature measurements within the microchannels, are integrated. Closed-loop, accurate temperature control is accomplished by a PID algorithm with the steady-state temperature maintained within approximately ±0.01 °C of the desired setpoints while achieving thermal stability within less than 30 s.

The utility of our microfluidic approach has been demonstrated by its application to the characterization of the temperature dependence of smFRET *versus* time trajectories reporting on the $GS1 \rightleftarrows GS2$ equilibrium within a PRE^{-A} ribosomal complex. Analysis of the smFRET *versus* time trajectories recorded as a function of temperature reveal that the GS1 and GS2 states of PRE complexes represent configurations of the PRE complex that are preferentially populated at the physiologically relevant temperature of 37 °C and that EF-G must contend with the kinetic barriers that govern GS1→GS2 and GS2→GS1 transitions during translocation *in vivo*. In addition, analysis of the histograms of the dwell times spent in the GS1 or GS2 states prior to undergoing a transition plotted from the smFRET *versus* time trajectories recorded the various temperatures reveal that the frequencies of both GS1→GS2 and GS2→GS1 transitions increase as a function of increasing temperature and that these effects are driven by corresponding decreases in the stabilities of the GS1 and GS2 states of the PRE^{-A} complex, respectively. These results provide a valuable starting point for the comprehensive analysis of the thermodynamic activation parameters underlying the GS1→GS2 and GS2→GS1 transitions of PRE complexes, as well as the effect of EF-G on these parameters during translocation.

Chapter 4 A MEMS Differential Scanning Calorimetric Sensor for Thermodynamic Characterization of Biomolecules

This chapter presents a MEMS sensor for differential scanning calorimetry (DSC) of liquid-phase biomolecular samples. The device consists of two microchambers, each of which is based on a freestanding polyimide diaphragm and surrounded by air cavities for thermal isolation. The chambers are each equipped with a thin-film gold resistive heater and temperature sensor, and are also integrated with a thin-film antimony-bismuth (Sb-Bi) thermopile. For DSC measurements, the chambers are respectively filled with a biomolecular sample and a reference solution, with their temperature varied at a constant rate. The thermopile voltage is measured to determine the differential power between the chambers for thermodynamic characterization of the biomolecules. The device is used to measure the unfolding of proteins in a small volume (1 μL) and at practically relevant concentrations (approximately 1 mg/mL). Thermodynamic properties, including the enthalpy change and melting temperature, during this conformational transition are determined and found to agree with published data.

4.1 Background

DSC directly measures heat evolved in thermally active processes as the temperature of a sample is varied. When applied to biochemical systems, DSC provides a label-free method (i.e., the detection is achieved without fluorescent, enzymatic or radioactive labeling of the biomolecules) to determine the thermodynamic properties of a wide variety of biomolecular interactions and conformational transitions [51-53].

Conventional DSC instruments, however, involve cumbersome designs, are inconvenient to operate, and require large sample sizes (~1 mL) [51, 52]. These issues have hindered the widespread application of DSC to biomolecular characterization. In a recently developed scanning calorimetry method [144], liquid sample and reference solutions were contained in capillary tubing integrated with thin-film temperature sensing, although a relatively large sample volume and high sample concentration was still required. These issues can potentially be addressed by miniaturization via Microelectromechanical Systems (MEMS) technology, as MEMS-based calorimetric devices can have unique advantages over conventional instruments, including reduced sample consumption, rapid time response, and improved throughput [145].

MEMS calorimetric devices, however, remain scarce while the existing examples are generally limited by several critical issues. One issue is in the inability to properly handle liquid samples in a well-defined environment [92, 95, 99, 101-103]. In addition, the calibration of MEMS DSC devices can greatly benefit from the proper use of integrated power generation and temperature sensing [144], such that cumbersome auxiliary equipment such as external optical equipment [102, 146]. While thin-film resistive heaters and temperature sensors were included in our previous MEMS DSC device [147], limitations in the heater geometry and placement did not allow on-chip heating to be used for device calibration.

In this chapter, we present a MEMS DSC sensor aiming to address these critical issues. The device integrates two microfluidic calorimetric chambers containing liquid-phase sample and reference solutions, each of which is based on a freestanding, thermally stable polyimide diaphragm and surrounded by air cavities for effective thermal isolation.

A Sb-Bi thermopile is embedded in the diaphragm for sensitive thermoelectric detection, and resistive microheaters and temperature sensors are properly aligned to calorimetric chambers for on-chip device calibration. The device is applied to the measurement of the unfolding of proteins in small volume (1 μL) at practically relevant concentrations (approaching 1 mg/mL), demonstrating the potential of MEMS calorimetry to enable sensitive biomolecular characterization with minimized sample consumption.

4.2 Materials and Methods

4.2.1 Principle and Design

DSC measures the differential thermal power, i.e., the difference in thermal power between a sample and a reference material, as a function of temperature. When the sample and reference materials are subjected to identical temperature scanning, i.e., their temperatures are varied at a prespecified rate within a range of interest, the thermally induced activity of the sample molecules, which is either exothermic or endothermic, causes a small temperature difference between the sample and reference materials (i.e., differential temperature). This differential temperature can be detected to reflect the differential power

$$\Delta P = P_{\mathrm{s}} - P_{\mathrm{r}} \tag{4-1}$$

where P_{s} and P_{r} are the thermal power generated in the sample and reference materials, respectively [147]. Therefore the differential heat capacity

$$\Delta C_{\mathrm{p}} = C_{\mathrm{ps}} - C_{\mathrm{pr}} \tag{4-2}$$

where C_{ps} and C_{pr} are, respectively, the heat capacities of the sample and reference materials, can be determined as [147]

$$\Delta C_{\mathrm{p}} = \frac{\Delta P}{\dot{T}} = \frac{\Delta U}{S\dot{T}} \tag{4-3}$$

where $\dot{T}$ is the time rate of the controlled temperature of sample and reference materials, ΔU is the output from the thermoelectric sensor that is employed to detect the differential temperature [148], and S is the thermoelectric sensitivity, i.e., the output electrical voltage generated by unit differential thermal power. Interpretation of the differential heat capacity then leads to determination of the fundamental thermodynamic properties of the sample material [147].

The MEMS DSC device consists of two identical PDMS microchambers, which hold sample and reference materials for calorimetric measurements. These chambers, referred to as the sample and reference chambers, respectively, are each connected to inlet and outlet ports by microfluidic channels and situated on a freestanding polyimide diaphragm. The diaphragms, along with air cavities surrounding the chambers, provide thermal isolation that enables sensitive calorimetric measurements (Figure 4-1a). The device is composed of multiple material layers (Figure 4-1b), including a layer of thin-film Sb-Bi thermopile embedded in the diaphragms with its hot and cold junctions located underneath the centers of the calorimetric chambers to measure the temperature difference between the sample and reference solutions. Each calorimetric chamber is also integrated with a thin-film resistive micro-temperature sensor and heater, in a separate material layer underneath the chamber center. These thermal transducers monitor the chamber temperatures in real time, and provide heating to the calorimetric chambers to generate a constant differential power for calorimetric calibration.

Antimony (Seebeck coefficient: 43 μV/K) and bismuth (Seebeck coefficient: -79 μV/K) [148] are chosen for differential temperature sensing due to their high thermoelectric sensitivies and ease of fabrication. Polymers are used to construct the calorimetric chambers to facilitate thermal isolation. In particular, polyimide is chosen as the diaphragm material due to its excellent mechanical stiffness (Young's modulus: 2.5 GPa) and thermal stability (glass transition temperature: 285 °C) [149], while PDMS is used to fabricate the calorimetric chambers for its ease of fabrication and packaging as well as biocompatibility.

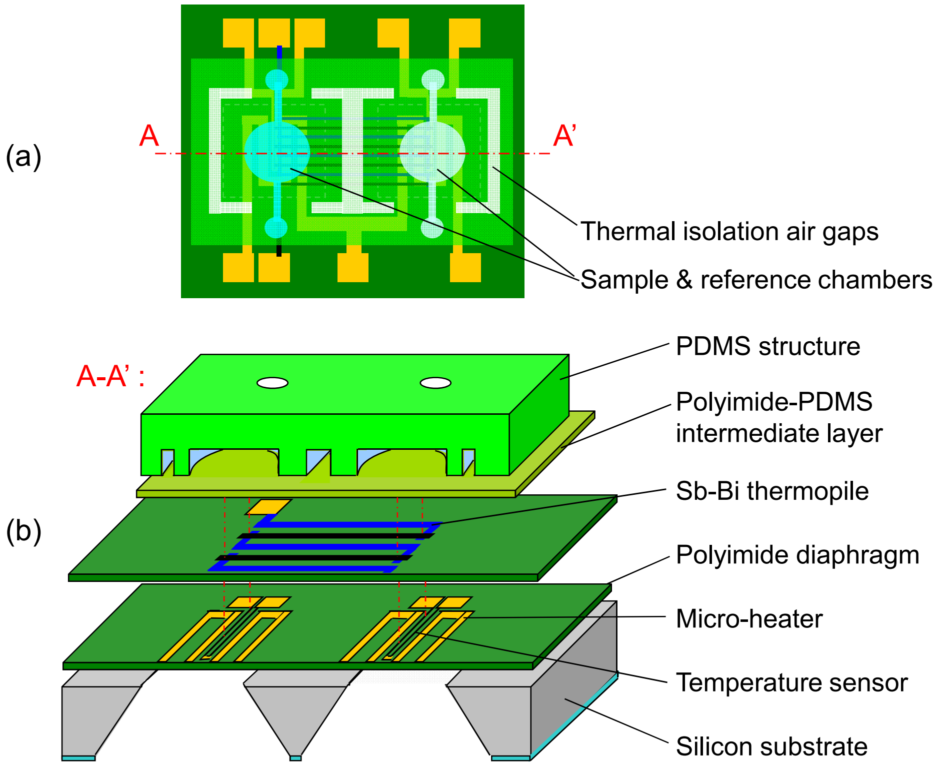

Figure 4-1: Schematic of the MEMS DSC device: (a) top, and (b) isometric views.

4.2.2 Fabrication and Measurements Setup

The fabrication of the MEMS DSC device involved a thermal substrate bonded to a microfluidic structure. The thermal substrate was fabricated from a silicon wafer that was precoated with silicon dioxide, starting with deposition of a 6-µm thick polyimide film by spin-coating. A pair of cavities were etched by tetramethylammonium hydroxide

(TMAH) into the backside of the wafer in correspondence to the calorimetric chambers, down to an approximately 50 μm-thick residual layer left on the front side (Figure 4-2a). After fully curing the polyimide film, a chromium/gold thin film (5/200 nm) was deposited by thermal evaporation to obtain the microheaters and temperature sensors, where then passivated with another polyimide layer (2 μm) by spin-coating (Figure 4-2b). Subsequently, Sb and Bi thin films (0.5 and 1.2 μm) were thermally evaporated and patterned using a standard lift-off process to form a 50-junction thermopile (Figure 4-2c). The microfluidic structure was fabricated from PDMS using micromolding techniques [150], and comprised the calorimetric chambers each of cylindrical shape and 1 μL in volume (diameter: 2.5 mm and height: 200 μm), with a center-to-center separation of 4 mm. Also included in the microfluidic structure were the microchannels (length: 2 mm, width: 100 μm, and height: 200 μm) connecting the chambers to the inlet and outlet ports. The thermal substrate was bonded with the PDMS microfluidic structure, with adhesion provided by an intermediate layer of polyimide-PDMS mixture [151] (approximately 2 μm thick) (Figure 4-2d). Finally, XeF_2 gas-phase isotropic etching was used to remove the residual silicon layer on the thermal substrate, releasing the freestanding polyimide diaphragm (Figure 4-2e). The integrated resistive microheaters each had a nominal resistance of 40 Ω and the temperature sensors each had a nominal resistance of 55 Ω. Shown in Figure 4-3 are the images of the PDMS structure and thermal substrate, as well as micrographs of the thermopile, integrated microheater and temperature sensor embedded in the diaphragm.

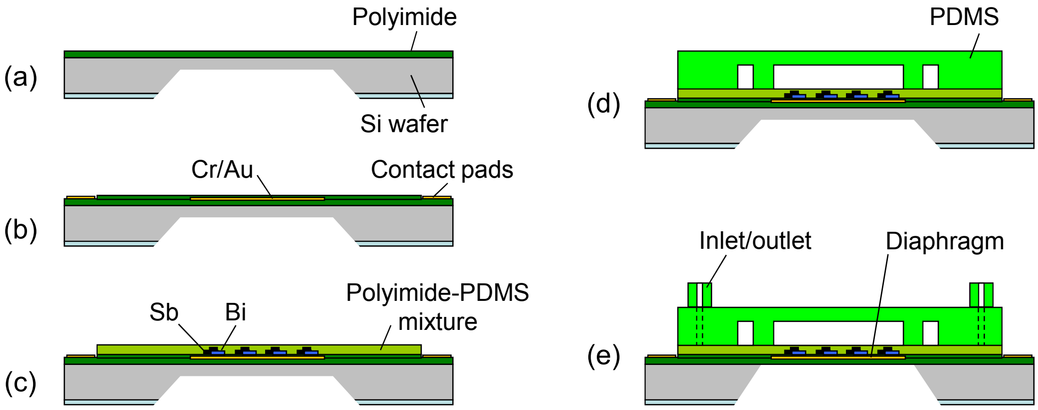

Figure 4-2: Fabrication process for the MEMS DSC device.

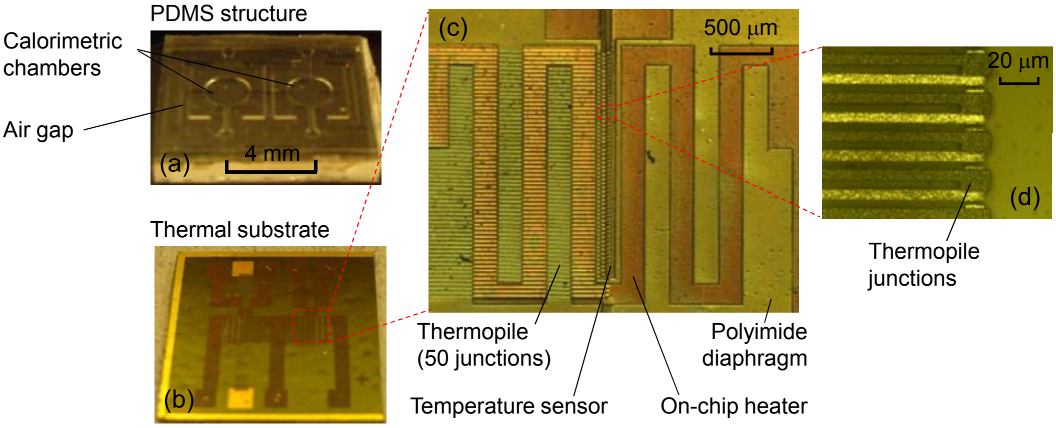

Figure 4-3: Images of a MEMS device: (a) the PDMS microfluidic structure, (b) the thermal substrate, (c) the thermopile, integrated microheater and temperature sensor embedded in the diaphragm, and (d) the thermopile junctions.

The experimental setup is illustrated in Figure 4-4. The on-chip microheaters, used for device calibration, were driven by a DC power supply (Agilent E3631A) and generated a constant differential heating power in the calorimetric chambers. The on-chip temperature sensors, used for both device calibration and DSC measurements of biomolecules, were interrogated by a digital multimeter (Agilent 34410A) to monitor the temperatures of the calorimetric chambers (Figure 4-4a). The thermopile output voltage, which is proportional to the differential temperature between the chambers, was measured by a nanovoltmeter (Agilent 34420A). The temperature control of the MEMS DSC device and thermoelectric measurements were automated using a personal computer via a LabVIEW-based program.

A packaged MEMS DSC device (i.e., a device made accessible to the macroworld by electrical interconnection wires and fluid interconnection tubes) was housed in a custom-built, temperature-controlled thermal enclosure consisting of multiple metal enclosure layers surrounding a metal stage on which the device was placed (Figure 4-4b). Multiple Peltier devices (Melcor UT15-12-40-F2) were located underneath the device stage, and by a power supply (Agilent E3631A), to add heat to or remove heat from the device. The temperature of the sample and reference chambers was controlled in closed loop by adjusting the voltage applied to the Peltier devices according to the feedback from the on-chip temperature sensors based on a PID algorithm.

The thermal enclosure offered thermal isolation of the device from the ambient environment to minimize measurement noise [152, 153]. In addition, the enclosure provided an environment in which the sample and reference solutions in the device were at a sufficiently uniform temperature, which was scanned at a specified rate. At any instant during DSC measurements, this allowed the biomolecules in the sample solution to experience a uniform temperature, which was accurately obtained by the on-chip temperature sensors. Thus, together with determination of the differential power by the thermopile, the MEMS device in this experimental setup could achieve accurate DSC measurements of biomolecules.

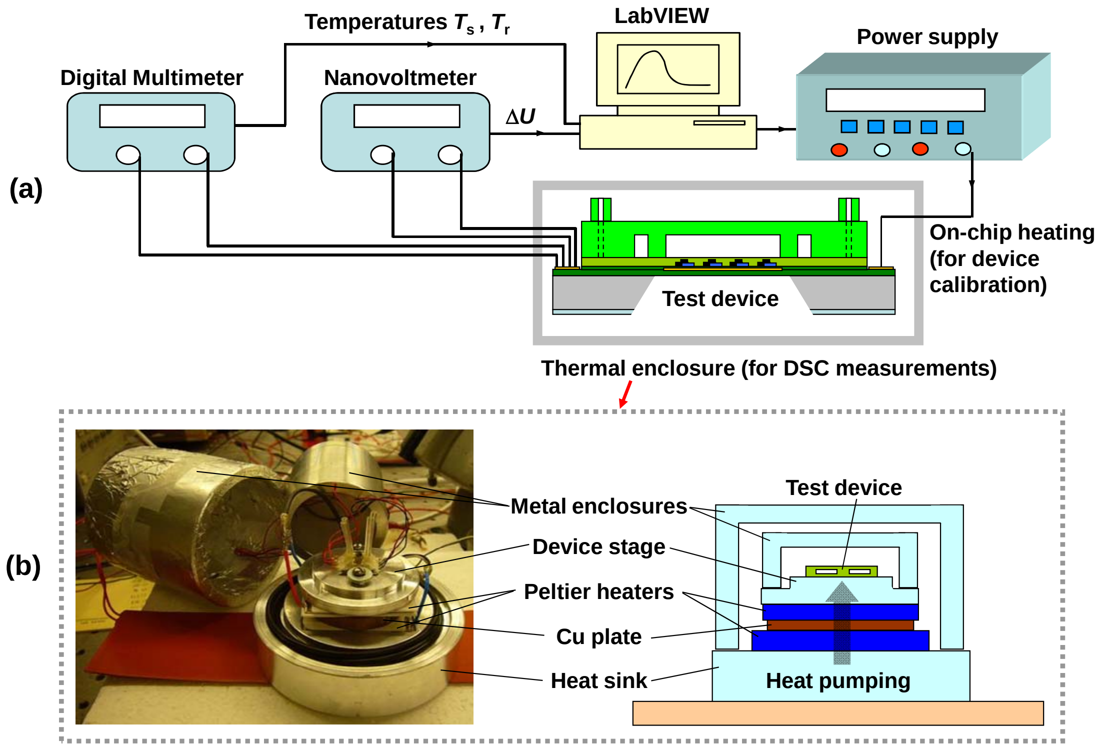

Figure 4-4: Testing setup for the MEMS DSC device. (a) DSC measurement setup. (b) Details of the custom-built, temperature-controlled thermal enclosure.

4.2.3 Experimental Method

The device was calibrated to determine the device response as a function of the differential power. This involved measurement of the output voltage of the thermopile in response to a known differential power, applied using the microheaters integrated on-chip, between the sample and reference chambers, which were both filled with pure buffer containing no biomolecules. Note that while DSC measurements generally require biomolecules at a uniform temperature (as described above), temperature uniformity was not a major requirement for the device calibration because of the absence of biomolecules in the chambers. Thus, it was sufficient for the applied differential power to be given in the form of the difference in total thermal power between the chambers, and this was adequately accomplished by on-chip heating despite its potential temperature localization effects.

During device calibration, the sample and reference chambers were both filled with 0.1 M Glycine-HCl buffer (pH 2.5), which was the buffer later used for protein unfolding measurements. A known, constant differential power was created by activating the microheater below the sample chamber while leaving the microheater underneath the reference chamber turned off. The temperature sensors were used to measure the temperatures of the thermopile's hot and cold junctions. The device output, i.e., the thermopile output voltage, was measured as a function of time to obtain the device's steady-state and transient responses to the differential heating power.

Before DSC measurements, the baseline in device output, i.e., the thermopile output voltage in the absence of a differential power input, during temperature scanning was measured with both calorimetric chambers filled with buffer solutions. Biological sample and buffer solutions were degassed with a vacuum chamber built in-house, metered with micropipettes, and introduced by a syringe pump (New Era Pump Systems, NE 1000). DSC measurements of biomolecules were performed with the temperature of the calorimetric chambers, respectively filled with biological sample and buffer solutions, scanned in a range of interest. The temperature sensors were used to monitor the temperatures of calorimetric chambers while the device output was obtained in real time to compute the biomolecular thermal power. The baseline in device output was always subtracted from the measurement signal for determination of thermodynamic properties of biomolecules.

4.3 Results and Discussions

4.3.1 Device Calibration

We first calibrated the sensitivity of the thermopile integrated in the MEMS DSC device at varying temperature difference between the hot and cold junctions, generated by on-chip heating. The thermopile differential voltage exhibited a highly linear relationship with temperature difference (Figure 4-5), showing a total thermoelectric sensitivity of 6.3 mV/ºC for the 50-junction thermopile. Therefore, a Seebeck coefficient of 125 μV/K for each Sb-Bi thermocouple was obtained, which was well within the range of values in the literature [154].

In addition, we calibrated the steady-state response of the MEMS DSC device to varying differential power and observed again a highly linear relationship, yielding a nearly constant responsivity of $S = 4.0$ mV/mW (Figure 4-6). This is approximately four times the responsivity of our previous MEMS DSC device [147] due to the higher thermoelectric sensitivity of the Sb-Bi thermopile. We have measured the device's steady-state response to differential power at different temperatures ranging from 25 to 65 °C (controlled by the thermal enclosure). The measurement data indicated that the device responsivity in this temperature range exhibited a relative standard deviation of less than 4%. It is thus acceptable to neglect the temperature dependence of the device sensitivity. We also observed a root-mean-square (RMS) noise of approximately 40 nV in the device output, which was used to determine a baseline noise in the differential power. This corresponded to a detection limit of approximately 10 nW in differential thermal power measurement, or a 3× improvement over that allowed by our previous MEMS DSC device [147].

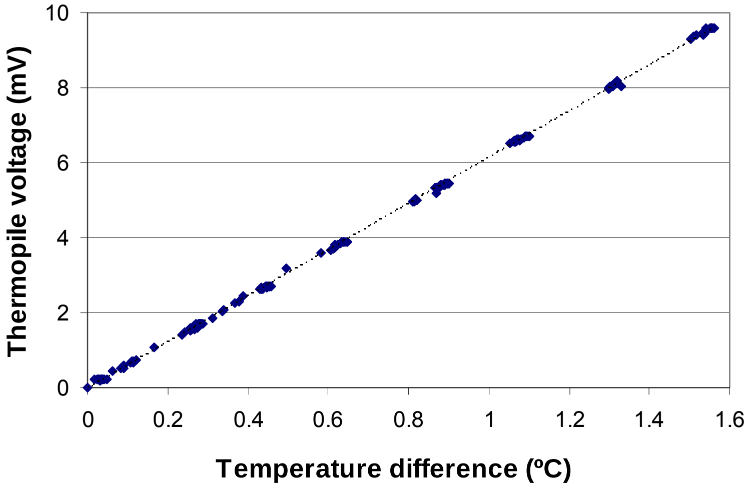

Figure 4-5: Thermopile output voltage from the MEMS DSC device in response to constant temperature difference between the thermopile's hot and cold junctions.

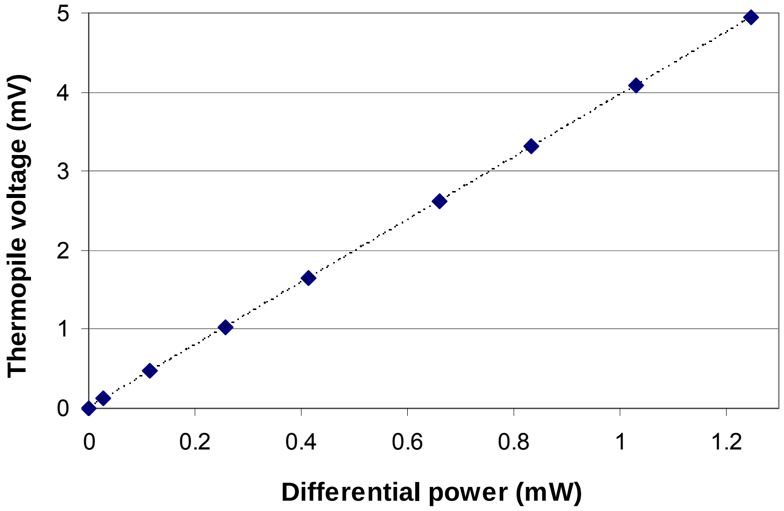

Figure 4-6: Steady-state response of the MEMS DSC device to constant differential power between the calorimetric chambers.

To characterize the transient response of the MEMS DSC device, a step differential power of 130 μW was initially applied to the calorimetric chambers and then turned off once the device output reached its equilibrium. The corresponding output voltage from the thermopile (Figure 4-7) was found to exponentially grow with time upon the application of the differential power, while decay exponentially upon the removal of the differential power. The thermal time constant was approximately 2.0 s, calculated by fitting the experimental data to first-order exponential growth and decay functions. This is significantly smaller than time constants of conventional DSC instruments [59] and considered appropriate for detection of biomolecular conformational transitions.

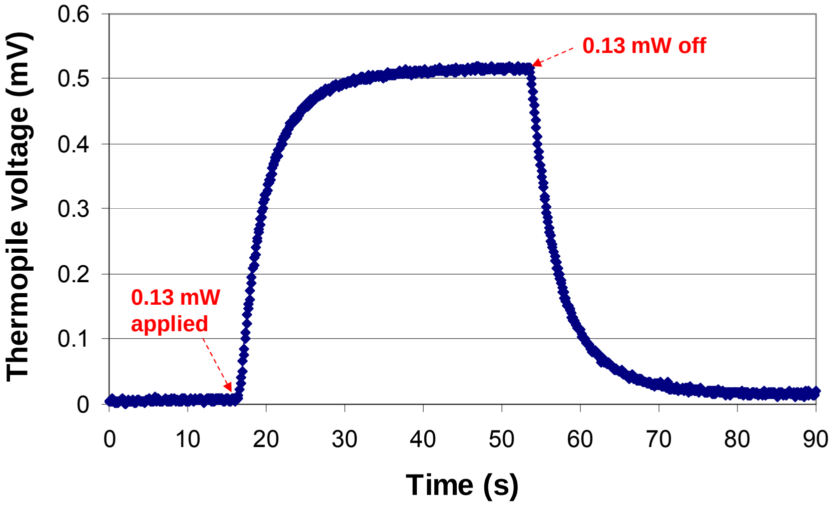

Figure 4-7: Transient response of the MEMS DSC device with respect to a step differential power.

4.3.2 Measurements of Protein Unfolding

The calibrated MEMS DSC device was exploited to characterize protein unfolding, a common type of biomolecular conformational transition. For this purpose, the thermal enclosure was found to be capable of providing temperature scanning of the MEMS DSC device at time rates as high as 6 ºC/min in the range of 10-90 ºC with power consumption lower than 25 W. Using lysozyme prepared in 0.1 M Glycine-HCl buffer (pH 2.5) for demonstration purposes, we monitored the device output while the sample and reference chambers, respectively filled with lysozyme and buffer, were scanned in a temperature range of 25-75 ºC at a constant rate of 5 ºC/min.

The thermopile output voltage as a function of temperature, corrected by baseline subtraction, was measured at varying protein concentrations ranging from 1 to 20 mg/mL (0.07-1.4 mM) (Figure 4-8). It can be observed that the device output exhibited a concentration-dependent minimum within a certain temperature range, reflecting the endothermic nature of protein unfolding processes. Notably, the unfolding of lysozyme was detectable at 1 mg/mL, representing a significant improvement over the MEMS DSC device we previously reported [147].

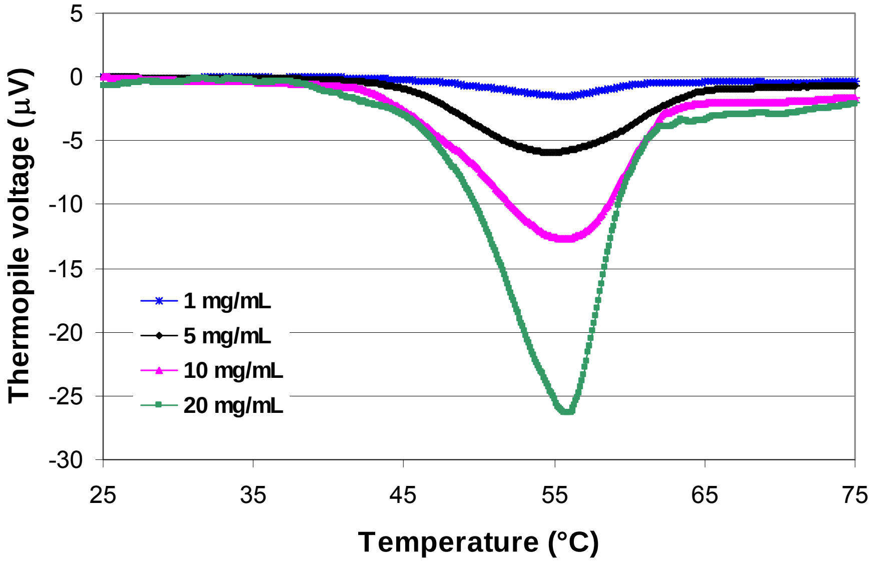

Figure 4-8: Output (baseline subtracted) of the MEMS DSC device as a function of temperature during the unfolding of lysozyme at varying concentrations.

4.3.3 Determination of Thermodynamic Properties

Furthermore, the differential heat capacity between the chambers was computed from the differential voltage measurement (Figure 4-8) using calibrated device sensitivity

(4.0 mV/mW) and Eq. (4-3), allowing us to obtain the thermodynamic properties of lysozyme during its unfolding process, such as partial specific heat capacity (c) (Figure 4-9a), the total change of molar enthalpy (i.e., enthalpy per mole of lysozyme) (ΔH), and melting temperature (T_m, defined as the temperature at which the change of molar enthalpy achieves 50% of ΔH) (Figure 4-9b) using a model previously described [147]. Despite the amplitude difference of device output at various protein concentrations, they all yielded consistent estimates of the thermodynamic properties associated with the protein unfolding process. In particular, the profile shape of c was generally not influenced by protein concentration, and ΔH was consistently determined to be approximately 450 kJ/mol with a corresponding melting temperature T_m of approximately 55 ºC. These results agree with published data, which are typically in the range ΔH = 377-439 kJ/mol and T_m = 55-58.9 ºC for lysozyme [155], demonstrating the potential utility of our MEMS DSC device for biomolecular characterization with minimal sample consumption at practically relevant protein concentrations.

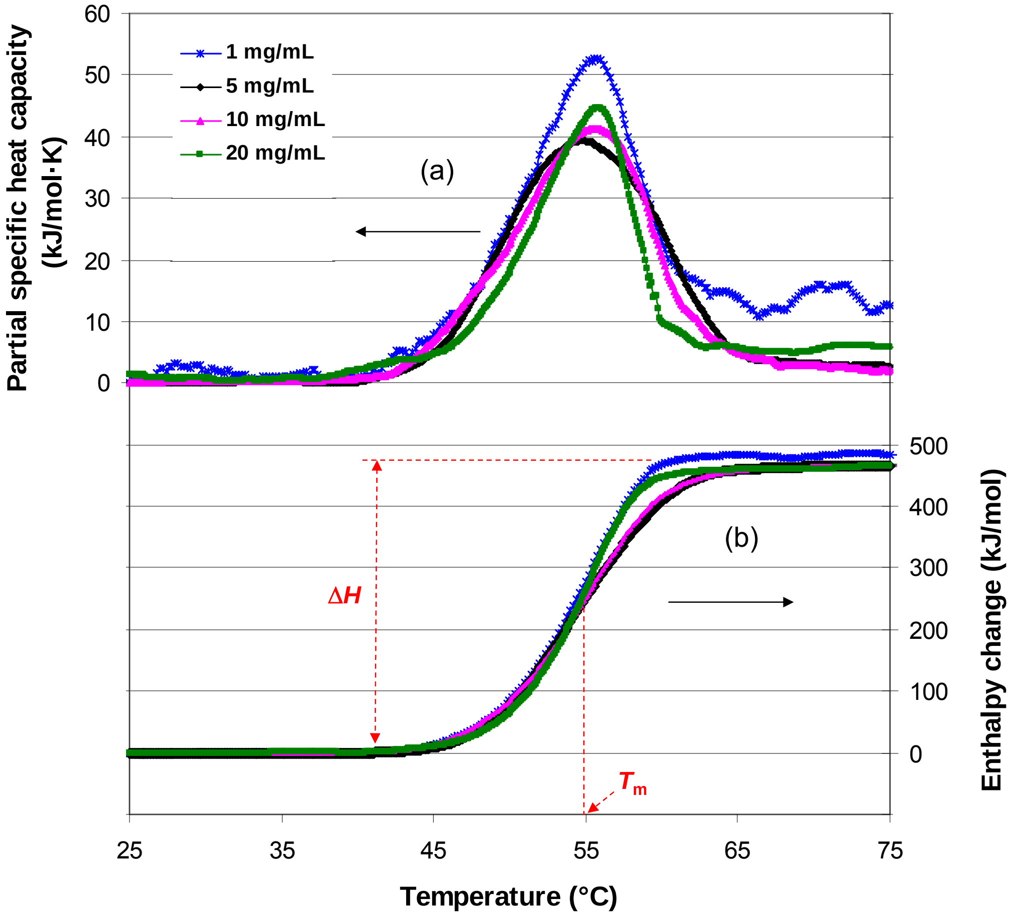

Figure 4-9: (a) Partial specific heat capacity, and (b) change of molar enthalpy as a function of temperature, during the unfolding of lysozyme at varying concentrations.

4.3.4 Effect of Temperature Scanning Rate

We further investigated the effects of the temperature scanning rate on DSC measurements [156], considering that temperature scanning unsynchronized with the thermal response of the sample could cause error in measurements [157]. Using 20 mg/mL lysozyme prepared in 0.1 M Glycine-HCl buffer (pH 2.5) for example, we characterized its unfolding at temperature scanning rates varying from 1-6 ºC/min. The thermopile output voltage (again corrected by baseline subtraction) (Figure 4-10a) exhibited a consistent dip in the same temperature range for protein unfolding as indicated above, with an amplitude increasing with the temperature scanning rate. This is consistent with a larger heat flux resulting in a higher endothermic power through phase transformations [158, 159].

These data were then used to compute the change of molar enthalpy (Figure 4-10b), also using the method described in Ref. [147]. Although a slight shift in the device output could be observed (Figure 4-10a) as temperature scanning rate increased, the thermodynamic properties associated with the protein unfolding process were found generally consistent, with a standard variation in ΔH of approximately 50 kJ/mol (i.e., ± 5% of the mean value of ΔH) and a standard variation in T_m of less than 1 ºC (Figure 4-10b). Notably, for temperature scanning at 1-5 ºC/min, the T_m values were almost the same. This demonstrates the measurement consistency using our MEMS DSC device, and indicates that a temperature scanning rate as high as 5 ºC/min is adequate for the measurement of lysozyme unfolding.

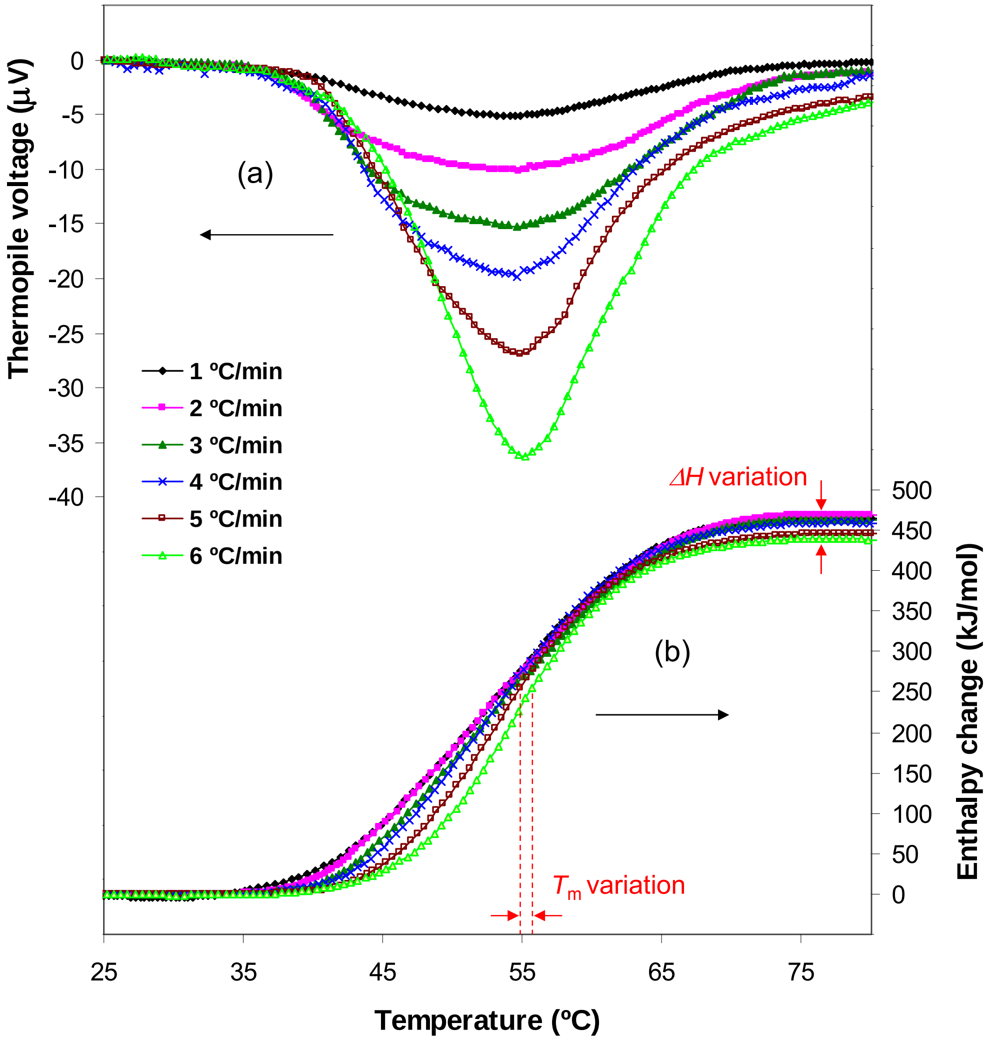

Figure 4-10: (a) Output of the MEMS DSC device, and (b) change of molar enthalpy as a function of temperature, during the unfolding of lysozyme (20 mg/mL) at varying temperature scanning rates.

4.4 Conclusions

This chapter presents a MEMS DSC sensor combining sensitive thermoelectric sensing and effective thermal isolation for thermodynamic characterization of small quantities of liquid-phase biomolecular samples. The device consists of a pair of PDMS microfluidic chambers (volume: 1 μL), each situated on a freestanding polyimide diaphragm and surrounded by air cavities for thermal isolation. The calorimetric chambers are each integrated with a thin-film resistive gold temperature sensor and heater for temperature monitoring and on-chip calibration heating. The chambers are also integrated with a thin-film Sb-Bi thermopile whose hot and cold junctions are located at the centers of the chambers to measure the differential temperature between chambers. The device is placed within a custom-built thermal enclosure, which provide uniform temperature scanning and minimized environmental disturbances. For DSC measurements, the calorimetric chambers are respectively filled with a biomolecular sample and a reference solution. With their temperature scanned at a constant rate over a range of interest, the differential thermal power between the biomolecular sample and reference solution is measured via the thermopile voltage in real time and used to compute the thermodynamic properties of the biomolecules, including the partial specific heat capacity, the change of molar enthalpy, and the melting temperature.

The MEMS DSC sensor was first calibrated to determine its responsivity (4 mV/mW) and thermal time constant (2.0 s). It was then used to measure the unfolding of lysozyme at detectable sample concentrations approaching 1 mg/mL. Using the measurement data, the total change of molar enthalpy and melting temperature in the lysozyme unfolding process were determined to be approximately 450 kJ/mol and 55 ºC, in agreement with values (377-439 kJ/mol and 55-58.9 ºC) reported in the literature. Finally, we investigated the effects of choice of temperature scanning rate on DSC measurements using the device and observed that a temperature scanning rate as high as 5 ºC/min is adequate for the characterization of lysozyme unfolding. These results demonstrate the potential of this MEMS DSC device for sensitive biomolecular characterization with minimized sample consumption.

Chapter 5 Temperature-Modulated Differential Scanning Calorimetry in a MEMS Device

This chapter presents a MEMS-based approach to temperature-modulated differential scanning calorimetry (AC-DSC) for biomolecular characterization. Based on a MEMS device integrating microfluidic handling with highly sensitive thermoelectric detection as well as on-chip AC heating and temperature sensing, we perform, for the first time, MEMS-based AC-DSC detection of liquid biological samples, demonstrated by the measurements of protein unfolding. The specific heat capacity and the melting temperature of the protein during the unfolding process are obtained and found to be consistent with published data. This MEMS AC-DSC approach has potential applications to label-free characterization of biomolecules.

5.1 Background

DSC is a widely applicable label-free characterization method for solution-phase biomolecular interactions [51]. Standard DSC (i.e., DC-DSC), in which the temperature of the materials is varied at a constant rate, is one of the most widely applicable calorimetric measurement modes. DC-DSC methods have been used to characterize a wide variety of biomolecular interactions and conformational transitions [52].

Temperature-modulated differential scanning calorimetry (AC-DSC) is a variant of DSC. In comparison to DC-DSC, AC-DSC involves calorimetric measurements under temporally periodic temperature variations. The use of temperature modulation allows more effective thermal relaxation of biomolecules, and hence AC-DSC is in general capable of higher temperature scanning rates than offered by DC-DSC [160]. In addition, by choice of the modulation frequency, the heat leakage from the biochemical reactants to the surroundings, which exists in non-adiabatic calorimetric measurements, can be reduced [161, 162] to minimize a significant source of experimental error. Moreover, AC calorimetry minimizes the effects of broad-band background noise via extraction of the detection signal by referencing the modulation frequency [163].

However, for conventional calorimetric instruments, the large thermal mass of the machine and the relatively large sample volumes used dictates a relatively slow thermal time response, making it difficult to exploit the more rapid temperature scanning rates AC-DSC could offer. MEMS technology can potentially address this issue by minimizing device dimensions, resulting in smaller thermal masses and minimized sample consumption. MEMS-based calorimetric devices, however, have not yet been extensively explored for biomolecular characterization [164]. The length scale reduction offered by MEMS technology [165] and hybrid designs combining external flowcells [103] have enabled high-throughput measurements of biomolecular binding. Cell metabolism was measured using differential calorimetric detection in an open environment [102], and we have previously demonstrated MEMS DSC characterization of protein denaturation with miniature thermal transducers and microfluidic chambers [147].

Recently there have been attempts to combine MEMS designs with the AC-DSC approach using microchips for AC calorimetric studies. Samples were measured in microdevices integrating thermoelectric sensing and AC heating. The AC heat was generated by different methods, such as using thermocouples as both the heating source and the thermal sensor [166], directly applying an AC current through the sample materials [167], and using a modulated Peltier module as the heat bath [162]. However, these devices are generally focused on studying the material properties of solid thin films under extreme experimental conditions (e.g., very low temperature) [168] in an open environment [169], and are hence not well suited to solution-based biomolecular characterization.

This chapter presents experimental results from AC-DSC of liquid biological samples within a MEMS device. The device, which was recently developed for DC-DSC measurements without temperature modulation [170], consists of microfluidic chambers containing biological and reference materials, an antimony-bismuth (Sb-Bi) thermopile for thermoelectric sensing, and thin-film resistive microheaters and temperature sensors. To enable AC-DSC, the differential thermal power between the sample and reference is measured, while the temperature of the chambers is varied at a specified rate with a periodic (AC) modulation. The device is highly sensitive due to improved thermal isolation and the use of the Sb-Bi thermopile for thermoelectric sensing, and allows minimized sample consumption in 1 μL of measurement volume. The integrated microheaters and temperature sensors enable *in-situ* AC heating and temperature sensing for accurate and efficient AC-DSC measurements and convenient device calibration. With these attributes, this MEMS AC-DSC approach can potentially enable highly efficient measurements of the thermodynamic characteristics of biomolecules with improved accuracy. This potential is demonstrated by the application of the device to AC-DSC measurements of the unfolding of lysozyme, which allow the determination of the thermodynamic properties associated with the conformational transitions of the protein.

5.2 Materials and Methods

5.2.1 Principle and Design

AC-DSC monitors the differential heat capacity, i.e., the heat capacity difference between a sample and a reference material, by varying the materials' temperatures at a specified constant rate via a thermally isolated enclosure equipped with temperature control functionalities, superimposed with a temporally periodic variation via identical AC modulation heating applied to the sample and reference (Figure 5-1). The differential heat capacity can be obtained by the measurement of the differential temperature, i.e., the temperature difference between the sample and reference materials [147].

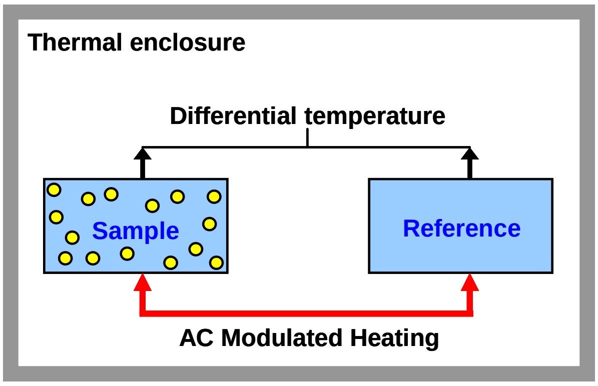

Figure 5-1: Principle of AC differential scanning calorimetry.

To enable AC-DSC measurements, we use a MEMS device combining highly sensitive thermoelectric sensing and microfluidic handling (Figure 5-2a) [147, 170]. The device consists of two identical poly(dimethylsiloxane) (PDMS) microchambers to contain sample and reference materials, respectively, for calorimetric detection. Each calorimetric chamber, i.e., the PDMS chamber containing the sample or reference material (or, sample or reference chamber), is situated on a freestanding polyimide diaphragm and surrounded by air gaps for maximum thermal isolation. This device features a multilayer configuration in which a layer of thin-film Sb-Bi thermopile is embedded in the diaphragms, with its hot and cold junctions located directly below the calorimetric chamber centers, to measure the minute differential temperature between the sample and reference materials. Another layer of thin-film resistive micro temperature sensors and heaters is also embedded in the diaphragms (Figure 5-2a). With alignment to the centers of calorimetric chambers, the temperature sensors are used to monitor the chamber temperatures in real time. Meanwhile, the microheaters are also aligned to the calorimetric chambers to provide uniform heating, from which a constant differential power can be generated for device calibration, and on-chip AC modulation heating can be directly achieved for AC-DSC measurements.

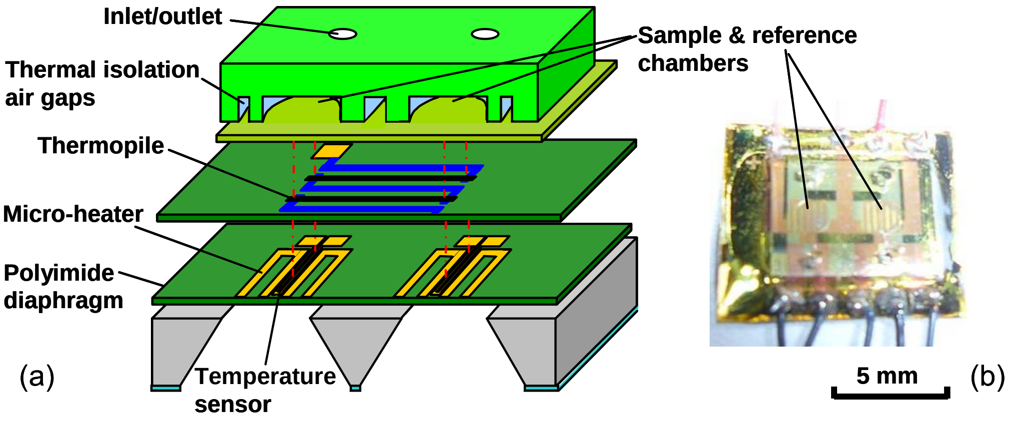

Figure 5-2: (a) Design schematic of the MEMS-based differential scanning calorimetric device. (b) A packaged device.

In considering the thermal leakage of the sample to the ambient environment, for simplicity we use a modulated electric current $I = I_0 \cos(\omega t)$ (ω is the modulation frequency) passing through the on-chip heater with constant resistance R [171]. It can be shown that when the heat transfer reaches steady state, the sample temperature consist of a DC component and an AC component whose amplitude is given by

$\Delta T_{\text{ac}} = I_0^{\ 2} R / (2k\sqrt{1+4\omega^2\tau^2})$, where K the thermal conductance between the sample and the ambient, $\tau = C / k$ the device's thermal time constant [171, 172], and C the total heat capacity of the sample and its containing chamber. If ω is chosen such that $\omega\tau >> 1$, then the AC temperature amplitude is approximately

$$\Delta T_{\text{ac}} = \frac{I_0^{\ 2} R}{4\omega C} \tag{5-1}$$

which is independent of the thermal conductance K. Therefore, the effects of the heat loss to ambient can be ignored in AC mode, minimizing a significant source of experimental error in non-adiabatic calorimetric measurements.

Using this MEMS device for AC-DSC measurements, the sample and reference chambers contain biological sample and buffer solutions, respectively. The device is placed in a thermally isolated enclosure whose temperature is varied at a constant rate, while a periodic modulation heating power is applied to the calorimetric chambers via the integrated microheaters. The differential temperature, indicative of the differential power between the sample and reference during biomolecular interactions, is then detected in terms of the AC-modulated voltage generated in the thermopile.

5.2.2 *Fabrication*

The MEMS device was fabricated using a process involving a thermal substrate bonded to a microfluidic structure [170]. In particular, the thermal substrate was fabricated from a silicon wafer, with cavities etched into the backside corresponding to the calorimetric chambers on the frontside to generate freestanding chambers [170]. The polyimide diaphragms, Cr/Au microheaters and temperature sensors, and Sb-Bi thermopile were patterned sequentially on the substrate, which was bonded to the microfluidic structure fabricated from PDMS using micromolding techniques [173]. The two circular calorimetric chambers of the device, each with a volume of 1 μL (diameter: 2.5 mm, height: 200 μm) and situated on a 6-μm thick polyimide diaphragm, were separated by a center-to-center distance of 4 mm. The Sb-Bi thermopile consisted of 100 thermoelectric junctions. The integrated microheaters each had a nominal resistance of 40 Ω and the resistive temperature sensors each had a nominal resistance of 55 Ω. A packaged device is shown in Figure 5-2b.

5.2.3 Experimental Method

During the experiment, the MEMS device was located in a thermal enclosure built in-house [170]. This thermal enclosure consisted of multiple metal enclosures surrounding a metal stage on which the device was placed to shield it from environmental disturbances [152]. Multiple Peltier devices were integrated underneath the device stage to generate the heat used for temperature scanning of the sample and reference solutions contained in the device. The temperature of the sample stage in the thermal enclosure was controlled in closed-loop via a PID algorithm implemented by a commercial temperature controller (Lakeshore 331). The on-chip microheaters driven by a DC power supply (Agilent E3631A) were used to generate a constant differential power input, while for modulation heating, a square-wave AC voltage generated by a waveform generator (Agilent 33220A) was applied (Figure 5-3). The temperature sensors were used to detect the real-time temperature inside each of the calorimetric chambers by a digital multimeter (Agilent 34410A). During device calibration, the thermopile output voltage was measured by a nanovoltmeter (Agilent 34420A), while during AC-DSC measurement, the amplitude and phase of thermopile voltage were measured by a lock-in amplifier

(Stanford Research Systems SR830) referenced by the same AC modulation square wave from the waveform generator. The AC-DSC measurement was fully automated through a LabVIEW program.

The DC performance of the MEMS device was calibrated using a known, constant differential power generated by activating the microheater below the sample chamber while the microheater underneath the reference chamber remained off. The baseline in device output, i.e., the thermopile voltage with no differential power input during temperature scanning, was measured with both chambers filled with buffer solutions. During calibration of the device's modulation frequency dependence and AC-DSC measurements, the sample chamber was filled with a biological sample solution while the reference chamber was filled with the buffer solution. Biological sample and buffer solutions were degassed with a vacuum pump built in house and then introduced into the device's calorimetric chambers with micropipettes.

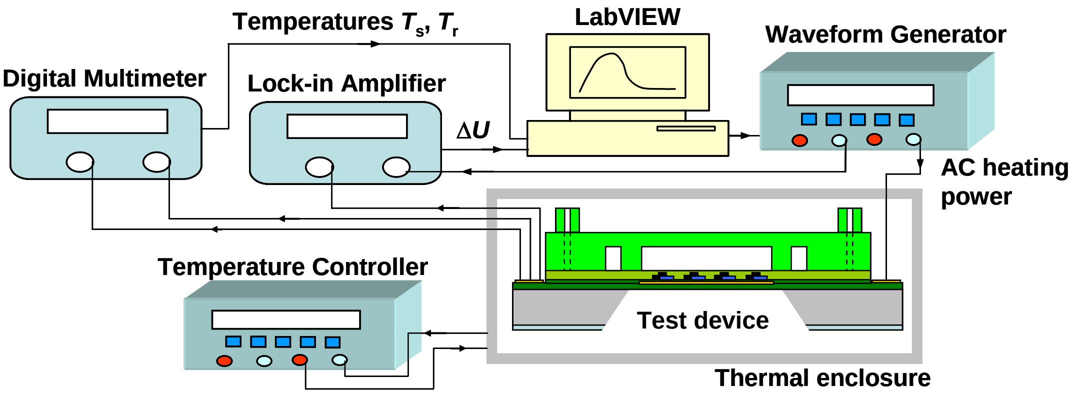

Figure 5-3: AC-DSC experimental setup.

5.3 Results and Discussion

5.3.1 Device Calibration

We first calibrated the thermopile integrated in the MEMS device and found that the 100-junction thermopile showed a sensitivity of 13.0 mV/ºC (Figure 5-4), corresponding to a Seebeck coefficient of (per Sb-Bi thermoelectric junction) of approximately 130 µV/ºC, which is consistent with data reported in the literature [154]. The steady-state response of the device to a constant differential power was then measured, and exhibited a highly linear relationship with a DC responsivity of 8.0 mV/mW (Figure 5-5). These results were consistent with calibration results from a device with an integrated 50-junction Sb-Bi thermopile [170].

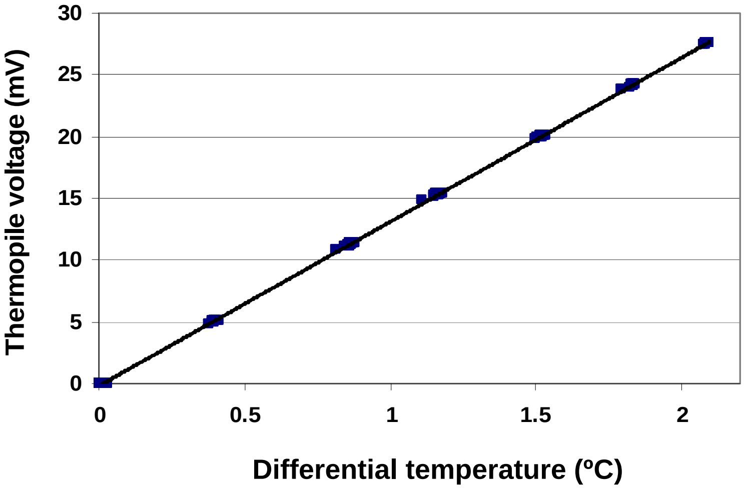

Figure 5-4: Output voltage of the thermopile integrated in the MEMS device in response to constant differential temperature between its hot and cold junctions.

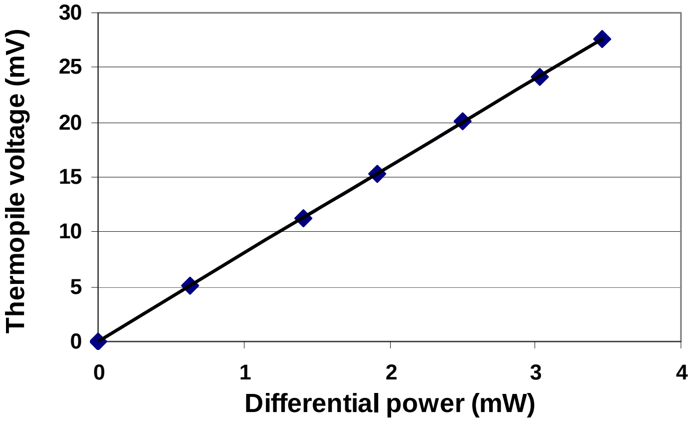

Figure 5-5: Steady-state response of the MEMS device to a constant differential power between the calorimetric chambers.

Additionally, we characterized the transient response of the device. The calorimetric chambers, both of which were filled either with air or with 0.1 M Glycine-HCl buffer (pH 2.5), were subjected to a step differential power (0.32 or 1.30 mW). Results from these characterization measurements are shown in Figure 5-6. The dependence of the thermopile voltage on time can be well represented by a first order exponential increase. The thermal time constant thus obtained was 0.8 s when the chambers were filled with air, and 2.0 s when they were filled with buffer solution. These values were independent of the applied differential power, and were desirably smaller than conventional AC calorimetric measurements [169].

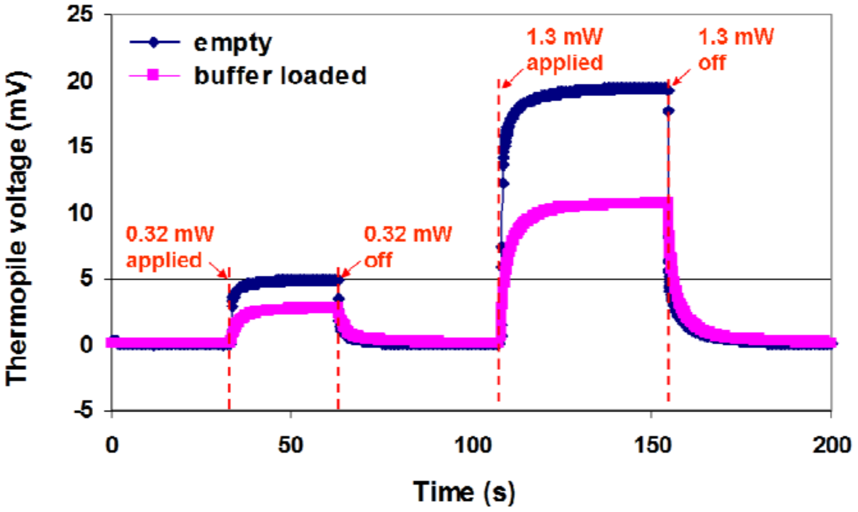

Figure 5-6: Transient response of the MEMS DSC device when the sample chamber was heated with a step power while the reference chamber was unheated.

5.3.2 Modulation Frequency Dependence

We further investigated the modulation frequency dependence of the device response to the applied differential power. To better simulate the application for AC-DSC measurement of protein unfolding process, the sample chamber was filled with lysozyme (20 mg/mL, prepared in 0.1 M Glycine-HCl, pH 2.5) as a sample, while the reference chamber was filled with Glycine-HCl buffer. The chambers were maintained at a constant temperature (25, 35, or 45 °C), and subjected to AC heating (voltage amplitude: 1 V). The dependence of the thermopile voltage amplitude on the modulation frequency, corrected by baseline subtraction, is shown in Figure 5-7. It can be seen that the thermopile voltage increased with temperature at almost all modulation frequencies, which can be explained by the temperature-dependence of the protein's heat capacity. More importantly, the device output (and hence sensitivity) was maximized in a modulation frequency range of 0.5 to 20 Hz (Figure 5-7), suggesting a reduced heat loss to the ambient by choice of modulation frequency [167]. Therefore, modulation frequencies in this range were used below in calorimetric measurements of protein unfolding processes.

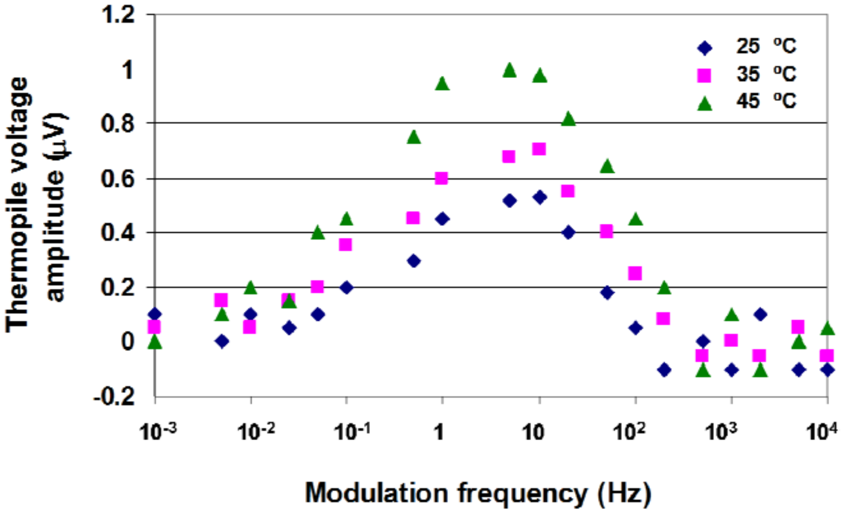

Figure 5-7: Frequency dependence of the thermopile voltage amplitude (baseline subtracted) when the sample chamber was filled with lysozyme (20 mg/mL) and the reference chamber was filled with 0.1 M Glycine-HCl buffer (pH 2.5).

5.3.3 AC-DSC Measurements of Protein Unfolding

The MEMS AC-DSC device was used to measure the thermal behavior of protein unfolding. Using lysozyme at different concentrations (10 and 20 mg/mL, prepared in 0.1 M Glycine-HCl buffer, pH 2.5) for example, the temperature of the calorimetric chambers was varied from 25 to 82 °C at a rate of 5 °C/min in combination with AC modulation via a heating voltage amplitude of 3.5 V at a constant frequency (1, 5, or 10 Hz). The periodic temperature variation resulting from the AC modulation heating had an amplitude of approximately 0.2 ºC.

The measured thermopile voltage amplitude (Figure 5-8a), again corrected by baseline subtraction, showed a concentration-dependent dip during the unfolding process, consistent with the endothermic nature of protein unfolding [56]. In addition, despite differences in thermopile voltage amplitude for different lysozyme concentrations, the phase of the thermopile voltage (Figure 5-8b) had identical changes throughout the unfolding process, which remained unchanged in the native and unfolded states when a two-state protein denaturation model was adopted [56, 155]. Furthermore, both the amplitude and phase changes of the thermopile voltage exhibited clear shifts with the modulation frequency (Figure 5-8), which could be attributed to the unsynchronized thermal response of the device to AC heating [167]. However, at a fixed protein concentration, the profiles of the thermopile voltage amplitude and phase changes had virtually the same shape (Figure 5-8) at different modulation frequencies, showing the suitability of the frequency choice for our MEMS-based AC-DSC measurements.

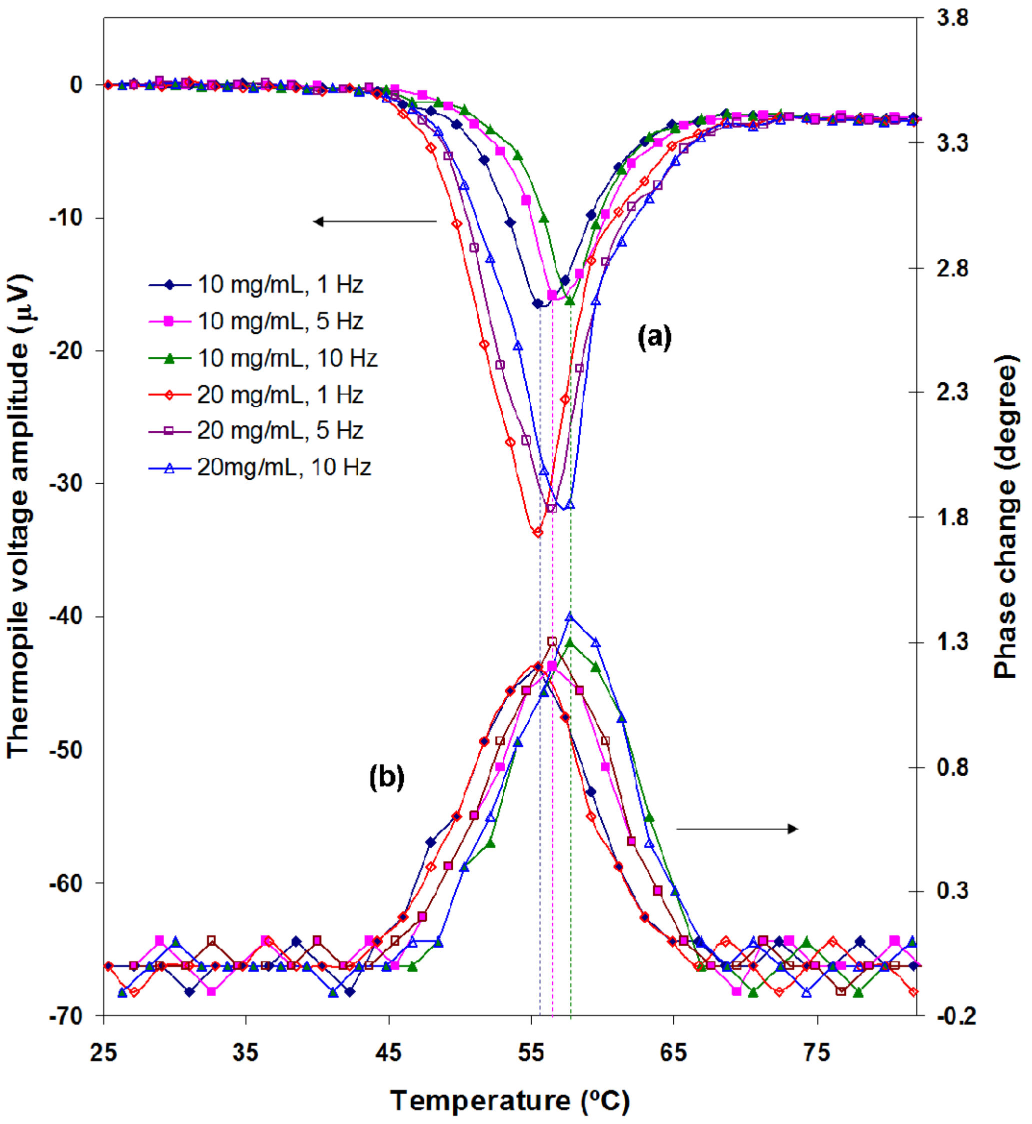

Figure 5-8: Changes in (a) amplitude, and (b) phase, of the thermopile voltage as a function of temperature during the unfolding of lysozyme at different lysozyme concentrations and AC modulation frequencies.

5.3.4 *Determination of Thermodynamic Properties*

The apparent melting temperature (T_m) of lysozyme during an unfolding process, i.e., the temperature at which the phase change of device output reaches its peak [167], was found to be in the range of 55-58 ºC (Figure 5-8), depending on the modulation frequency. Furthermore, we can determine the differential heat capacity (ΔC_p) between the protein and reference solutions using the measured thermopile voltage amplitude (ΔU) and the following equation [147]

$$\Delta C_{\mathrm{p}} = \Delta U / (S\dot{T}) \tag{5-2}$$

where $\dot{T}$ is the time rate of the controlled temperature of sample and reference materials, and S is the calibrated thermoelectric sensitivity, i.e., the output electrical voltage generated by unit differential thermal power.

In turn, the partial specific heat capacity (c) of the protein as a function of temperature (Figure 5-9) can be determined as [147]

$$c = c_{\mathrm{solv}}(v / v_{\mathrm{solv}}) + \Delta C_{\mathrm{p}} / m \tag{5-3}$$

where c and c_{solv} are the partial specific heat capacities of the biomolecule and reference solvent, respectively, m is the mass of the biomolecule in the sample chamber, and v and v_{solv} are the partial specific volumes of biomolecules and the reference solvent, respectively.

It can be seen in Figure 9 that although there again existed a slight shift in c throughout the unfolding process induced by modulation frequency, the profile shape of c was not influenced by the modulation frequency. Moreover, at each modulation frequency, the calculated value of c does not differ significantly at different protein concentrations (Figure 5-9), showing that the AC-DSC measurements were accurate. There was also a difference in the specific heat capacity (Δc) between the protein's native and unfolded states, which was calculated to be approximately 3.0 kJ/mol·K regardless of the modulation frequency. Note that there were small differences in the value of Δc at different lysozyme concentrations possibly due to protein aggregation at the higher concentrations. By integrating *c* during the protein unfolding process, we determined the total change of molar enthalpy (i.e., enthalpy per mole of lysozyme) to be in the range of 350-380 kJ/mol, which is slightly lower than published data obtained from DC-DSC characterization (377-439 kJ/mol) [155]. This could be attributed to limitations in the bandwidth and signal acquisition rate of the current measurement instrumentation, which would allow measurements at only a limited number of temperatures. Future work will address these instrumentation limitations (e.g., via inclusion of high-speed signal processing capabilities) as well as improve the MEMS DSC device sensitivity (e.g., by use of calorimetric microstructures with increased thermal isolation), thereby allowing accurate AC-DSC measurements of small volumes of biomolecular samples at practically low concentrations.

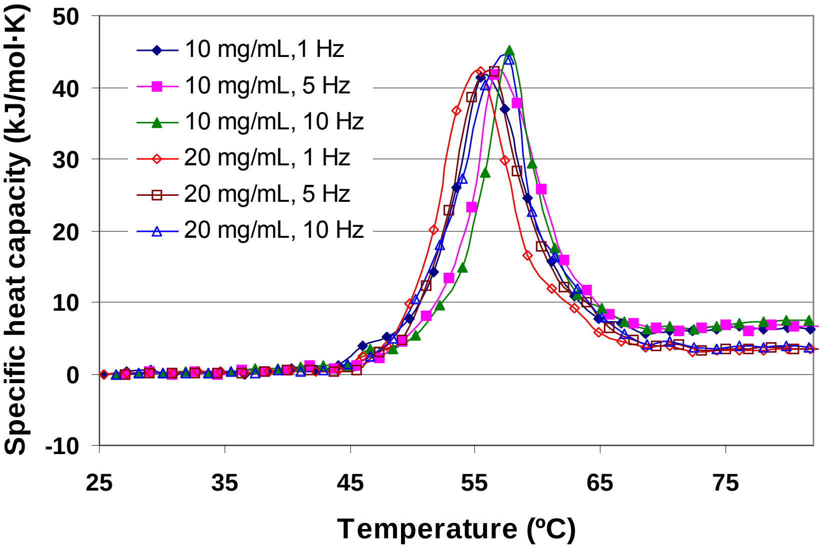

Figure 5-9: Specific heat capacity of lysozyme as a function of temperature during the unfolding of lysozyme at different lysozyme concentrations and AC modulation frequencies.

5.4 Conclusions

This chapter presents AC-DSC characterization of liquid biomolecules in a MEMS device. The device consists of two PDMS microfluidic calorimetric chambers each 1 μL in volume. The chambers are each surrounded by air gaps and based on a freestanding polyimide diaphragm, offering excellent thermal isolation. The diaphragms are integrated with resistive microheaters and temperature sensors as well as a 100-junction Sb-Bi thermopile for thermal control and sensing. The differential power between a sample and a reference material contained in the chambers is measured via the thermopile, while the chamber temperature is varied at a specified rate, with a periodic modulation component provided by the on-chip heaters.

Characterization of the device yielded a DC responsivity of 8 mV/mW and a thermal time constant of approximately 2.0 s. The frequency response of the device indicated that optimal sensitivity could be obtained in a modulation frequency range of 0.5–20 Hz. Measurement of the unfolding of lysozyme at concentrations of 20 and 10 mg/mL using the device was performed at modulation frequencies of 1, 5, and 10 Hz, yielding consistent results representing the protein's two-state conformational transition. The specific heat capacity and the melting temperature during the unfolding process were calculated and found to agree with widely accepted data in the literature. These results demonstrate the potential of MEMS-based AC-DSC for thermodynamic characterization of biomolecules.

Chapter 6 A MEMS Isothermal Titration Biocalorimeter

This chapter presents a MEMS ITC device for characterization of biomolecular interactions. The MEMS device consists of two identical microchambers, each situated on a freestanding diaphragm and surrounded by air cavities for effective thermal isolation. The chambers are integrated with a thin-film Sb-Bi thermopile and connected to the inlets through a passive chaotic micromixer. The mixer uses herringbone-shaped ridges in the ceiling of a serpentine channel to generate a chaotic flow pattern that induces mixing of the incoming liquid streams. For ITC measurements, the sample and binding reagent introduced into the device are first mixed before they enter the reaction calorimetric chamber. Meanwhile, the sample and pure buffer are also introduced, becoming mixed before entering the reference calorimetric chamber. The differential temperature between the chambers is measured using the integrated thermopile, and is used to compute the thermal power from the reaction, and in turn, the thermodynamic parameters. We demonstrate experimental results of the biomolecular interactions, using binding systems of 18-Crown-6 (18-C-6) and barium chloride ($BaCl_2$), as well as ribonuclease A (RNase A) and cytidine 2'-monophosphate (2'CMP), in a 1-μL volume at concentrations as low as 2 mM. Consistent temperature-dependent thermodynamic properties of the biomolecular binding, including the stoichiometry, equilibrium binding constant, and enthalpy change, are obtained and found to agree with published results using conventional calorimeters.

6.1 Background

ITC directly measures heat evolved in a biochemical reaction as a function of the molar reactant ratio, and simultaneously determines all binding parameters, providing an efficient, high-precision, label-free method for characterization of biomolecular interactions [63]. Conventional ITC instruments [174], however, have been limited by complicated structural design, slow thermal response, and large sample and reagent consumption. These issues can potentially be addressed by miniaturization via MEMS technology. MEMS-based calorimetric devices can have unique advantages over conventional instruments, including reduced sample consumption, rapid time response, and improved throughput [164]. While MEMS technology holds the potential in improved biocalorimetry for characterization of biomolecular interactions, this opportunity has not been extensively explored. One major issue with MEMS calorimetric devices is the inadequate capability of handling liquid biochemical samples, representing by their general use for solid- or gas-phase samples [101, 175], or for liquid-phase samples without fluidic confinement [176] or integrating with off-chip external flow cells [103].

Recently, by integrating microfluidic functionalities and MEMS-based thermal transduction, several microfluidic calorimeters featuring sensitive detection of the reaction of liquid samples have been reported [177-180]. In terms of microfluidic handling, there are currently two major types of microfluidic calorimeters: flow-through calorimeters [181, 182] in which micro-chambers or channels are used as biological reactors while sample solutions are introduced by continuous flows, and droplet-based calorimeters [183] in which discrete sample droplets are generated and transported to a surface for thermal detection. However, when used for characterization of biomolecular interactions, the flow-through calorimeters still consume considerable amount of samples and conduct measurements without well-defined volumes, which makes it difficult to obtain quantitative information associated with the reaction; while the droplet-based calorimeters typically have complicated design due to on-chip droplet generation and manipulation, and are significantly affected by energy dissipation via evaporation.

Furthermore, with the function of titration, i.e., introduction of reactants at controlled molar ratios, incorporated into microfluidic calorimeters [184], there have been a few attempts of integrated ITC measurements of biochemical interactions on MEMS devices. By continuous in-channel delivery of reactants with varying molar rates to a flow-focusing junction, the heat flux upon the chemical reaction was measured and used to calculate the enthalpy change [185]. By varying the concentrations of reactant solutions that were deposited to form individual droplets, the reaction heat was measured as a function of reactants' molar ratio [111]. Also by sequential injections of small droplets containing a reactant to a larger droplet containing the other reactant, the reaction heat per injection was measured in real time [186]. Despite the demonstration of ITC, these devices are generally difficult to accurately control the environment where the reactions are measured [187]. For example, the reaction temperature, an important parameter for thermodynamic characterization as biological processes are ubiquitously temperature-dependent, was not properly controlled. Moreover, the existing MEMS calorimeters generally lack mixing functionalities which can be critical for reaction of microfluidic sample solutions [188]. Although on-chip micro-mixers have been integrated in microfluidic devices for potentiometric detection of biochemical reaction [189], their application in MEMS calorimeters has yet to be explored.

Here we present a MEMS-ITC device aiming at addressing these critical issues. The device integrates two microfluidic chambers for reaction and reference, respectively, situated on freestanding diaphragms and surrounded by air cavities for effective thermal isolation. Each calorimetric chamber is connected to the inlets through a passive chaotic mixer [190] to allow for a single-injection of the reactant solutions (each 0.5 μL) to be fully mixed before entering the reaction calorimetric chamber, and simultaneously a single-injection of buffer solutions entering the reference chamber. A sensitive thermopile is integrated in the diaphragm for thermoelectric detection of the biochemical reaction heat. The device is tested in a custom-built thermal enclosure that shields environmental disturbance and provides well-controlled temperatures to measurements. This device allows MEMS-based ITC measurements with well defined miniature reaction volumes and at properly controlled temperatures. We apply this device for temperature-dependent characterization of biochemical reaction and ligand-protein binding at sample concentrations as low as 2 mM, demonstrating the potential of efficient thermodynamic characterization of biomolecular interactions with minimized sample consumption.

6.2 Materials and Methods

6.2.1 Principle and Design

ITC measures reaction heat as a function of the molar ratio of the reactants. Consider a solution-phase biochemical reaction

$$n_1\mathrm{X} + n_2\mathrm{M} \rightleftharpoons \mathrm{MX} + \Delta H \tag{6-1}$$

where X is a binding reagent (i.e., a ligand) reacting with a sample molecule M, resulting in the product MX accompanied by a change of enthalpy ΔH. In ITC, the ligand is titrated, i.e., successively added in known aliquots, into the sample, while the reaction heat is measured. This data is then used to calculate the thermodynamic properties of the reaction, including the equilibrium binding constant K_B = [MX]/[X][M] ([·] denotes the equilibrium concentration of the species), stoichiometry $N = \mathrm{n}_1/\mathrm{n}_2$, and molar enthalpy change (ΔH). In particular, if the ligand and sample have a single set of identical binding sites [191], the biochemical reaction heat can be expressed as [191]

$$Q = \frac{NM_t \Delta H V_0}{2}\left[1 + \frac{r}{N} + \frac{1}{NK_B M_t} - \sqrt{(1 + \frac{r}{N} + \frac{1}{NK_B M_t})^2 - \frac{4r}{N}}\right] \tag{6-2}$$

where Q is the biochemical reaction heat evolved at a molar ratio $r = \frac{X_t}{M_t}$, V_0 is the active volume for reaction, M_t is the total concentration of the sample, free plus bound, in the reaction cell of volume V_0, and X_t is the total concentration of the ligand that is titrated into the sample solution.

The reaction heat is calculated based on the monitoring of the bio-thermal power during the reaction. ITC measurements usually use a differential scheme in which two calorimetric chambers are exploited for the reaction and reference, respectively. Both chambers are filled with the sample solution, while the reaction and reference chambers are titrated with the binding reagent and buffer solution, individually. The biochemical reaction, either exothermic or endothermic, induces a thermal power difference between the calorimetric chambers: $\Delta P = P_s - P_r$, where P_s and P_r are the thermal power in the reaction and reference chamber, respectively. A thermoelectric sensor can be used to detect the differential power [147]

$$\Delta P = \frac{\Delta U}{S} \tag{6-3}$$

where ΔU is the output from the thermoelectric sensor and S is the thermoelectric sensitivity, i.e., the output electrical voltage generated by unit differential thermal power [147, 170].

The MEMS-ITC device integrates two identical PDMS microchambers each situated on a freestanding polyimide diaphragm and surrounded by air cavities for effective thermal isolation. The chambers are each connected to the inlets through a passive chaotic micromixer. The mixer uses herringbone-shaped ridges in the ceiling of a serpentine channel (Figure 6-1a) to generate a chaotic flow pattern that induces mixing of the incoming liquid streams [190]. The diaphragm embeds a layer of thin-film Sb-Bi thermopile with its cold and hot junctions located underneath the centers of the calorimetric chambers to measure the thermal power difference between the reaction and the reference (Figure 6-1b). Each calorimetric chamber is also equipped with integrated thin-film resistive micro-temperature sensor and heater for *in-situ* temperature monitoring and on-chip device calibration [170].

For ITC measurements, the sample and ligand introduced into the device are first mixed in the mixer, and then enter the reaction calorimetric chamber, where the reaction is completed. In the same time, the sample and pure buffer are also introduced into the device, becoming mixed before entering the reference calorimetric chamber. The differential temperature between the chambers is measured using the integrated thermopile, and is use to determine the thermal power from the reaction, from which the thermodynamic reaction parameters are calculated.

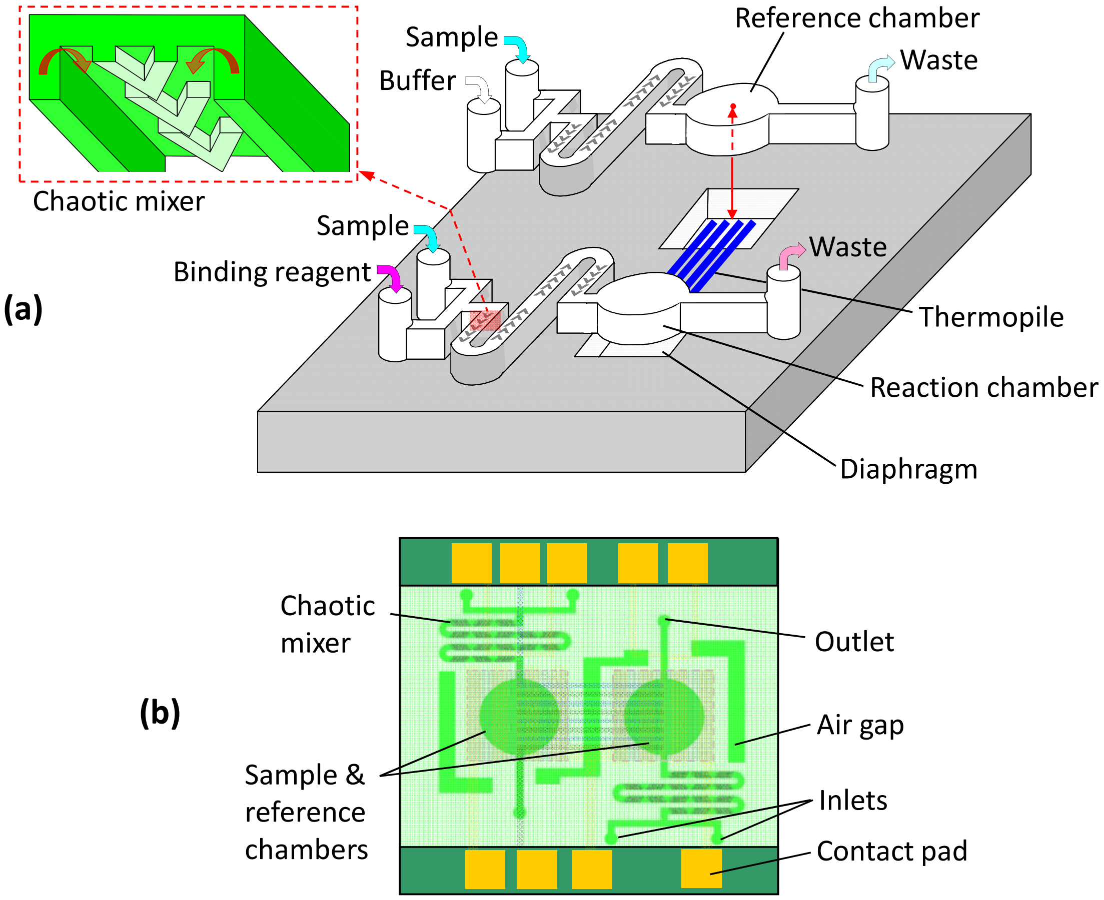

Figure 6-1: (a) MEMS-ITC design and (b) top view of the device schematic.

6.2.2 Fabrication and Measurement Setup

The fabrication of the MEMS-ITC device was described elsewhere [170]. In particular, the chaotic mixers and the calorimetric chambers were fabricated in a single sheet using PDMS replica technique based on multiple-layered SU-8 molding [173]. The microfabricated device integrated a 50-junction Sb-Bi thermopile and two 0.75-µL calorimetric chambers with a center-to-center separation of 4 mm. The calorimetric chambers had a cylindrical shape with a height of 150 µm and a diameter of 2.5 mm. The chaotic mixers were serpentine microchannels (width: 200 μm, height: 150 μm, length: approximately 15 mm) with herringbone-shaped ridges on the ceiling which each had a width of 40 μm, a height of 50 μm, an orientation angle of 60° to the channel sidewall, and a edge-to-edge distance between adjacent ridges of 30 μm. The nominal resistances of the integrated resistive microheaters and temperature sensors were 40 Ω and 55 Ω, respectively. Figure 6-2 shows the images of important elements in the thermal substrate and PDMS structure, including the embedded thermopile, micro-temperature sensor, calorimetric chamber and chaotic mixer.

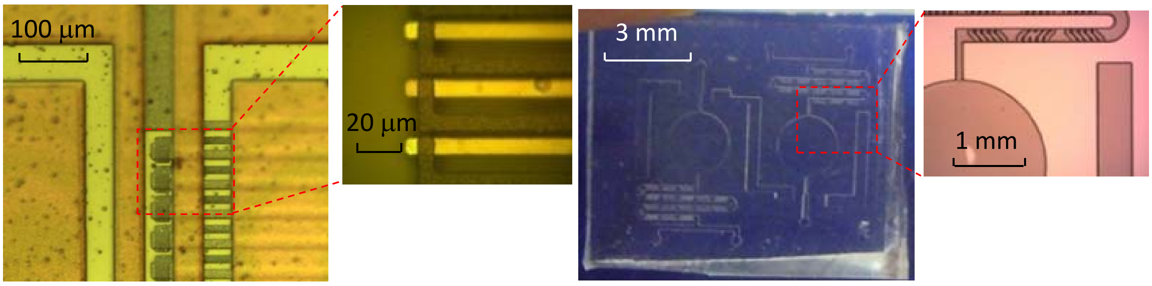

(a) (b)

Figure 6-2: Fabrication Images of important chip elements: (a) the thermopile junctions and temperature sensor; (b) the PDMS calorimetric chambers and chaotic mixers.

To test the MEMS-ITC device, a thermal enclosure was custom-built to house the device (Figure 6-3) to shield thermal disturbance from ambient, as well as provide uniform temperature control to the solutions loaded in the device. The general design scheme of the thermal enclosure was described elsewhere [170]. For MEMS-ITC measurements, this thermal enclosure was improved with additional thermal isolation by suspending the sample stage from the base, vibration isolation by enhanced base mass and rubber buffering layer, and multiple-ports microfluidic feedthrough to the device. The temperature control of the thermal enclosure was implemented by a commercial temperature controller (Lakeshore Model 331). The device was first packaged with electrical interconnection wires and fluidic interconnection tubes before it was situated on the sample stage inside the thermal enclosure.

The on-chip microheaters, used for device calibration, were driven by a DC power supply (Agilent E3631A) and generated a constant differential heating power in the calorimetric chambers. The on-chip temperature sensors, used for *in-situ* temperature monitoring of the calorimetric chambers, were interrogated by a digital multimeter (Agilent 34410A). The thermopile output voltage, which is proportional to the differential temperature between the chambers, was measured by a nanovoltmeter (Agilent 34420A). The temperature monitoring of the calorimetric chambers and thermoelectric measurements were automated using a personal computer via a LabVIEW-based program (Figure 6-3). The biological sample and buffer solutions were degassed with a vacuum chamber built in-house, metered introduced into the MEMS-ITC device using a multiple-injections syringe pump (KD Scientific, KDS 220).

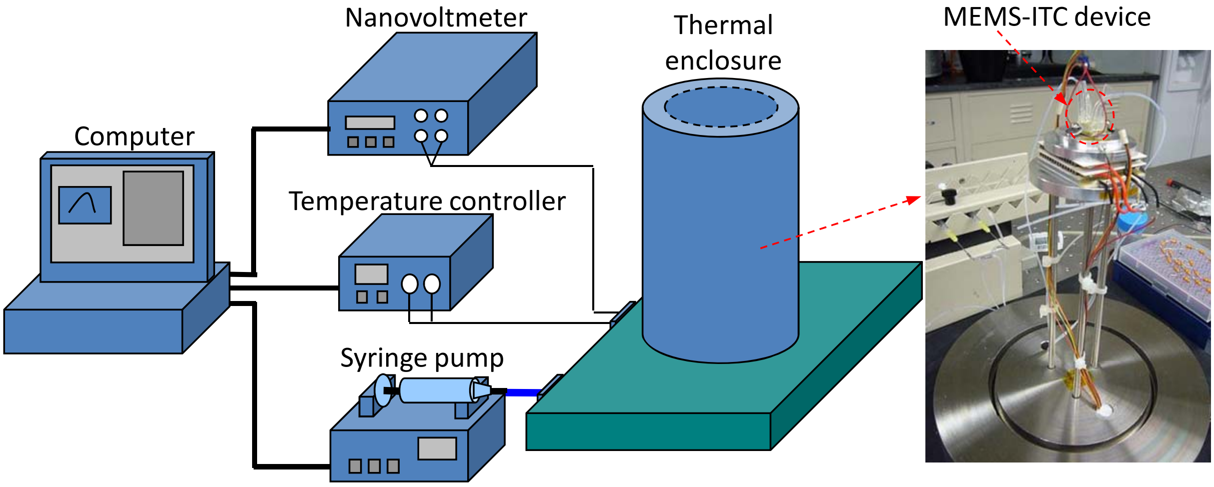

Figure 6-3: Images Testing setup for the MEMS-ITC device, with an inset showing the device situated inside the thermal enclosure.

6.2.3 *Experimental Method*

The device was first calibrated by measuring its steady-state and transient response to differential power generated by on-chip microheaters as described elsewhere [170]. Before ITC measurements, the baseline in device output, i.e., the thermopile output voltage in the absence of reaction, was measured with introduction of sample and buffer solutions to both calorimetric chambers. During ITC measurements, the thermal enclosure provided a controlled reaction temperature while the thermopile output, indicative of the differential bio-thermal power, was detected in real time, as well as the integrated micro-temperature sensor to monitor the temperatures of calorimetric chambers. The volume of ligand and sample was fixed at 0.5 μL for each injection, while the molar ratio was adjusted by changing the concentration of ligand to be injected. The baseline in device output was always subtracted from the measurement signal for determination of thermodynamic properties of biomolecules.

6.3 Result and Discussion

6.3.1 *Device Calibration*

We first calibrated the thermal time constant of the MEMS-ITC device by applying a step differential power of 90 μW initially and then turned it off once the device output reached its equilibrium. The device output voltage was found to fit to first-order exponential growth and decay functions upon the application and removal of the differential power, respectively, from which the thermal time constant was determined to be approximately 1.5 s (Figure 6-4a). In addition, we calibrated the steady-state response of the device to varying differential power and observed a linear relationship showing a constant thermoelectric sensitivity of *S*=4.9 mV/mW (Figure 6-4b). We also calibrated the device's sensitivity at controlled temperatures (provided by the thermal enclosure) from 20 to 45°C, and found it remained almost unchanged with a relative standard deviation of less than 3%.

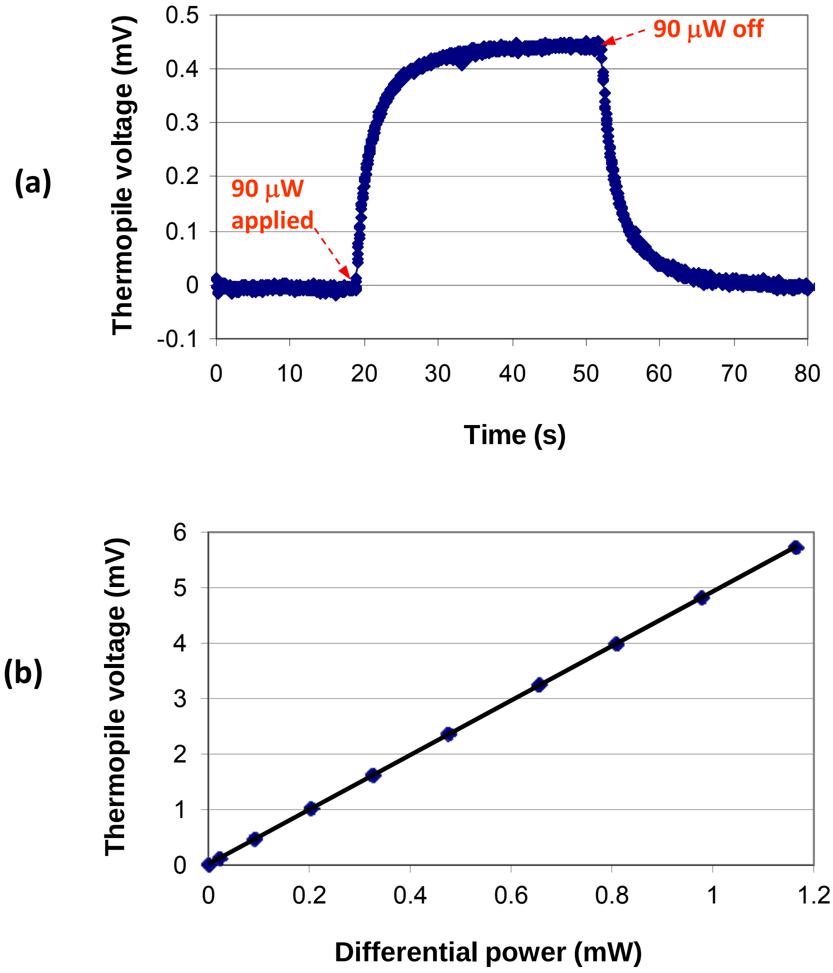

Figure 6-4: Calibration of the MEMS-ITC device using on-chip differential heating power between the calorimetric chambers. (a) Transient response to a step differential power. (b) Steady-state response to a constant differential power.

6.3.2 Detection Specificity to Titration

We then tested the baseline stability and detection specificity using a standard chemical reaction of 18-Crown-6 (18-C-6) and barium chloride ($BaCl_2$) both prepared in sterile water (all chemicals from Sigma Aldrich). Using a flow rate of 50 μL/min, the solutions were injected into the calorimetric chambers within 1 s. Using a data acquisition rate of 2 s^{-1} to monitoring the device output in real time, we did not see appreciable delay after injection, indicating full mixing of the reactants. Figure 6-5 showed the time-resolved thermopile voltage upon introduction of 4 mM $BaCl_2$ and 5 mM 18-C-6 (each 0.5 μL) in the reaction chamber, compared with the signal upon introduction of sterile water and 5 mM 18-C-6 (also each 0.5 μL). For both measurements, the reference chamber was injected with sterile water and 5 mM 18-C-6, and a data acquisition rate of 0.2 s^{-1} was used due to instrument configuration for lower background noise. As can be seen from Figure 6-5, the device exhibited a stable baseline throughout the measurements and a reaction-specific spike attributable to the exothermic nature of the binding between 18-C-6 and $BaCl_2$. Also note that the reaction completed in approximately 20-30 s, during which interference from solution injection and mixing were generally negligible.

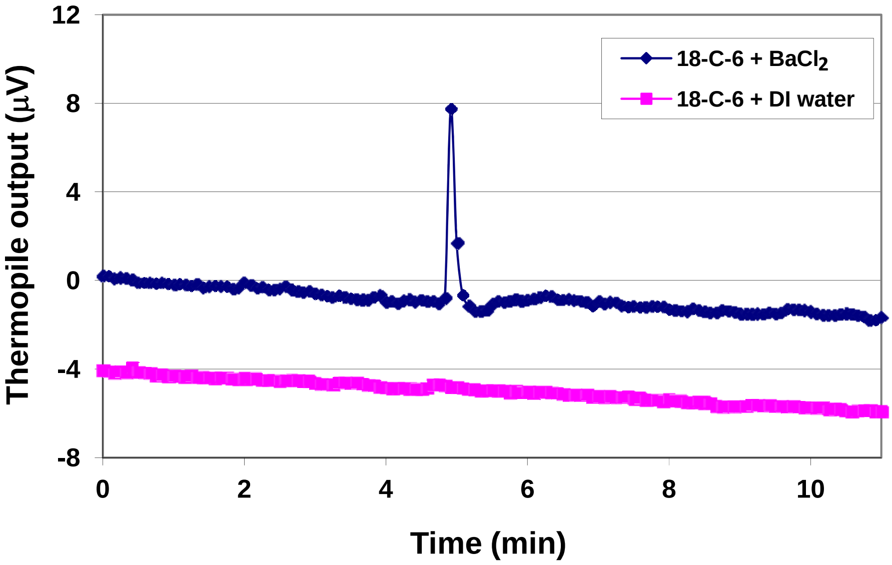

Figure 6-5: Time-resolved device output upon introduction of 5 mM 18-C-6 and 4 mM BaCl2 (each 0.5 µL), compared with measurement of 5 mM 18-C-6 titrated by DI water. (The traces are intentionally plotted with an offset of 4 µV for clarity.)

6.3.3 ITC Measurement of Biochemical Reactions

We then used the calibrated MEMS-ITC device to characterize biomolecular interactions. We first used the $BaCl_2$-18-C-6 reaction to validate our ITC measurements [192]. By varying the molar ratio ($M_{BaCl2}/M_{18\text{-}C\text{-}6}$) from 0.1 to 2, the baseline-subtracted device output (Figure 6-6a) demonstrated spikes consistent with the titration reactions. Rather than measuring the heat evolved with the addition of several aliquots of $BaCl_2$ to a single sample of 18-C-6 as performed in commercial ITC instruments [174], our ITC experiment was performed at discrete measurements [111] each with a definite concentration of $BaCl_2$ (0.5–10 mM) and a fixed concentration of 18-C-6 (5 mM). Each measurement was completed in approximately 5 min.

The thermopile voltage was then used to calculate the bio-thermal power based on Eq. (6-3), and in turn the reaction heat by integral of the bio-thermal power during the process. The reaction heat as a function of reactant molar ratio generated a binding isotherm [111, 174], from which the thermodynamic properties can be obtained through fitting to the analytical model (Eq. (6-2)). The binding isotherm of the reaction of 18-C-6 and $BaCl_2$, as well as the fitted curve, is shown in Figure 6-6b, with error bars representing the standard deviation from three measurements at each molar ratio. Note that for this specific $BaCl_2$-18-C-6 system, our device affords detectable sample concentrations approaching those of conventional instruments (ca. 1 mM) [1] with roughly three orders of magnitude reduction in volume.

(a)

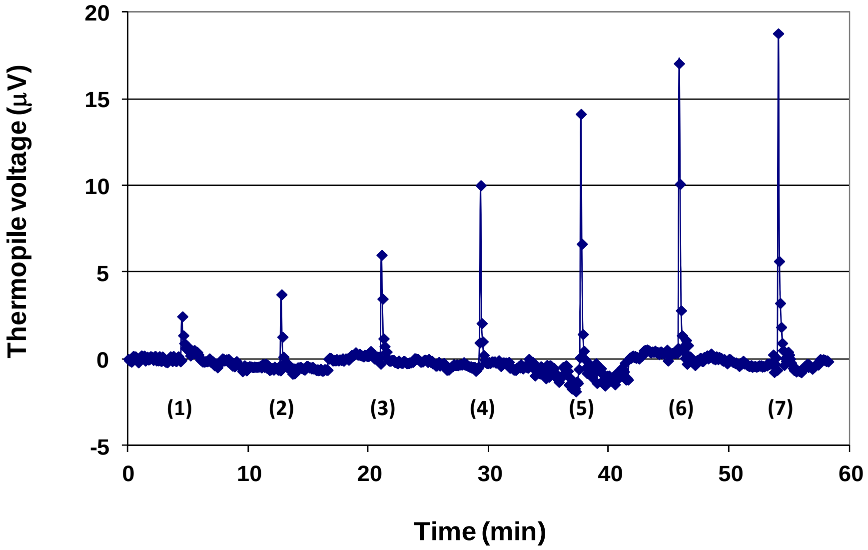

Titration	Molar Ratio
(1)	0.1
(2)	0.4
(3)	0.8
(4)	1.0
(5)	1.2
(6)	1.6
(7)	2

(b)

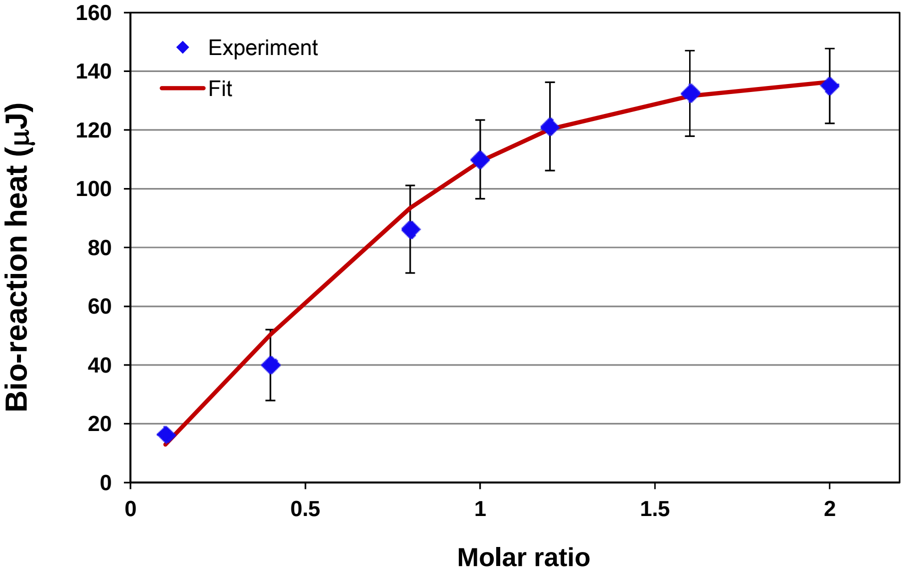

Figure 6-6: (a) Device output (baseline subtracted) of the binding of 5 mM 18-C-6 and $BaCl_2$ at a series of molar ratios ($M_{BaCl2}/M_{18\text{-}C\text{-}6}$): (1) 0.1, (2) 0.4, (3) 0.8, (4) 1.0, (5) 1.2, (6) 1.6, (7) 2.0. (b) Calculated biochemical heat of the binding of 18-C-6 and BaCl2 (error bars included) as a function of molar ratio, as well as the fitted curve to the identical binding-site model.

6.3.4 Determination of Temperature-Dependent Thermodynamic Properties

We performed ITC measurements of the biochemical reaction of 18-C-6 and $BaCl_2$ at controlled temperatures of 23 and 35 ºC, and used the resulting binding isotherms to compute the temperature-dependent thermodynamic properties of N, K_B and ΔH (Table 6-1). In particular, as temperature increases from 23 to 35 ºC, N slightly increases from 1.00 to 1.05, while K_B decreases from approximately 6.0×10^{-3} to 2.0×10^{-3} M^{-1} and ΔH decreases from 30.0 to 27.8 kJ/mol, showing a trend of slightly weaker binding with temperature. These properties and their temperature dependence obtained by our measurements agree reasonably with published data using commercial calorimeters [193] (Table 6-1).

Table 6-1: Temperature-dependent thermodynamic properties: the stoichiometry (N), binding affinity (K_B), and molar enthalpy change (ΔH), of the binding of 18-C-6 and $BaCl_2$ at controlled temperatures of 23 and 35 °C, compared with published data under similar experiment conditions [193].

	Temperature (°C)	**Stoichiometry (N)**	**K_B (M^{-1})**	**ΔH (kJ/mol)**
Our results	23	1.00	$\sim 6.0\times 10^3$	30.0
	35	1.05	$\sim 2.8\times 10^3$	27.8
Published data	25	1.01	5.63×10^3	29.9
	40	0.97	3.17×10^3	29.4

6.3.5 Temperature-Dependent Characterization of Biomolecular Interactions

We further applied the MEMS-ITC device for characterization of biomolecular interactions, e.g., ligand-protein binding, using a demonstrative system of cytidine 2’-monophosphate (2’CMP) and ribonuclease A (RNase A) (Sigma Aldrich). 2’CMP is known as a strong inhibitor of substrates that bind to the active site of RNase A [174]. Both reagents were prepared in 50 mM potassium acetate buffer, pH 5.5. Similarly, at varying molar ratios ($M_{2'CMP}/M_{RNase\ A}$) from 0.1 to 2, the device output exhibited titration-dependent spikes in correspondence to the molar ratio (Figure 6-7). We also performed ITC measurements of 2’CMP-RNase A binding at controlled temperatures of 23 and 35 °C with error bars from three measurements at each molar ratio (not shown). In turn, the temperature-dependent thermodynamic properties associated with this biomolecular interaction were determined (Table 6-2) from fitting the experimental data to the described model (Eq. (6-2)). The results from our measurements again agreed reasonably well with published data using commercial ITC instruments [174]. For 2’CMP-RNase A interaction, the reasonably detectable concentration of RNase A can be as low as 2 mM. These results demonstrate the potential utility of this MEMS-ITC device for efficient characterization of a wide variety of biomolecular interactions.

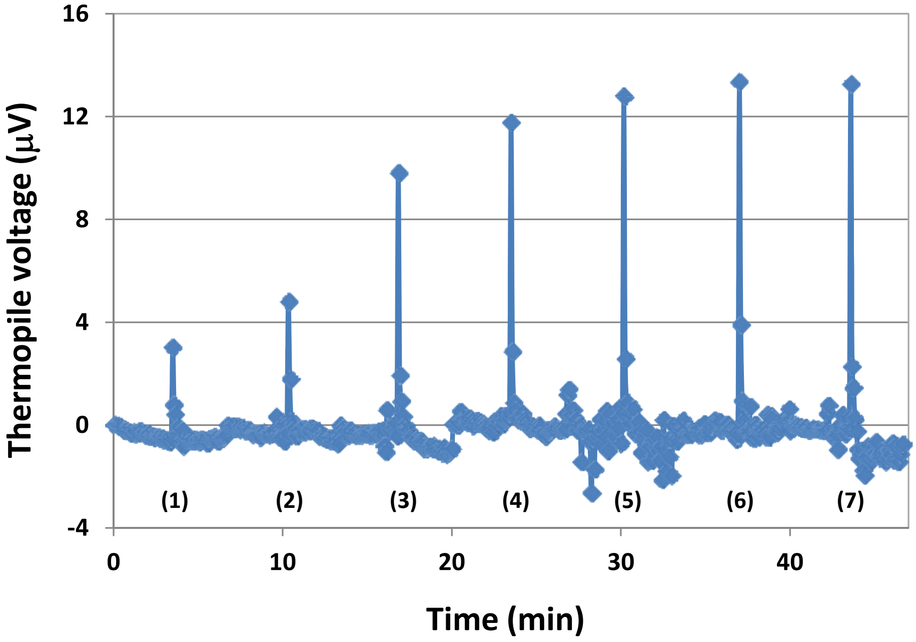

Titration	Molar Ratio
(1)	0.1
(2)	0.4
(3)	0.8
(4)	1.0
(5)	1.2
(6)	1.6
(7)	2

Figure 6-7: Device output (baseline subtracted) of the binding of 2 mM RNase A and 2'CMP at a series of molar ratios ($M_{2'CMP}/M_{RNase\ A}$): (1) 0.1, (2) 0.4, (3) 0.8, (4) 1.0, (5) 1.2, (6) 1.6, (7) 2.0.

Table 6-2: Temperature-dependent thermodynamic properties: the stoichiometry (N), binding affinity (K_B), and molar enthalpy change (ΔH), of the binding of RNase A and 2'CMP at controlled temperatures of 23 and 35 °C, compared with published data under similar experiment conditions [174].

	Temperature (°C)	Stoichiometry (N)	K_B (M^{-1})	ΔH (kJ/mol)
Our results	23	1.01	~9.0×10^4	52.3
	35	1.07	~4.0×10^4	56
Published data	28	1.00	8.27×10^4	51.4
	38	1.04	4.85×10^4	57.5

6.4 Conclusions

This chapter presents a MEMS device combining sensitive thermoelectric sensing and on-chip microfluidic mixing for isothermal titration calorimetric characterization of biomolecular interactions. The MEMS device consists of a pair of PDMS microfluidic chambers (1 μL), each situated on a freestanding diaphragm and surrounded by air cavities for maximized thermal isolation. The chambers are each equipped with a thin-film resistive micro-temperature sensor and heater for *in-situ* temperature monitoring and device calibration, and are integrated with a thin-film Sb-Bi thermopile to detect the differential temperature between chambers. Each chamber is connected to the inlets through a passive chaotic micromixer which uses herringbone-shaped ridges in the ceiling of a serpentine channel to generate a chaotic flow pattern that enhances mixing of the incoming liquid streams. For ITC measurements, the sample and binding reagent introduced into the device are first mixed before they enter the reaction chamber, while the sample and pure buffer are introduced and mixed before entering the reference chamber. The differential temperature between the chambers is measured using the integrated thermopile, and is used to compute the bio-thermal power, and furthermore, the thermodynamic parameters of the interaction.

We first calibrated the MEMS-ITC device to determine its responsivity of 4.9 mV/mW and thermal time constant of approximately 1.5 s. The baseline stability and detection specificity were then validated using a standard reaction system of 18-C-6 and $BaCl_2$ compared with a control experiment in which 18-C-6 and sterile water were introduced. We then used the device to measure the reaction of 18-C-6 and $BaCl_2$ at varying molar ratio in a 1-μL volume at concentrations as low as 5 mM. With the temperature controlled at 23 and 35 °C, the bio-thermal power as s function of molar ratio from our ITC measurements was used to build binding isotherms from which consistent temperature-dependent thermodynamic properties of the biomolecular binding, including the stoichiometry, equilibrium binding constant, and enthalpy change, are obtained and found to agree with published results using commercial calorimeters. We further applied the MEMS-ITC device for a ligand-protein binding system of 2’CMP and RNase A for demonstration with a volume of 1 μL and concentrations as low as 2 mM. We again performed ITC measurements at 23 and 35 °C, obtaining consistent temperature-dependent thermodynamic properties that agreed well with published data. These results demonstrate the potential of this MEMS-ITC device for efficient characterization of biomolecular interactions with minimized sample consumption.

Chapter 7 Concluding Remarks

7.1 Thesis Summary

In this thesis, several MEMS-based devices integrating microfluidic handling, *in-situ* temperature control, and sensitive detection are presented for temperature-dependent characterization of biomolecular interactions within well-defined environments. These devices are aimed at different applications for surface-based and solution-based biomolecular interactions. For surface-based biomolecular interactions, microfluidic devices integrating on-chip micro-heaters and temperature sensors have been developed, either exploiting microcantilevers for temperature-dependent characterization of biomolecular affinity binding, or combining TIRF microscopy for investigation of the temperature dependence of biomolecular activity with single-molecule resolution. For solution-based interactions, MEMS-based calorimetric devices integrating effective thermal isolation, microfluidic chambers and on-chip passive mixing, sensitive thermoelectric sensing, and temperature scanning functionalities have been developed. These MEMS devices include DC- and AC-DSC sensors for probing the energetics of biomolecules through a range of temperature, as well as an ITC sensor for temperature-dependent characterization of biochemical reactions and molecular interactions. For all these MEMS-based approaches, temperature-dependent thermodynamic properties underlying various biomolecular interactions have also been determined from our systematic measurements.

Chapter 2 presents label-free characterization of temperature-dependent biomolecular affinity binding on solid surfaces using a microcantilever-based device integrating on-chip temperature sensing. The device consists of a Parylene cantilever one side of which is coated with a thin gold film and functionalized with molecules of an affinity receptor to a target analyte. The cantilever is located in a PDMS microfluidic chamber which is integrated with a transparent ITO thin-film resistive temperature sensor on a glass slide. The ITO sensor allows for real-time measurements of the temperature inside the chamber with unobstructed optical access for reflection-based optical detection of the cantilever deflection. To test the temperature-dependent binding between the target and receptor, the temperature of the chamber is maintained at a constant setpoint, while the analyte solution is continuously infused through the chamber. The measured cantilever deflection is used to determine the thermodynamic properties associated with the target-receptor binding according to a monovalent binding kinetic model. We studied the temperature-dependent affinity binding between PDGF and an affinity aptamer with the chamber temperature controlled in the range of 19-37 °C. Quantitative binding properties were obtained, indicating strong temperature dependence of the binding of PDGF to the aptamer.

In Chapter 3, a microfluidic approach to investigating the temperature-dependence of single-molecule activity is presented. The approach utilizes a temperature-controlled microfluidic flowcell coupled to a prism-based TIRF microscope. The temperature-controlled microfluidic flowcell consists of a set of parallel microchannels formed between a quartz slide and a glass coverslip on which thin-film micro-heaters, for efficient and rapid on-chip heating, and temperature sensors, for *in situ* temperature measurements within the microchannels, are integrated. Closed-loop, accurate temperature control is accomplished by a PID algorithm with the steady-state temperature maintained within approximately ±0.01 ˚C of the desired setpoints while achieving thermal stability within less than 30 s. The utility of our microfluidic approach has been demonstrated by its application to the characterization of the temperature dependence of smFRET *versus* time trajectories reporting on the GS1$\rightleftarrows$GS2 equilibrium within a PRE^{-A} ribosomal complex. Analysis of the smFRET *versus* time trajectories recorded as a function of temperature reveal that the GS1 and GS2 states of PRE complexes represent configurations of the PRE complex that are preferentially populated at the physiologically relevant temperature of 37 °C. In addition, analysis of the histograms of the dwell times spent in the GS1 or GS2 states prior to undergoing a transition plotted from the smFRET *versus* time trajectories recorded the various temperatures reveal that the frequencies of both GS1→GS2 and GS2→GS1 transitions increase as a function of increasing temperature.

Chapter 4 presents a MEMS DSC sensor combining sensitive thermoelectric sensing and effective thermal isolation for thermodynamic characterization of small quantities of liquid-phase biomolecular samples. The device consists of a pair of PDMS microfluidic chambers (volume: 1 μL), each situated on a freestanding polyimide diaphragm and surrounded by air cavities for thermal isolation. The calorimetric chambers are each integrated with a thin-film resistive gold temperature sensor and heater for temperature monitoring and on-chip calibration heating. The chambers are also integrated with a thin-film Sb-Bi thermopile whose hot and cold junctions are located at the centers of the chambers to measure the differential temperature between chambers. With their temperature scanned at a constant rate over a range of interest, the differential thermal power between the biomolecular sample and reference solution is measured via the thermopile voltage in real time and used to compute the thermodynamic properties. The MEMS DSC sensor was first calibrated to determine its responsivity (4 mV/mW) and thermal time constant (2.0 s). It was then used to measure the unfolding of lysozyme at detectable sample concentrations approaching 1 mg/mL. The partial specific heat capacity, the change of molar enthalpy, and the melting temperature were determined and found in agreement with reported values in literature. We also investigated the effects of choice of temperature scanning rate on DSC measurements using the device and observed that a temperature scanning rate as high as 5 ºC/min is adequate for the characterization of lysozyme unfolding.

As a variant of standard DSC, AC-DSC characterization of liquid biomolecules in a MEMS device is presented in Chapter 5. The device consists of two PDMS microfluidic calorimetric chambers each 1 μL in volume. The chambers are each surrounded by air gaps and based on a freestanding polyimide diaphragm, offering excellent thermal isolation. The diaphragms are integrated with resistive microheaters and temperature sensors as well as a 100-junction Sb-Bi thermopile for thermal control and sensing. The differential power between a sample and a reference material contained in the chambers is measured via the thermopile, while the chamber temperature is varied at a specified rate, with a periodic modulation component provided by the on-chip heaters. Characterization of the device yielded a DC responsivity of 8 mV/mW and a thermal time constant of approximately 2.0 s. The frequency response of the device indicated that optimal sensitivity could be obtained in a modulation frequency range of 0.5–20 Hz. Measurement of the unfolding of lysozyme at concentrations of 20 and 10 mg/mL using the device was performed at modulation frequencies of 1, 5, and 10 Hz. The specific heat capacity and the melting temperature during the unfolding process were calculated and found to agree with widely accepted data in the literature.

In Chapter 6, a MEMS device combining sensitive thermoelectric sensing and on-chip microfluidic mixing for ITC characterization of biomolecular interactions is presented. The MEMS device consists of a pair of PDMS microfluidic chambers (1 μL), each again situated on a freestanding diaphragm and surrounded by air cavities for maximized thermal isolation. The chambers are each equipped with a thin-film resistive micro-temperature sensor and heater, and are integrated with a thin-film Sb-Bi thermopile to detect the differential temperature between chambers. Each chamber is connected to the inlets through a passive chaotic micromixer which uses herringbone-shaped ridges in the ceiling of a serpentine channel to generate a chaotic flow pattern that enhances mixing of the incoming liquid streams. For ITC measurements, the sample and binding reagent introduced into the device are first mixed before they enter the reaction chamber, while the sample and pure buffer are introduced and mixed before entering the reference chamber. The differential temperature between the chambers is measured using the integrated thermopile, and is used to compute the bio-thermal power. We first calibrated the MEMS-ITC device to determine its responsivity of 4.9 mV/mW and thermal time constant of approximately 1.5 s. We then used the device to measure the reaction of 18-C-6 and $BaCl_2$ and a ligand-protein binding system of 2’CMP and RNase A at varying molar ratios in a 1-μL volume at concentrations as low as 2 mM with the temperature controlled at 23 and 35 °C. Temperature-dependent thermodynamic properties of the biomolecular binding, including the stoichiometry, equilibrium binding constant, and enthalpy change, are obtained and found to agree with published results using commercial calorimeters.

The techniques and devices presented in this thesis demonstrate the great potential of MEMS-based integrated microsystems for various temperature-dependent biomolecular characterization applications.

7.2 Future Work

The MEMS-based devices described in this thesis provide a robust framework for temperature-dependent characterization of biomolecular interactions within well-defined micro-environments. In addition to the future work discussed at the conclusion of each individual chapter, the following opportunities might be significant extensions to the work presented in this thesis.

7.2.1 Further Size Reduction of Sensors and Reactors

Miniaturization [194] has been a major feature of MEMS devices with significant advantages including minimized sample consumption, higher integration of functional units in a single device, lower cost, and enhanced portability. When applied for temperature-dependent characterization of biomolecular interactions, further reduction of device size is more important in that thermal response and heating efficiency can be improved due to reduced thermal mass. There have been several attempts of extreme size reduction for MEMS-based biomolecular characterization in literature. For example, MEMS calorimetric devices measuring droplet-based reactions with a volume of tens of nanoliters [186] or integrating isolated small microchambers (a few nanoliters) as bio-reactors [110]. The MEMS devices presented in this thesis are typically based on silicon or glass substrate with a typical chip size of approximately 1×1 cm^2, while the microfluidic channels or chambers typically have a volume of approximately 1 μL. These dimensions can be further reduced in future studies with proper addressing the accompanying issues such as fabrication yield, design of other elements (e.g., microheaters arrayed along channels) to maintain the same functions, and detection setup improvement.

7.2.2 Improvement of Thermal Isolation and Minimization of Noise

For thermal biosensors, the detection sensitivity and accuracy also strongly depend on the thermal isolation of the biomolecular interactions [152]. This actually requires additional experimental setup in biomolecular characterization applications. For example, many conventional calorimeters have to equip strict thermal shielding or even adiabatic environment [195] to meet certain detection requirements. In our MEMS-based calorimetry studies, we have noticed that the device responsivity is affected by the thermal isolation between the calorimetric chambers significantly. For example, using a typical MEMS DSC device with two 1-μL microchambers and a 50-junction Sb-Bi thermopile integrated, the thermoelectric sensitivity, i.e., the coefficient of the thermopile output voltage changes as a function of differential thermal power, was determined to be ~ 4 mV/mW with both chambers situated on freestanding diaphragms, while < 1 mV/mW with a 50-μm thick silicon residual layer underneath the diaphragms.

For maximized thermal isolation, our current MEMS calorimetric design features totally freestanding diaphragms with surrounding air cavities, as well as operating in a custom-built thermal enclosure providing shielding from the environmental disturbances.

To further improve the thermal isolation between the calorimetric chambers, both the device design and the thermal enclosure can be reconfigured in future studies. For device design, the structure such as the geometry of the thermopile, the supporting frame, and the diaphragm and chamber, can be modified. For example, the fabrication substrate can be another low-thermal conductivity material other than silicon. The two calorimetric chambers can be situated on a large diaphragm with miniaturized access channels such that both chambers can be extremely isolated. For thermal enclosure, more metal enclosures can be used while the inside can be vacuumed to provide enhanced thermal shielding.

The thermoelectric detection capability is also significantly limited by the background thermal noise in measurements. The major thermal noise, Johnson noise, is defined as $U_n = \sqrt{4k_B T \Delta f \cdot R}$, where k_B is the Boltzmann constant, T the temperature, Δf the measurement bandwidth, and R the electrical resistance of a thermal sensor. To reduce the Johnson noise of the thermal sensor, an effective method would be reducing the electrical resistance of the thermal sensor, i.e., the thermopile used in MEMS calorimeters. This goal can be achieved by optimizing the geometric parameters of the thermopile, such as the line width, length, and thickness, and the number of thermal junctions. In addition, configuration of the instruments and experimental setup to enable a lower measurement bandwidth can also reduce Johnson noise significantly. However, a lower bandwidth also induces a longer duration for data integration and hence a lower data acquisition rate.

7.2.3 High-Throughput Arrays

High throughput [194] has been another truly intriguing advantage using MEMS devices for biomolecular characterization [165]. As enable by MEMS design and fabrication, multiple functional elements can be simply integrated in a single device for parallel measurements. The work presented in this thesis holds great potential in improving the throughput along this scheme. For example, microcantileves are known to be fabricated in pairs for interferometric measurements or lined up in parallel microchannels such that multiple experiments can be performed simultaneously. In addition, the MEMS DSC and ITC devices can also be transplant to an array on which multiple sets of calorimetric chambers with micro-mixers and thermal sensors can be integrated again for characterization of many bio-samples efficiently. As such, these arrays can be potentially used as high-throughput drug screening platforms, and thus are very beneficial to both scientific investigations and healthcare. We should also be aware that many efforts are further needed to achieve such arrays. One prominent issue would be the liquid-phase sample introduction and control in which complicated microfluidic network and valving [196, 197] is required.

However, the future work listed above is representative, but not all-inclusive. The prospective MEMS devices for temperature-dependent characterization of biomolecular interactions are expected to have improved sensitivity, accuracy, faster thermal response, higher throughput, and enhanced reliability. Many novel features and functionalities may continuously emerge with the development of engineering techniques and the ceaseless pursuit of mankind in practicability, convenience, and comfort.

List of Publication Resulting From This Thesis

Refereed Journal Publications

1. Bin Wang, Yuan Jia, and Qiao Lin, "A MEMS isothermal titration biocalorimeter," in preparation.

2. Jingyi Fei, Bin Wang, Joseph Ho, Qiao Lin, Ruben L. Gonzalez, Jr., "Energy landscape of ribosomal pre-translocation complex revealed temperature-controlled single-molecule measurement," in preparation.

3. Bin Wang and Qiao Lin, "A MEMS differential scanning calorimetric sensor for thermodynamic characterization of biomolecules," *J. Microelectromechanical Systems*, in press.

4. Bin Wang and Qiao Lin, "Temperature-modulated differential scanning calorimetry in a MEMS device," *Sensors and Actuators: B: Chemical*, in press.

5. Bin Wang, Fengliang Huang, ThaiHuu Nguyen, Yong Xu, and Qiao Lin, "Microcantilever-based label-free characterization of temperature-dependent biomolecular affinity binding," *Sensors and Actuators: B: Chemical*, in press.

6. Bin Wang, Joseph Ho, Jingyi Fei, Ruben L. Gonzalez, Jr., and Qiao Lin, "A microfluidic approach for investigating the temperature dependence of biomolecular activity with single-molecule resolution," *Lab on a Chip*, 11: 274-281, 2011.

7. Li Wang, Bin Wang, and Qiao Lin, "Demonstration of MEMS-based differential scanning calorimetry for determining thermodynamic properties of biomolecules," *Sensors and Actuators B: Chemical*, 134: 953-958, 2008.

Refereed Conference Publications

1. Bin Wang, Yuan Jia, and Qiao Lin, "A MEMS isothermal titration biocalorimeter," *The 16th Int. Conf. Miniaturized Systems for Chemistry and Life Sciences (MicroTAS' 12)*, Okinawa, Japan, 2012, accepted.

2. Bin Wang and Qiao Lin, "MEMS-based AC differential scanning calorimetry," *The 16th Int. Conf. Solid-State Sensors, Actuators and Microsystems (Transducers' 11)*, pp. 1958-1961, Beijing, China, 2011.

3. Bin Wang and Qiao Lin, "A MEMS differential scanning calorimeter for thermodynamic characterization of biomolecules," *IEEE Int. Conf. Micro Electro Mechanical Systems (MEMS' 11)*, pp. 821-824, Cancun, Mexico, 2011.

4. Bin Wang, ThaiHuu Nguyen, Fengliang Huang, and Qiao Lin, "Microcantilever-based label-free thermal characterization of biomolecular affinity binding," *IEEE Int. Conf. Micro Electro Mechanical Systems (MEMS' 10),* pp. 855-858, Hong Kong, China, 2010.

5. Bin Wang, Jingyi Fei, ThaiHuu Nguyen, Ruben L. Gonzalez, Jr., and Qiao Lin, "Translocation of the ribosome in temperature-controlled microfluidic channels," *Int. Conf. on Miniaturized Chemical and Biochemical Analysis Systems (MicroTAS' 07)*, pp. 796-798, Paris, France, 2007.

6. Bin Wang, Jingyi Fei, ThaiHuu Nguyen, Ruben L. Gonzalez, Jr., and Qiao Lin, "Single-molecule detection in temperature-controlled microchannels," *IEEE Int. Conf. Nano/Micro Engineered and Molecular Systems (NEMS' 07),* pp. 972-976, Bangkok, Thailand, 2007.

Bibliography

[1] A. J. Hopfinger, *Intermolecular Interactions and Biomolecular Organization*: John Wiley & Sons Inc, 1977.

[2] T. Nguyen, J. P. Hilton, and Q. Lin, "Emerging applications of aptamers to micro- and nanoscale biosensing," *Microfluidics and Nanofluidics,* vol. 6, pp. 347-362, 2009.

[3] H.-J. Bohm and G. Schneider, *Protein-ligand interactions: from molecular recognition to drug design*: Wiley, 2003.

[4] A. Velazquez-Campoy, M. J. Todd, and E. Freire, "HIV-1 protease inhibitors: enthalpic versus entropic optimization of the binding affinity," *Biochemistry,* vol. 39, pp. 2201-2207, 2000.

[5] S. C. Blanchard, H. D. Kim, J. Ruben L. Gonzalez, J. D. Puglisi, and S. Chu, "tRNA dynamics on the ribosome during translation," *PNAS,* vol. 101, pp. 12893-12898, 2004.

[6] J. Frank and J. Ruben L. Gonzalez, "Dynamics of the ribosome during the elongation cycle," *Annual Review of Biochemistry,* vol. 79, p. in press, 2010.

[7] P. D'Orazio, "Biosensors in clinical chemistry," *Clinica Chimica Acta,* vol. 334, pp. 41-69, 2003.

[8] V. R. Meyer, *Practical High-Performance Liquid Chromatography*: Wiley, 2010.

[9] T. W. Mayhood and W. T. Windsor, "Ligand binding affinity determined by temperature-dependent circular dichroism: Cyclin-dependent kinase 2 inhibitors," *Analytical Chemistry,* vol. 345, pp. 187-197, 2005.

[10] G. K. Shoemaker, N. Soya, M. M. Palcic, and J. S. Klassen, "Temperature-dependent cooperativity in donor-acceptor substrate binding to the human blood group glycosyltransferases," *Glycobiology,* vol. 18, pp. 587-592, 2008.

[11] T. Nguyen, R. Pei, M. Stojanovic, and Q. Lin, "An aptamer-based microfluidic device for thermally controlled affinity extraction," *Microfluidics and Nanofluidics,* vol. 6, pp. 479-487, 2009.

[12] L. Brunton, J. Lazo, and K. Parker, *Goodman and Gilman's The Pharmacological Basis of Therapeutics*, 11th ed.: McGraw-Hill Professional, 2005.

[13] B.-R. Laboratories. Available: http://www3.bio-rad.com/

[14] P. Bergese, G. Oliviero, I. Alessandri, and L. E. Depero, "Thermodynamics of mechanical transduction of surface confined receptor/ligand reactions," *Journal of Colloid and Interface Science,* vol. 316, pp. 1017-1022, 2007.

[15] J. LaBaer and N. Ramachandran, "Protein microarrays as tools for functional proteomics," *Current Opinion in Chemical Biology,* vol. 9, pp. 14-19, 2005.

[16] P. Angenendt, J. Glokler, Z. Konthur, H. Lehrach, and D. J. Cahill, "3D protein microarrays: performing multiplex immunoassays on a single chip," *Analytical Chemistry,* vol. 75, pp. 4368-4372, 2003.

[17] P. Cimmperman, L. Baranauskiene, S. Jachimoviciute, J. Jachno, J. Torresan, V. Michailoviene, J. Matuliene, J. Sereikaite, V. Bumelis, and D. Matulis, "A quantitative model of thermal stabilization and destabilization of proteins by ligands," *Biophysical Journal,* vol. 95, pp. 3222-3231, 2008.

[18] R. Karlsson and R. Stahlberg, "Surface plasmon resonance detection and multispot sensing for direct monitoring of interactions involving low-molecular-weight analytes and for determination of low affinities," *Analytical Biochemistry,* vol. 228, pp. 274-280, 1995.

[19] P. D. Skottrup, M. Nicolaisen, and A. F. Justesen, "Towards on-site pathogen detection using antibody-based sensors," *Biosensors and Bioelectronics,* vol. 24, pp. 339-348, 2008.

[20] L. S. Green, D. Jellinek, R. Jenison, A. Ostman, C.-H. Heldin, and N. Janjic, "Inhibitory DNA ligands to platelet-derived growth factor B-chain," *Biochemistry,* vol. 35, pp. 14413-14424, 1996.

[21] T. K. Dam, R. Roy, D. Page, and C. F. Brewer, "Negative cooperativity associated with binding of multivalent carbohydrates to lectins. Thermodynamic analysis of the "multivalency effect"," *Biochemistry,* vol. 41, pp. 1351-1358, 2002.

[22] C. L. Danvic, G. Guiraudie-Capraz, D. Abderranhmani, J.-P. Zanetta, and P. N.-L. Meillour, "Natural ligands of porcine olfactory binding proteins," *Journal of Chemical Ecology,* vol. 35, pp. 741-751, 2009.

[23] W.-L. Tseng, H.-T. Chang, S.-M. Hsu, R.-J. Chen, and S. Lin, "Immunoaffinity capillary electrophoresis: determination of binding constant and stoichiometry for antibody-antigen interaction," *Electrophoresis,* vol. 23, pp. 836-846, 2002.

[24] S. Balamurugan, A. Obubuafo, S. A. Soper, and D. A. Spivak, "Surface immobilization methods for aptamer diagnostic applications," *Analytical and Bioanalytical Chemistry,* vol. 390, pp. 1009-1021, 2008.

[25] T. H. D. J. Patel, "Adaptive recognition by nucleic acid aptamers," *Science,* vol. 287, pp. 820-825, 2000.

[26] C. Tuerk and L. Gold, "Systematic evolution of ligands by exponential enrichment: RNA ligands to bacteriophage T4 DNA polymerase," *Science,* vol. 249, pp. 505-510, 1990.

[27] S. Cho, S. H. Lee, W. J. Chung, Y. K. Kim, Y. S. Lee, and B. G. Kim, "Mcirobead-based affinity chromatography chip using RNA aptamer modified with photocleavable linker," *Electrophoresis,* vol. 25, pp. 3730-3739, 2004.

[28] S. Jayasena, "Aptamers: an emerging class of molecules that rival antibodies in diagnostics," *Clinical Chemistry,* vol. 45, pp. 1628-1650, 1999.

[29] B. B. Haab, "Methods and applications of antibody microarrays in cancer research," *Proteomics,* vol. 3, pp. 2116-2122, 2003.

[30] U. B. Nielsen, M. H. Cardone, A. J. Sinskey, G. MacBeath, and P. K. Sorger, "Profiling receptor tyrosine kinase activation by using Ab mciroarray," *PNAS,* vol. 100, pp. 9330-9335, 2003.

[31] M. W. Pantoliano, E. C. Petrella, J. D. Kwasnoski, V. S. Lobanov, J. Myslik, E. Graf, T. Carver, E. Asel, B. A. Springer, P. Lane, and F. R. Salemme, "High-

density miniaturization thermal shift assays as a general strategy for drug discovery," *Journal of Biomolecular Screening,* vol. 6, pp. 429-440, 2001.

[32] M. A. Cooper and V. T. Singleton, "A survey of the 2001 to 2005 quartz crystal microbalance biosensor literature: applications of acoustic physics to the analysis of biomolecular interactions," *Journal of Molecular Recognition,* vol. 20, pp. 154-184, 2007.

[33] P. S. Waggoner and H. G. Craighead, "Micro- and nanomechanical sensors for environmental, chemical, and biological detection," *Lab on a Chip,* vol. 7, pp. 1238-1255, 2007.

[34] A. M. v. Oijen, "Single-molecule approaches to characterization kinetics of biomolecular interactions," *Current Opinion in Biotechnology,* vol. 22, pp. 75-80, 2011.

[35] S. C. Blanchard, J. Ruben L. Gonzalez, H. D. Kim, S. Chu, and J. D. Puglisi, "tRNA selection and kinetic proofreading in translation," *Nature Structural and Molecular Biology,* vol. 11, pp. 1008-1014, 2004.

[36] J. Fei, J. E. Bronson, J. M. Hofman, R. L. Srinivas, C. H. Wiggins, and J. Ruben L. Gonzalez, "Allosteric collaboration between elongation factor G and the ribosomal L1 stalk directs tRNA movements during translation," *PNAS,* vol. 106, pp. 15702-15707, 2009.

[37] J. Fei, J. Wang, S. H. Sternberg, D. D. MacDougall, M. M. Elvekrog, D. K. Pulukkunat, M. T. Englander, and J. Ruben L. Gonzalez, "A highly purified, fluorescently labeled in vitro translation system for single-molecule studies of protein synthesis," *Methods in Enzymology,* vol. 472, pp. 221-259, 2010.

[38] G. J. Schutz, W. Trabesinger, and T. Schmidt, "Direct observation of ligand colocalization on individual receptor molecules," *Biophysical Journal,* vol. 74, pp. 2223-2226, 1998.

[39] L. Edman and R. Rigler, "Memory landscapes of single-enzyme molecules," *PNAS,* vol. 97, pp. 8266-8271, 2000.

[40] B. P. English, W. Min, A. M. v. Oijen, K. T. Lee, G. Luo, H. Sun, B. J. Cherayil, S. C. Kou, and X. S. Xie, "Ever-fluctuating single enzyme molecules: Michaelis-Menten equation revisited," *Nature Chemical Biology,* vol. 2, pp. 87-94, 2006.

[41] O. Flomenbom, K. Velonia, D. Loos, S. Masuo, M. Cotlet, Y. Engelborghs, J. Hofkens, A. E. Rowan, R. J. Nolte, and M. v. d. Auweraer, "Stretched exponential decay and correlations in the catalytic activity of fluctuating single lipase molecules," *PNAS,* vol. 102, pp. 2368-2372, 2005.

[42] A. D. Mehta, M. Rief, J. A. Spudich, D. A. Smith, and R. M. Simmons, "Single-molecule biomechanics with optical methods," *Science,* vol. 283, pp. 1689-1695, 1999.

[43] T. Funatsu, Y. Harada, M. Tokunaga, K. Saito, and T. Yanagida, "Imaging of single fluorescent molecules and individual ATP turnovers by single myosin molecules in aqueous solution," *Nature,* vol. 374, pp. 555-559, 1995.

[44] A. Borgia, P. M. Williams, and J. Clarke, "Single-molecule studies of protein folding," *Annual Review of Biochemistry,* vol. 77, pp. 101-125, 2008.

[45] W. J. Greenleaf, M. T. Woodside, and S. M. Block, "High-resolution, single-molecule measurements of biomolecular motion," *Annual Review of Biophysics and Biomolecular Structure,* vol. 36, pp. 171-190, 2007.

[46] C. Joo, H. Balci, Y. Ishitsuka, C. Buranachai, and T. Ha, "Advances in single-molecule fluorescence methods for molecular biology," *Annual Review of Biochemistry,* vol. 77, pp. 51-76, 2008.

[47] R. A. Marshall, C. E. Aitken, M. Dorywalska, and j. D. Puglisi, "Translation at the single-molecule level," *Annual Review of Biochemistry,* vol. 77, pp. 177-203, 2008.

[48] E. Toprak and P. R. Selvin, "Watching nanometer-scale conformational changes of single molecules," *Annual Review of Biophysics and Biomolecular Structure,* vol. 36, pp. 349-369, 2007.

[49] X. S. Xie, P. J. Choi, G.-W. Li, N. K. Lee, and G. Lia, "Single-molecule approach to molecular biology in living bacterial cells," *Annual Review of Biophysics and Biomolecular Structure,* vol. 37, pp. 417-444, 2008.

[50] X. Zhuang, "Single-molecule RNA science," *Annual Review of Biophysics and Biomolecular Structure,* vol. 34, pp. 399-414, 2005.

[51] V. V. Plotnikov, J. M. Brandts, L.-N. Lin, and J. F. Brandts, "A new ultrasensitive scanning calorimeter," *Analytical Biochemistry,* vol. 250, pp. 237-244, 1997.

[52] G. Privalov, V. Kavina, E. Freire, and P. L. Privalov, "Precise scanning calorimeter for studying thermal properties of biological macromolecules in dilute solution," *Analytical Biochemistry,* vol. 232, pp. 79-85, 1995.

[53] P. Privalov and S. Potekhin, "Scanning microcalorimetry in studying temperature-induced changes in proteins," *Methods in Enzymology,* vol. 131, pp. 4-51, 1986.

[54] C. A. Savran, S. M. Knudsen, A. D. Ellington, and S. R. Manalis, "Micromechanical detection of proteins using aptamer-based receptor molecules," *Analytica Chemistry,* vol. 76, pp. 3194-3198, 2004.

[55] G. D. Crescenzo, P. L. Pham, Y. Duracher, and M. D. O'Conner-McCourt, "Transforming growth factor-beta (TGF-beta) binding to the extracellular domain of the type II TGF-beta receptor: receptor capture on a biosensor surface using a new coiled-coil capture system demonstrates that avidity contributes significantly to high affinity binding," *Journal of Molecular Biology,* vol. 328, pp. 1173-1183, 2003.

[56] A. D. Robertson and K. P. Murphy, "Protein structure and the energetics of protein stability," *Chemical Reviews,* vol. 97, pp. 1251-1267, 1997.

[57] G. W. H. Hohne, W. F. Hemminger, and H.-J. Flammersheim, *Differential scanning calorimetry*, 2nd ed.: Springer Berlin / Heidelberg, 2004.

[58] T. Hatakeyama and F. X. Quinn, *Thermal Analysis: Fundamentals and Applications to Polymer Science*, 2nd ed.: Wiley New York, 1999.

[59] G. P. Privalov and P. L. Privalov, "Problems and prospects in microcalorimetry of biological macromolecules," *Energetics of Biological Macromolecules,* vol. 323, pp. 31-62, 2000.

[60] J. F. Brandts and L.-N. Lin, "Study of strong to ultratight protein interactions using differential scanning calorimetry," *Biochemistry,* vol. 29, pp. 6927-6940, 1990.

[61] E. Freire, G. Privalov, P. Privalov, and V. Kavina, "Device and methods for the heat of reaction resulting from mixture of a plurality of reagents," 5707149, 1998.

[62] T. Wiseman, S. Williston, J. F. Brandts, and L.-N. Lin, "Rapid measurement of binding constants and heats of binding using a new titration calorimeter," *Analytical Biochemistry,* vol. 179, pp. 131-137, 1989.

[63] R. Ghai, R. J. Falconer, and B. M. Collins, "Applications of isothermal titration calorimetry in pure and applied research--survey of the literature from 2010," *Journal of Molecular Recognition,* vol. 25, pp. 32-52, 2012.

[64] U. v. Ah, D. Wirz, and A. Daniels, "Isothermal micro calorimetry - a new method for MIC determination: results for 12 antibotics and reference strains of E. coli and S. aureus," *BMC Microbiology,* vol. 9, p. 106, 2009.

[65] A. L. Feig, "Review: applications of isothermal titration calorimetry in RNA biochemistry and biophysics," *Biopolymers,* vol. 87, pp. 293-301, 2007.

[66] T. G. A. Lonhienne and D. J. Winzor, "A potential role for isothermal calorimetry in studies of the effects of thermodynamic non-ideality in enzyme-catalyzed reactions," *Journal of Molecular Recognition,* vol. 17, pp. 351-361, 2004.

[67] J. E. Ladbury, "Isothermal titration calorimetry: application to structure-based drug design," *Thermochimica Acta,* vol. 380, pp. 209-215, 2001.

[68] M. A. A. O'Neill and S. Gaisford, "Applications and use of isothermal calorimetry in pharmaceutical development," *International Journal of Pharmaceutics,* vol. 417, pp. 83-93, 2011.

[69] L. S. Roselin, M.-S. Lin, P.-H. Lin, Y. Chang, and W.-Y. Chen, "Recent trends and some applications of isothermal titration calorimetry in biotechnology," *Biotechnology Journal,* vol. 5, pp. 85-98, 2010.

[70] J. Li and E. S. Yeung, "Real-time single-molecule kinetics of trypsin proteolysis," *Analytical Chemistry,* vol. 80, pp. 8509-8513, 2008.

[71] Y. Yang, F.-C. Lin, and G. Yang, "Temperature control device for single molecule measurements using the atomic force microscope," *Review of Scientific Instruments,* vol. 77, p. 063701, 2006.

[72] S. L. Biswal, D. Raorane, A. Chaiken, H. Birecki, and A. Majumdar, "Nanomechanical detection of DNA melting on microcantilever surfaces," *Analytical Chemistry,* vol. 78, pp. 7104-7109, 2006.

[73] D. Nettels, S. Muller-Spath, F. Kuster, H. Hofmann, D. Haenni, S. Ruegger, L. Reymond, A. Hoffmann, J. Kubelka, B. Heinz, K. Gast, R. B. Best, and B. Schuler, "Single-molecule spectroscopy of the temperature-induced collapse of unfolding proteins," *PNAS,* vol. 106, pp. 20740-20745, 2009.

[74] S. Enoki, R. Watanabe, R. Lino, and H. Noji, "Single-molecule study on the temperature-sensitive reaction of F1-ATPase with a Hybrid F1 carrying a single β(E190D)," *The Journal of Biological Chemistry,* vol. 284, pp. 23169-23176, 2009.

[75] M. Sekiya, R. K. Nakamoto, M. K. Al-Shawi, M. Nakanishi-Matsui, and M. Futai, "Temperature dependence of single molecule rotation of the Escherichia coli ATP synthase F1 sector reveals the importance of α–β subunit interactions in the catalytic dwell," *The Journal of Biological Chemistry,* vol. 284, pp. 22401-22410, 2009.

[76] P. S. Dittrich and A. Manz, "Single-molecule fluorescence detection in microfluidic channels- the holy grail in uTAS?," *Analytical and Bioanalytical Chemistry,* vol. 382, pp. 1771-1782, 2005.

[77] H.-F. Ji, H. Gao, K. R. Buchapudi, X. Yang, X. Xu, and M. K. Schulte, "Microcantilever biosensors based on conformational change of proteins," *The Analyst,* vol. 133, pp. 434-443, 2008.

[78] A.-R. A. Khaled, K. Vafai, M. Yang, X. Zhang, and C. S. Ozkan, "Analysis, control and augmentation of microcantilever deflections in bio-sensing systems," *Sensors and Actuators B: Chemical,* vol. 94, pp. 103-115, 2003.

[79] P. W. Snyder, G. Lee, P. E. Marszalek, R. L. Clark, and E. J. Toone, "A stochastic, cantilever approach to the evaluation of solution phase thermodynamic quantities," *PNAS,* vol. 104, pp. 2579-2584, 2007.

[80] T. Braun, M. K. Ghatkesar, N. Backmann, W. Grange, P. Boulanger, L. Letellier, H.-P. Lang, A. Bietsch, C. Gerber, and M. Hegner, "Quantitiative time-resolved measurement of membrane protein-ligand interactions using microcantilever array sensors," *Nature Nanotechnology,* vol. 4, pp. 179-185, 2009.

[81] M. Yue, J. C. Stachowiak, H. Lin, R. Datar, R. Cote, and A. Majumdar, "Label-free protein recognition two-dimensional array using nanomechanical sensors," *Nanoletters,* vol. 8, pp. 520-524, 2008.

[82] R. Mukhopadhyay, V. V. Sumbayev, M. Lorentzen, J. Kjems, P. A. Andreasen, and F. Besenbacher, "Cantilever sensor for nanomechanical detection of specific protein conformations," *Nanoletters,* vol. 5, pp. 2385-2388, 2005.

[83] M. B. Viani, L. I. Pietrasanta, J. B. Thompson, A. Chand, I. C. Gebeshuber, J. H. Kindt, M. Richter, H. G. Hansma, and P. K. Hansma, "Probing protein-protein interactions in real time," *Nature Structural Biology,* vol. 7, pp. 644-647, 2000.

[84] F. Huber, M. Hegner, C. Gerber, H.-J. Guntherodt, and H. P. Lang, "Label free analysis of transcription factors using microcantilevers arrays," *Biosensors and Bioelectronics,* vol. 21, pp. 1599-1605, 2006.

[85] N. C. H. Le, R. Yokokawa, D. V. Dao, T. D. Nguyen, J. C. Wells, and S. Sugiyama, "Versatile microfluidic total internal reflection (TIR)-based devices: application to microbeads velocity measurement and single molecule detection with upright and inverted microscope " *Lab on a Chip,* vol. 9, pp. 244-250, 2009.

[86] C. W. Hollars, J. Puls, O. Bakajin, B. Olsan, C. E. Talley, S. M. Lane, and T. Huser, "Bio-assay based on single molecule fluorescence detection in microfluidic channels," *Analytical and Bioanalytical Chemistry,* vol. 385, pp. 1384-1388, 2006.

[87] B. Ladoux, J.-P. Quivy, P. Doyle, O. d. Roure, G. Almouzni, and J.-L. Viovy, "Fast kinetics of chromatin assembly revealed by single-molecule videomicroscopy and scanning force microscopy," *PNAS,* vol. 97, pp. 14251-14256, 2000.

[88] M. Foquet, J. Korlach, W. Zipfel, W. W. Webb, and H. G. Craighead, "DNA fragment sizing by single molecule detection in submicrometer-sized closed fluidic channels," *Analytical Chemistry,* vol. 74, pp. 1415-1422, 2002.

[89] T.-H. Wang, Y. Peng, C. Zhang, P. K. Wong, and C.-M. Ho, "Single-molecule tracing on a fluidic microchip for quantitative detection of low-abundance nucleic acids," *Journal of the American Chemical Society,* vol. 127, pp. 5354-5359, 2005.

[90] T. Matsugna, M. Hosokawa, A. Arakaki, T. Taguchi, T. Mori, T. Tanaka, and H. Takeyama, "High-efficiency single-cell entrapment and fluorescence in situ hybridization analysis using a Poly(dimethylsiloxane) microfluidic device integrated with a black Poly(ethylene terephthalate) micromesh," *Analytical Chemistry,* vol. 80, pp. 5139-5145, 2008.

[91] V. Namasivayam, R. G. Larson, D. T. Burke, and M. A. Burns, "Electrostretching DNA molecules using polymer-enhanced media within microfabricated devices," *Analytical Chemistry,* vol. 74, pp. 3378-3385, 2002.

[92] S. L. Lai, G. Ramanath, and L. H. Allen, "High-speed scanning microcalorimetry with monolayer sensitivity," *Applied Physics Letters,* vol. 67, pp. 1229-1231, 1995.

[93] D. Jaeggi, H. Baltes, and D. Moser, "Thermoelectric AC power sensor by CMOS technology," *IEEE Electron Device Letters,* vol. 13, pp. 366-368, 1992.

[94] C. Hagleitner, A. Hierlemann, D. Lange, A. Kummer, N. Kerness, O. Brand, and H. Baltes, "Smart single-chip gas sensor microsystem," *Nature,* vol. 414, pp. 293-296, 2001.

[95] R. E. Cavicchi, G. E. Poirier, N. H. Tea, M. Afridi, D. Berning, A. Hefner, I. Suehle, M. Gaitan, S. Semancik, and C. Montgomery, "Micro-differential scanning calorimeter for combustible gas sensing," *Sensors and Actuators B,* vol. 97, pp. 22-30, 2004.

[96] J. R. Barnes, R. J. Stephenson, C. N. Woodburn, S. J. O'Shea, M. E. Wellan, T. Rayment, J. K.Gimzewski, and C. Gerber, "A femtojoule calorimeter using micromechanical sensors," *Review of Scientific Instruments,* vol. 65, pp. 3793-3798, 1994.

[97] E. A. Johannessen, J. M. R. Weaver, P. H. Cobboid, and J. M. Cooper, "Heat conduction nanocalorimeter for pl-scale single cell measurement," *Applied Physics Letters,* vol. 80, pp. 2029-2031, 2002.

[98] K. Verhaegen, K. Baert, J. Simaels, and W. van Dressche, "A high-throughput silicon microphysiometer," *Sensors and Actuators A,* vol. 82, pp. 186-190, 2000.

[99] E. B. Chancellor, J. P. Wikswo, F. Baudenbacher, M. Radparvar, and D. Osterman, "Heat conduction calorimeter for massively parrallel high throughput

measurements with picoliter sample volumes," *Applied Physics Letters,* vol. 85, pp. 2408-2411, 2004.

[100] E. A. Olson, M. Y. Efremov, A. T. Kwan, S. Lai, V. Petrova, F. Schiettekatte, J. T. Warren, M. Zhang, and L. H. Allen, "Scanning calorimeter for nanoliter-scale liquid samples," *Applied Physics Letters,* vol. 77, pp. 2671-2673, 2000.

[101] D. W. Cooke, K. J. Michel, and F. Hellman, "Thermodynamic measurements of submilligram bulk samples using a membrane-based "calorimeter on a chip"," *Review of Scientific Instruments,* vol. 79, p. 053902, 2008.

[102] S. Maggiolino, N. Scuor, R. L. Mahajan, and O. Sbaizero, "MEMS DSC: a new device for microcalorimetric analysis in the biological field," *Microsystem Technologies,* vol. 16, pp. 967-971, 2010.

[103] J. Lerchner, T. Maskow, and G. Wolf, "Chip calorimetry and its use for biochemical and cell biological investigations," *Chemical Engineering and Processing,* vol. 47, pp. 991-999, 2008.

[104] Y. Zhang and S. Tadigadapa, "Calorimetric biosensor with integrated microfluidic channels," *Biosensors and Bioelectronics,* vol. 19, pp. 1733-1743, 2004.

[105] C. Pradere, C. Hany, J. Toutain, and J.-C. Batsale, "Thermal analysis for velocity, kinetics, and enthalpy reaction measurements in microfluidic devices," *Experimental Heat Transfer,* vol. 23, pp. 44-62, 2010.

[106] N. Inomata, M. Toda, M. Sato, A. Ishijima, and T. Ono, "Pico calorimeter for detection of heat produced in an individual brown fat cell," *Applied Physics Letters,* vol. 100, p. 154104, 2012.

[107] G. V. Casquillas, F. Bertholle, M. L. Berre, S. Meance, L. Malaquin, J. J. Greffet, and Y. Chen, "Thermo-resistance based micro-calorimeter for continuous chemical enthalpy measurements," *Microelectronic Engineering,* vol. 85, pp. 1367-1369, 2008.

[108] B. S. Kwak, B. S. Kim, H. H. Cho, J. S. Park, and H. I. Jung, "Dual thermopile intergated microfluidic calorimeter for biochemical thermodynamics," *Microfluidics and Nanofluidics,* vol. 5, pp. 255-262, 2008.

[109] B. S. Kwak, B. S. Kim, H. H. Cho, J. S. Park, and H. I. Jung, "Dual thermopile integrated microfluidic calorimeter for biochemical thermodynamics," *Microfluidics and Nanofluidics,* vol. 5, pp. 255-262, 2008.

[110] W. Lee, W. Fon, B. W. Axelord, and M. L. Roukes, "High-sensitivity microfluidic calorimeters for biological and chemical applications," *PNAS,* vol. 106, pp. 15225-15230, 2009.

[111] M. I. Recht, D. D. Bruyker, A. G. Bell, M. V. Wolkin, E. Peeters, G. B. Anderson, A. R. Kolatkar, M. W. Bern, P. Kuhn, R. H. Bruce, and F. E. Torres, "Enthalpy array analysis of enzymatic and binding reactions," *Analytical Biochemistry,* vol. 377, pp. 33-39, 2008.

[112] V. Vandelinder, A. C. M. Ferreon, Y. Gambin, A. A. Deniz, and A. Groisman, "High-resolution temperature-concentration diagram of a-synuclein conformation obtained from a single Forster resonance energy transfer image in a microfluidic device," *Analytical Chemistry,* vol. 81, pp. 6929-6935, 2009.

[113] P. R. N. Childs, *Practical temperature measurement*: Butterworth-Heinemann, 2001.

[114] H. F. Arata, Y. Rondelez, H. Noji, and H. Fujita, "Temperature alternation by an on-chip microheater to reveal enzymatic activity of b-galactosidase at high temperatures," *Analytical Chemistry,* vol. 77, pp. 4810-4814, 2005.

[115] D. A. Raorane, M. D. Lim, F. F. Chen, C. S. Craik, and A. Majumdar, "Quantitative and label-free technique for measuring protease activity and inhibition using a microfluidic cantilever array," *Nanoletters,* vol. 8, pp. 2968-2974, 2008.

[116] S. S. Sinha, R. K. Mitra, and S. K. Pal, "Temperature-dependent simultaneous ligand binding in human serum albumin," *Journal of Physical Chemistry B,* vol. 112, pp. 4884-4891, 2008.

[117] B. Wang, J. Ho, J. Fei, R. L. G. Jr., and Q. Lin, "A microfluidic approach for investigating the temperature dependence of biomolecular activity with single-molecular resolution," *Lab on a Chip,* vol. 11, pp. 274-281, 2011.

[118] G. A. Richardson, "Autonomous thermal control system for highly variable environments," *Journal of Heat Transfer,* vol. 131, p. 064505 (3 pages), 2009.

[119] B. Yang and Q. Lin, "Planar Micro Check Valves Based on Polymer Compliance," *Sensors and Actuators A: Physical,* vol. 134, pp. 186-193, 2007.

[120] R. W. Glaser, "Antigen-antibody binding and mass transport by convection and diffusion to a surface: a two-dimensional computer model of binding and dissociation kinetics," *Analytical Biochemistry,* vol. 213, pp. 152-161, 1993.

[121] J. Liu, N. J. Agrawal, A. Calderon, P. S. Ayyaswamy, D. M. Eckmann, and R. Radhakrishnan, "Multivalent binding of nanocarrier to endothelial cells under shear flow," *Biophysical Journal,* vol. 101, pp. 319-326, 2011.

[122] G. D. Crescenzo, C. Boucher, Y. Durocher, and M. Jolicoeur, "Kinetic characterization by surface plasmon resonance-based biosensors: principle and emerging trends," *Cellular and Molecular Bioengineering,* vol. 1, pp. 204-215, 2008.

[123] G. Prism. Available: www.graphpad.com/prism/prism.htm/

[124] G. Carta and A. Jungbauer, *Protein Chromatography: Process Development and Scale-Up*: Wiley-VCH, 2010.

[125] R. A. Potyrailo, R. C. Conrad, A. D. Ellington, and G. M. Hieftje, "Adapting selected nucleic acid ligands (aptamers) to biosensors," *Analytica Chemistry,* vol. 70, pp. 3419-3425, 1998.

[126] M. Gavutis, E. Jacks, P. Lamken, and J. Piehler, "Determination of the two-dimensional interaction rate constants of a cytokine receptor complex," *Biophysical Journal,* vol. 90, pp. 3345-3355, 2006.

[127] C. B. Muller and W. Richtering, "Sealed and temperature-controlled sample cell for inverted and confocal microscopes and fluorescence correlation spectroscopy," *Colloid and Polymer Science,* vol. 286, pp. 1215-1222, 2008.

[128] Y. Yang, F.-C. Lin, and G. Yang, "Temperature control device for single molecule measurements using the atomic force microscope," *Review of Scientific Instruments,* vol. 77, p. 063701, 2006.

[129] E. T. Lagally, I. Medintz, and R. A. Mathies, "Single-molecule DNA amplification and analysis in an integrated microfluidic device," *Analytical Chemistry,* vol. 73, pp. 565-570, 2001.

[130] P. V. Cornish and T. Ha, "A survey of single-molecule techniques in chemical biology," *ACS Chemical Biology,* vol. 2, pp. 53-61, 2007.

[131] J. Fei, P. Kosuri, D. D. MacDougall, and J. Ruben L. Gonzalez, "Coupling of ribosomal L1 stalk and tRNA dynamics during translation elongation," *Molecular Cell,* vol. 30, pp. 348-359, 2008.

[132] R. Roy, S. Hohng, and T. Ha, "A practical guide to single-molecule FRET," *Nature Methods,* vol. 5, pp. 507-516, 2008.

[133] S. Dorner, J. L. Brunelle, D. Sharma, and R. Green, "The hybrid state of tRNA binding is an authentic translation elongation intermediate," *Nature Structural & Molecular Biology,* vol. 13, pp. 234-241, 2006.

[134] L. H. Horan and H. F. Noller, "Intersubunit movement is required for ribosomal translocation," *PNAS,* vol. 104, pp. 4881-4885, 2007.

[135] T. Ha, I. Rasnik, W. Cheng, H. P. Babcock, G. H. Gauss, T. M. Lohman, and S. Chu, "Initiation and re-initiation of DNA unwinding by the Escherichia coli Rep helicase," *Nature,* vol. 419, pp. 638-641, 2002.

[136] Q. Lin, F. Jiang, X.-Q. Wang, Y. Xu, Z. Han, Y.-C. Tai, J. Lew, and C.-M. Ho, "Experiments and simulations of MEMS thermal sensors for wall shear-stress measurements in aerodynamic control applications," *Journal of Micromechanics and Microengineering,* vol. 14, pp. 1640-1649, 2004.

[137] R. J. Goldstein and K.-S. Lau, "Laminar natural convection from a horizontal plate and the influence of plate-edge extensions," *Journal of Fluid Mechanics,* vol. 129, pp. 55-75, 1983.

[138] N. Fischer, A. L. Konevega, W. Wintermeyer, M. V. Rodnina, and H. Stark, "Ribosome dynamics and tRNA movement by time-resolved electron cryomicroscopy," *Nature,* vol. 466, pp. 329-333, 2010.

[139] X. Agirrezabala, J. Lei, J. L. Brunelle, R. F. Ortiz-Meoz, R. Green, and J. Frank, "Visualization of the hybrid state of tRNA binding promoted by spontaneous ratcheting of the ribosome," *Molecular Cell,* vol. 32, pp. 190-197, 2008.

[140] P. Julian, A. L. Konevega, S. H. W. Scheres, M. Lazaro, D. Gil, W. Wintermeyer, M. V. Rodnina, and M. Valle, "Structure of ratcheted ribosomes with tRNAs in hybrid states," *PNAS,* vol. 105, pp. 16924-16927, 2008.

[141] J. B. Munro, R. B. Altman, N. O'Connor, and S. C. Blanchard, "Identification of two distinct hybrid state intermediates on the ribosome," *Molecular Cell,* vol. 25, pp. 505-517, 2007.

[142] S. H. Sternberg, J. Fei, N. Prywes, K. A. McGrath, and J. Ruben L. Gonzalez, "Translation factors direct intrinsic ribosome dynamics during translation termination and ribosome recycling," *Nature Structural and Molecular Biology,* vol. 16, pp. 861-869, 2009.

[143] S. A. McKinney, C. Joo, and T. Ha, "Analysis of single-molecule FRET trajectories using hidden Markov modeling," *Biophysical Journal,* vol. 91, pp. 1941-1951, 2006.

[144] L. P. d. l. Rama, L. Hu, M. Y. Efremov, E. A. Olson, P. F. Nealey, M. A. McLean, S. G. Sligar, and L. H. Allen, "Anomalous transitions of DODAB using fast scanning liquid calorimetry," *Thermochimica Acta,* vol. 522, pp. 72-76, 2011.

[145] F. E. Torres, P. Kuhnt, D. D. Bruyker, A. G. Bell, M. V. Wolkin, E. Peeters, J. R. Williamson, G. B. Anderson, G. P. Schmitz, M. I. Recht, S. Schweizer, L. G. Scott, J. H. Ho, S. A. Elrod, P. G. Schultz, R. A. Lerner, and R. H. Bruce, "Enthalpy arrays," *Proc. Natl. Acad. Sci. USA,* vol. 101, pp. 9517-9522, 2004.

[146] L. Wang, D. M. Sipe, Y. Xu, and Q. Lin, "A MEMS thermal biosensor for metabolic monitoring applications," *Journal of Microelectromechanical Systems,* vol. 17, pp. 318-327, 2008.

[147] L. Wang, B. Wang, and Q. Lin, "Demonstration of MEMS-based differential scanning calorimetry for determining thermodynamic properties of biomolecules," *Sensors and Actuators B: Chemical,* vol. 134, pp. 953-958, 2008.

[148] G. C. M. Meijer and A. W. Herwaarden, *Thermal Sensors*. London, United Kingdom: Institute of Physics Publishing, 1994.

[149] V. M. Lubecke, F. Pardo, and V. A. Lifton, "Polyimide spacers for flip-chip optical MEMS," *Journal of Microelectromechanical Systems,* vol. 16, pp. 959-968, 2007.

[150] B. Ziaie, A. Baldi, M. Lei, Y. Gu, and R. A. Siegel, "Hard and soft micromaching for BioMEMS: review of techniques and examples of applications in microfluidics and drug delivery," *Advanced Drug Delivery Reviews,* vol. 56, pp. 145-172, 2004.

[151] L. J. Matienzo and F. D. Egitto, "Poly(dimethylsiloxane)-polyimide blends in the formation of thick polyimide films," *Journal of Materials Science,* vol. 42, pp. 239-251, 2007.

[152] S. Wang, K. Tozaki, H. Hayashi, and H. Inaba, "Nano-watt stabilized DSC and its applications," *Journal of Thermal Analysis and Calorimetry,* vol. 79, pp. 605-613, 2005.

[153] K.-i. Tozaki, H. Inaba, H. Hayashi, C. Quan, N. Nemoto, and T. Kimura, "Phase transition of n-C32H66 measured by means of high resolution and super-sensitive DSC," *Thermochimica Acta,* vol. 397, pp. 155-161, 2003.

[154] D. M. Rowe, *CRC Handbook of Thermoelectrics*, 1st ed. Boca Raton FL: CRC-Press, 1995.

[155] H.-J. Hinz and F. P. Schwartz, "Measurement and analysis of results obtained on biological substances with d.s.c.," *Journal of Chemical Thermodynamics,* vol. 33, pp. 1511-1525, 2001.

[156] Y. X. Zhang, P. F. Xing, H. Y. Shi, J. Chen, P. W. Wang, and J. C. He, "On the heating rate dependence of crystallization temperatures of metallic glasses," *Journal of Applied Physics,* vol. 108, p. 033515 (8 pages), 2010.

[157] E. Zhuravlev and C. Schick, "Fast scanning power compensated differential scanning nano-calorimeter: 1. The device," *Thermochimica Acta,* vol. 505, pp. 1-13, 2010.

[158] M. V. Siljegovic, G. R. Strbac, F. Skuban, and S. R. Lukic-Petrovic, "Determination of thermal parameters of glasses from the system Bix(As2S3)100-x based on DSC curves," *Journal of Thermal Analysis and Calorimetry,* vol. 105, pp. 947-951, 2011.

[159] D. Souri, "Investigation of glass transition temperature in (60-x)V2O5-40TeO2-xNiO glasses at different heating rates," *Journal of Materials Science,* vol. 46, pp. 6998-7003, 2011.

[160] B. Wunderlich, "Quasi-isothermal temperature-modulated differential scanning calorimetry (TMDSC) for the separation of reversible and irreversible thermodynamic changes in glass transition and melting ranges of flexible macromolecules," *Pure and Applied Chemistry,* vol. 81, pp. 1931-1952, 2009.

[161] J.-L. Garden and J. Richard, "Entropy production in AC-calorimetry," *Thermochimica Acta,* vol. 461, pp. 57-66, 2007.

[162] R. Lortz, S. Abe, Y. Wang, F. Bouquet, U. Tutsch, and A. Junod, "Modulated-bath ac calorimetry using modified commercial Peltier elements," *Review of Scientific Instruments,* vol. 76, p. 103902, 2005.

[163] L. Carpentier, O. Bustin, and M. Descamps, "Temperature-modulated differential scanning calorimetry as a specific heat spectroscopy," *Journal of Physics D: Applied Physics,* vol. 35, pp. 402-408, 2002.

[164] A. W. v. Herwaarden, "Overview of calorimeter chips for various applications," *Thermochimica Acta,* vol. 432, pp. 192-201, 2005.

[165] F. E. Torres, P. Kuhnt, D. D. Bruyker, A. G. Bell, M. V. Wolkin, E. Peeters, J. R. Williamson, G. B. Anderson, G. P. Schmitz, M. I. Recht, S. Schweizer, L. G. Scott, J. H. Ho, S. A. Elrod, P. G. Schultz, R. A. Lerner, and R. H. Bruce, "Enthalpy arrays," *Proceedings of the National Academy of Sciences,* vol. 101, pp. 9517-9522, 2004.

[166] D. H. Jung, I. K. Moon, and Y. H. Jeong, "Peltier AC calorimeter," *Thermochimica Acta,* vol. 391, pp. 7-12, 2002.

[167] H. Huth, A. A. Minakov, and C. Schick, "Differential AC-chip calorimeter for glass transition measurements in ultrathin films," *Journal of Polymer Science: Part B: Polymer Physics,* vol. 44, pp. 2996-3005, 2006.

[168] Y. Inoue and Y. Nakazawa, "AC-calorimetry for detecting electronic phase transitions at low temperatures using micro-chip devices," *Thermochimica Acta,* vol. 492, pp. 85-88, 2009.

[169] D. Finotello, S. Qian, and G. S. Iannacchione, "AC calorimetric studies of phase transitions in porous substrates, superfluid helium and liquid crystals," *Thermochimica Acta,* vol. 304/305, pp. 303-316, 1997.

[170] B. Wang and Q. Lin, "A MEMS differential scanning calorimetric sensor for thermodynamic characterization of biomolecules," *Journal of Microelectromechanical Systems,* in press.

[171] P. K. Thiruvikraman, "Study of electronic phase transitions at high pressures," Doctoral, Mangalore University, 1999.

[172] F. I. Cruceanu, "AC-calorimetry and dielectric spectroscopy on anisotropic liquid crystal and aerosil dispersions," Doctoral, Worcester Polytechnic Institute, 2007.

[173] B. Ziaie, A. Baldi, M. Lei, Y. Gu, and R. A. Siegel, "Hard and soft micromachining for BioMEMS: review of techniques and examples of applications in microfluidics and drug delivery," *Advanced Drug Delivery Reviews,* vol. 56, pp. 145-172, 2004.

[174] T. Wiseman, S. Williston, J. F. Brandts, and L.-N. Lin, "Rapid measurements of binding constants and heats of binding using a new titration calorimeter," *Analytical Biochemistry,* vol. 179, pp. 131-137, 1989.

[175] R. E. Cavicchi, G. E. Poirier, N. H. Tea, M. Afridi, D. Berning, A. Hefner, I. Suehle, M. Gaitan, S. Semancik, and C. Montgomery, "Micro-differential scanning calorimeter for combustible gas sensing," *Sensors and Actuators B: Chemical,* vol. 97, pp. 22-30, 2004.

[176] E. B. Chancellor, J. P. Wikswo, F. Baudenbacher, M. Radparvar, and D. Osterman, "Heat conduction calorimeter for massively parallel high throughput measurements with picoliter sample volumes," *Applied Physics Letters,* vol. 85, pp. 2408-2410, 2004.

[177] E. Iervolino, A. W. v. Herwaarden, and P. M. Sarro, "Calorimeter chip calibration for thermal characterization of liquid samples," *Thermochimica Acta,* vol. 492, pp. 95-100, 2009.

[178] W. Lee, W. Fon, B. W. Axelrod, and M. L. Roukes, "High-sensitivity microfluidic calorimeters for biological and chemcial applications," *PNAS,* vol. 106, pp. 15225-15230, 2009.

[179] Y. Zhang and S. Tadigadapa, "Calorimetric biosensors with integrated microfluidic channels," *Biosnesors and Bioelectronics,* vol. 19, pp. 1733-1743, 2004.

[180] Y. Zhang and S. Tadigadapa, "Thermal characterization of liquids and polymer thin films using a microcalorimeter," *Applied Physics Letters,* vol. 86, p. 034101, 2005.

[181] V. Baier, R. Fodisch, A. Ihring, E. Kessler, J. Lerchner, G. Wolf, J. M. Kohler, M. Nietzsch, and M. Krugel, "Highly sensitive thermopile heat power sensor for micro-fluid calorimetry of biochemical processes," *Sensors and Actuators A: Physical,* vol. 123-124, pp. 354-359, 2005.

[182] A. J. Taberner, I. W. Hunter, R. S. Kirton, P. M. F. Nielsen, and D. S. Loiselle, "Characterization of a flow-through microcalorimeter for measuring the heat production of cardiac trabeculae," *Review of Scientific Instruments,* vol. 76, p. 104902, 2005.

[183] F. E. Torres, P. Kuhn, D. D. Bruyker, A. G. Bell, M. V. Wolkin, E. Peeters, J. R. Williamson, G. B. Anderson, G. P. Schmitz, M. I. Recht, S. Schweizer, L. G. Scott, J. H. Ho, S. A. Elrod, P. G. Schultz, R. A. Lerner, and R. H. Bruce, "Enthalpy arrays," *PNAS,* vol. 101, pp. 9517-9522, 2004.

[184] R. B. Spokane and S. J. Gill, "Titration microcalorimeter using nanomolar quantities of reactants," *Review of Scientific Instruments,* vol. 52, pp. 1728-1733, 1981.

[185] C. Hany, H. Lebrun, C. Pradere, J. Toutain, and J.-C. Batsale, "thermal analysis of chemical reaction with a continuous microfluidic calorimeter," *Chemical Engineering Journal,* vol. 160, pp. 814-822, 2010.

[186] B. Lubbers and F. Baudenbacher, "Isothermal titration calorimetry in nanoliter droplets with subsecond time constants," *Analytical Chemistry,* vol. 83, pp. 7955-7961, 2011.

[187] J. Xu, R. Reiserer, J. Tellinghuisen, J. P. Wikswo, and F. J. Baudenbacher, "A mcirofabricated nanocalorimeter: design, characterization, and chemical calibration," *Analytical Chemistry,* vol. 80, pp. 2728-2733, 2008.

[188] C. J. Campbell and B. A.Grzybowski, "Microfluidic mixers: from microfabricated to self-assembling devices," *Philisophical Transactions of the Royal Society A: Mathematical, Physical & Engineering Sciences,* vol. 362, pp. 1069-1086, 2004.

[189] R. Ferrigno, J. N. Lee, X. Jiang, and G. M. Whitesides, "Potentiometric titrations in a poly(dimethylsiloxane)-based microfluidic device," *Analytical Chemistry,* vol. 76, pp. 2273-2280, 2004.

[190] A. D. Stroock, S. K. W. Dertinger, A. Ajdari, I. Mezic, H. A. Stone, and G. M. Whitesides, "Chaotic mixer for microchannels," *Science,* vol. 295, pp. 647-651, 2002.

[191] MicroCal LLC, "ITC data analysis in Origin: Tutorial Guide," 2004.

[192] J. Tellinghuisen, "Designing isothermal titration calorimetry experiments for the study of 1:1 binding: problem with the "standard protocol"," *Analytical Biochemistry,* vol. 424, pp. 211-220, 2012.

[193] MicroCal LLC. Available: http://www.microcal.com/

[194] S. Vyawahare, A. D. Griffiths, and C. A. Merten, "Miniaturization and parallelization of biological and chemical assays in microfluidic devices," *Chemistry & Biology,* vol. 17, pp. 1052-1065, 2010.

[195] Y. Muraoka, S. Yamashita, T. Yamamoto, and Y. Nakazawa, "Microchip-calorimerty of organic charge transfer complex which shows superconductivity at low temperatures," *Thermochimica Acta,* vol. 532, pp. 88-91, 2012.

[196] A. Groisman, M. Enzelberger, and S. R. Quake, "Microfluidic memory and control devices," *Science,* vol. 300, pp. 955-958, 2003.

[197] T. Throsen, S. J. Maerkl, and S. R. Quake, "Microfluidic large-scale integration," *Science,* vol. 298, pp. 580-584, 2002.